

Syracuse University

SURFACE

Physics - Dissertations

College of Arts and Sciences

2011

Morphology and Mechanics of the Actin Cytoskeleton

David Aaron Quint
Syracuse University

Follow this and additional works at: https://surface.syr.edu/phy_etd



Part of the [Physics Commons](#)

Recommended Citation

Quint, David Aaron, "Morphology and Mechanics of the Actin Cytoskeleton" (2011). *Physics - Dissertations*. 113.

https://surface.syr.edu/phy_etd/113

This Dissertation is brought to you for free and open access by the College of Arts and Sciences at SURFACE. It has been accepted for inclusion in Physics - Dissertations by an authorized administrator of SURFACE. For more information, please contact surface@syr.edu.

Abstract

Contained in this thesis is the quest to model the growth, form and mechanics of part of the cellular cytoskeleton known as the lamellipodium. The cellular cytoskeleton is made of filamentous proteins, such as F-actin, and provides for structural support for the cell. Lamellipodia are extensions of the cellular cytoskeleton at the leading edge of a crawling cell generated so that the cell can extend, and thereby move in a particular direction. In the first two chapters, we focus on morphological characteristics of lamellipodia formation, which is, in part, shaped by branched filament nucleation via the branching protein Arp2/3. For example, we find that the orientation of filaments with respect to the leading edge of a crawling cell is optimized for filament growth. In addition, orientational and spatial degrees of freedom of the filaments are married to derive the overall shape of the filament density profile along the leading edge, another morphological characteristic. In the next two chapters, we explore the mechanics of model lamellipodia, where both freely-rotating and angle-constraining cross-linkers of actin filaments are present, in addition to the angle-constraining effect that the branching protein Arp2/3 has between mother and daughter filaments. We compare the mechanical properties of the compositely cross-linked filament networks to that of purely freely-rotating cross-linked filament networks, which has been studied by others previously. Using both theory and numerical simulations, we find that the addition of angle-constraining cross-linkers allows the lamellipodium to become rigid and transmit forces with a minimal amount of material—yet another optimization principle. Therefore, in our quest to

model lamellipodia formation, we have uncovered along the way several optimization principles, which may ultimately guide, in part, our understanding of how cells crawl to heal wounds or create organs.

MORPHOLOGY and MECHANICS of the ACTIN
CYTOSKELETON

By

David Quint

B.Sc., UC Santa Cruz, 2004

DISSERTATION

Submitted in partial fulfillment of the requirements for the
degree of Doctor of Philosophy in Physics
in the Graduate School of Syracuse University

August 2011

Copyright 2011 David Quint

All rights reserved

Contents

Chapter Summary	xvii
1 Lamellipodia Growth, Form and Physics	1
1.1 Crawling: Model cell - The keratocyte	3
1.1.1 F-actin	4
1.1.2 Growth at the leading edge - The Arp2/3 protein	7
1.1.3 Death at the leading edge - Capping proteins	8
1.1.4 Forces - Do “you” have what it takes?	9
1.1.5 The Dendritic Nucleation Model (DNM) - Fitting the pieces together	10
1.2 Theoretical implications of the DNM: Population dynamics	12
1.2.1 Fitness: Optimum orientation	14
1.3 Theoretical implications of the DNM: Spatial distribution of filaments	16
1.3.1 The Graded Radial Extension Model (GRE) - Relating ori- entational and spatial degrees of freedom	16
1.3.2 Filament density along the leading edge	17
1.4 Conclusion to chapter 1	20
2 Optimal Orientation of Branched Cytoskeletal Filaments	24
2.1 Mean field models	27
2.1.1 Collision-based model	27
2.1.2 Comparison with other models	33

2.1.3	Generalized birth/death rates	34
2.1.4	Fluctuations	37
2.2	Orientation influencing spatial organization	38
2.2.1	Filament density profile along the leading edge	38
2.2.2	Two-dimensional, discrete simulation	41
2.3	Conclusion to chapter 2	46
3	Rigidity and Random Networks	55
3.1	Constraint counting	56
3.2	Maxwell's floppy modes	59
3.3	Effective Medium Theory (EMT)	61
3.3.1	Disorder and fluctuations	63
3.4	Filament bending networks	68
3.4.1	The semiflexible chain	69
3.4.2	Force-extension of a semiflexible chain	70
3.4.3	EMT for semiflexible chains	72
3.4.4	Nonaffinity	77
3.5	Conclusion to chapter 3	78
4	Redundancy and Cooperativity-Mechanics of Cross-linked Filamentous Networks	81
4.1	Model and methods	84
4.1.1	EMT - Collinear and non-collinear bending	86
4.1.2	Numerical simulations	89
4.2	Results	90
4.2.1	Mechanical integrity as measured by the shear modulus	90
4.2.2	Non-affinity parameter	92
4.2.3	Scaling near the isostatic point	94

4.3	Conclusion to chapter 4	95
4.3.1	Crosslinker mechanics: Cooperativity	96
4.3.2	Crosslinker mechanics: Redundancy	97
4.3.3	Lamellipodia mechanics	99
A	Leading Edge Filament Density Profile	105
A.1	Lateral flow velocity	105
B	Rigidity and Effective Medium Theory (EMT)	107
B.1	Linearized Energy: Stretching and bending interactions	107
B.1.1	Stretching	107
B.1.2	Bending	108
B.2	Dynamical matrix calculation of a^*	109
B.3	Dynamical matrix calculation for b^*	112
C	Semiflexible Chain Force-extension	117
C.1	The weak bending limit	117
	Bibliography	119

List of Tables

1.1	Three classes of biopolymers and their properties found in the cellular cytoskeleton. In the case of intermediate filaments, there is a reasonable range of variation as classified by type I through VI. One example is vimentin, which is type III. The values were obtained from <i>in vitro</i> experiments.	4
-----	--	---

List of Figures

- 1.1 *Left* Image of a keratocyte in glide motion. **Red**: Leading edge of the lamellipodium, **Blue**: Posterior of the cell where the cytoskeletal network is disassembled. **Green/Black Arrow**: Indicates direction of motion and length ($\sim 2\mu m$) of the lamellipodium $1\mu m$. [J. Cell Biol., Vol. **178**, p. 1207 (2007)]; *Right* Schematic of cell crawling by extension of the lamellipodium via actin polymerization. [Int. J. Biol. Sci. Vol. **3**, p. 303 (2007)] 5
- 1.2 From left to right the nucleation and elongation of a F-actin filament by the polymerization of G-actin. In steady state the addition and subtraction of monomers at the ends of the filament occurs at a rate in which the total mass of the filament is unchanged, a process known as *treadmilling*. [Courtesy of Lodish H, et al., *Molecular Cell Biology*. 4th ed., W. H. Freeman, New York, (2000)] 6
- 1.3 *Left* Electron micrograph of a Sec. of the lamellipodia showing a dense network of integrated actin filaments; *Right* Smaller scale image of a dendritic branch of actin filaments formed by the incorporation of activated Arp2/3 protein. [J. Cell Biol., Vol. 145, p. 1009 (1999)] 8

-
- 1.4 Two models for the protrusion of the leading edge membrane by the polymerization of F-actin. *Left* The original Brownian ratchet model, Brownian fluctuations of the leading edge membrane open up space between the filament tip allowing for actin to polymerize. When the membrane returns it has advanced forward due to the increase in length of filaments by the addition of monomers; *Right* Modification to the Brownian ratchet model, bending elastic energy stored in the filament due to thermal fluctuations of the filament tip allow for the addition of G-actin monomers when the tip is bent away from the leading edge. Bending back toward the membrane the increase in filament length advances the membrane edge. [Nature Reviews: Molecular Cell Biology **7**, p. 404 (2006)] . . . 11
- 1.5 Schematic of the role of Arp2/3 in the dendrietic nucleation model as well as other important agents such as capping proteins. [Adapted from Annu. Rev. Biochem., Vol. **70**, p. 649] 12
- 1.6 Schematic of the Maly and Borisy population model for daughter filaments branching (B) from mother filaments (M) at an angle ψ . Filaments have a higher probability to be capped the farther they are oriented from the leading edge membrane (θ). (solid horizontal line)). 14
- 1.7 Comparison of the GRE model with that of the PE model. [Nature **362**, pg. 167 (1993)] 18
- 1.8 Schematic of filament lateral flow due to expansion of the leading edge consistent with the Graded Radial Extention Model. [Eur. Biophys. J., Vol. **32**, p. 563 (2003)]. 19

1.9	Experimentally measured filament distribution of F-actin along the leading edge of a live crawling cell using immunofluorescence labeling. The peak of intensity occurs at the midpoint of the lamellipodium. [PLoS Biol., Vol. 5 p. 2035 (2007)]	20
2.1	Schematic of the orientation of a branched filament (B) in relation to its mother filament (M) and the horizontal line denotes the leading edge.	29
2.2	Depiction of the optimal orientation (red) and the two suboptimal ones (blue, green).	32
2.3	Plot of $q(\theta)$ for $\psi = 70^\circ$. For $\sigma = 4^\circ$, $\frac{c'}{b'} = 0.269$, for $\sigma = 8^\circ$, $\frac{c'}{b'} = 0.254$, and for $\sigma = 12^\circ$, $\frac{c'}{b'} = 0.213$	50
2.4	Left: Dimensionless filament densities along the leading edge, where $\rho_c = \tilde{\rho}_c^+ + \tilde{\rho}_c^-$, for example. Right: Total dimensionless filament density ($\rho_c + \rho_l + \rho_r$) along leading edge.	50
2.5	Discrete simulation output with $\psi = 70^\circ$, $\theta = 35^\circ$, and $\sigma = 10^\circ$. The length of the horizontal bar is 1 micron.	51
2.6	Left: Growth rate for different branch angles. Right: Growth rate for for $c = 0.67 \text{ s}^{-1}$ (and so more growth than for $c = 0.83 \text{ s}^{-1}$).	51
2.7	Growth rate for 70 degree branching angle with noise.	52
2.8	Bethe lattice with coordination number three. The circles indicate a repeating pattern.	52
2.9	Left: The ratio of overlaps to branch points as a function of θ with $\sigma = 10^\circ$ for two fixed branch angle curves. Right: The ratio of overlaps to branch points as a function of θ for a smaller capping rate (more overlaps). Here, $\sigma = 0^\circ$	53

-
- 2.10 Left: Spatial distribution of filament tips in the x -direction (horizontal) for $\psi = 60^\circ, 70^\circ, 80^\circ$ and the random branch model. Right: Spatial distribution of filament tips in the y -direction (vertical) for $\psi = 60^\circ, 70^\circ, 80^\circ$ and the random branch model. For both plots, $\sigma = 10^\circ$ 54
- 3.1 (Left) Schematic of the set of unconnected points on a 2 dimensional square grid; (Right) Schematic of one configuration of bonds. The **red** bond is redundant, while the **blue** dashed line is where the red one should be placed if the frame is to be rigid. 57
- 3.2 (Left) Unit cell of a triangular lattice. Lattice node(site) i has at most 6 nearest neighbors j . (Right) The lattice site i is in static equilibrium when there is at least 4 neighbor connections. 60
- 3.3 A section of a bond diluted triangular lattice with $p > p_r$ 63
- 3.4 To construct a triangular lattice we start with a square lattice and add a diagonal constraint. Shown here is 1/3 of the triangular unit cell. 65
- 3.5 The effective spring network after combining all series and parallel sub-networks. 66
- 3.6 Plot of the shear modulus G varying the bond occupation probability p . The transition to a rigid network happens for $p \simeq 2/3$ for this simulation with a system size of $N = 128 \times 128$ lattice sites. Inset shows the nonaffinity of the deformations within the lattice. As p approaches the isostatic point (p_{iso}) the nonaffinity parameter (Γ) diverges which signals the transition from a floppy network to a rigid one (See section 3.4.4 and chapter 4 for details). 68

- 3.7 Schematic of the position vector $\vec{r}(s)$ along a section of a semiflexible chain as a function of the chain's contour coordinate s . Also shown the unit tangent vector $\vec{t}(s)$ 70
- 3.8 Bending interactions on the lattice involve three sites ijh . Bending is defined as the angle between the bonds \overline{ij} and \overline{ih} . In the undeformed (red) lattice the equilibrium configuration is when bond \overline{ij} and \overline{ih} are parallel. The deformed (blue) lattice is depicting a \mathbf{q} dependent strain \mathbf{u} . [Phys. Rev. Lett. Vol. 99, 038101 (2007)] 76
- 4.1 Deformed configuration a compositely cross-linked semiflexible network with 2.7 percent strain, with bond occupation probability $p = 0.64$, and angle-constraining cross-linker occupation probability $p_{nc} = 0.15$ The purple lines denote semiflexible filaments, the red arcs denote angle-constraining cross-links, the black circles represent nodes where all crossing filaments are free to rotate, while the grey circles denote nodes where some of the crossing filaments are free to rotate. The filament bending stiffness relative to stretching stiffness $\kappa/\alpha = 10^{-6}$ and the stiffness of angular cross-links relative to stretching stiffness $\kappa_{nc}/\alpha = 10^{-6}$ 85
- 4.2 The shear modulus as a function of p for semiflexible networks with freely-rotating crosslinks ((a) and (d)), flexible networks with freely-rotating and angle-constraining crosslinks ((b) and (e)), and semiflexible networks with both crosslinkers ((c) and (f)). The top panels show results from the effective medium theory and bottom panels show results from the simulations. 91

- 4.3 The presence of angular constraints allows these networks to have a finite rigidity even for small concentration of filaments. Figure (a) shows how the rigidity percolation threshold can be continuously lowered by increasing the concentration of angular springs for flexible (solid, blue) and stiff (dashed, red) networks. The lines correspond to the effective medium theory and the symbols to the numerical simulation. Figures (b) and (c) show the shear modulus (in logarithmic scale described by the colorbar) as a function of p and p_{nc} for flexible networks (b) and semiflexible networks (c). The parameter values studied are (b) $\kappa_{nc}/\alpha = 10^{-4}$ and (c) $\kappa/\alpha = 10^{-4}$, $\kappa_{nc}/\alpha = 10^{-2}$. The black dashed lines in (b) and (c) correspond to the effective medium theory prediction of the rigidity percolation threshold. For the flexible networks $L = 32$ while for semiflexible networks $L = 64$ 92
- 4.4 The non-affinity parameter Γ as a function of p for semiflexible networks with both types of crosslinkers. In (a) we show the effect of changing the concentration p_{nc} of the angle-constraining crosslinkers for $\kappa/\alpha = 10^{-4}$, $\kappa_{nc}/\alpha = 10^{-2}$, while in (b) we show the effect of changing their stiffness κ_{nc} 94
- 4.5 Close to isostaticity, the shear modulus G scales with $\Delta p = p - p_{rp,I}$ and κ (κ_{nc}) as $G|\Delta p|^{-f} = \kappa|\Delta p|^{-\phi}$. The effective medium theory predicts mean field exponents $f = 1$ and $\phi = 2$ for both semiflexible networks with freely-rotating crosslinkers (a) and compositely crosslinked flexible networks (b), while simulations predict $f = 1.1(1)$ and $\phi = 2.9(1)$ for semiflexible networks with freely-rotating crosslinkers (c) and $f = 1.1(1)$ and $\phi = 2.8(1)$ for compositely crosslinked flexible networks (d). 95

-
- A.1 Schematic of filament lateral flow due to expansion of the leading edge. Note that Δf is the full derivative of $f(x, t)$. The dashed curve is the leading edge at a time of $t + \Delta t$ and the position of the filament between the two solid dots has moved from x to $x + \Delta x$. . 106
- B.1 Schematic figure of the filament network. The solid red lines represent the undeformed filament network, while the dashed blue lines show the deformation field having wavevector \mathbf{q} and displacement amplitude \mathbf{u} (shown in the upper left corner of the figure). The black arrows show the displacement field at each lattice point. This perfect lattice is disordered by making randomly placed cuts in the infinitely long filaments. These are not shown. [Courtesy of M. Das, unpublished] 113

Chapter Summary

Chapter 1

In our quest to model lamellipodia formation, Chapter One describes what is previously known about the growth, form, and function of the lamellipodium of a crawling cell. All three facets follow from the regulation of the polymerization of the biopolymer F-actin with the dominant mechanism for filament nucleation being branching via the protein Arp2/3. Other proteins, such as a capping protein preventing the polymerization of actin filaments, are also described. In addition, crosslinking proteins and severing proteins each have a role to play in lamellipodia formation. Given these various players, F-actin, Arp2/3, and capping protein, etc., what is known as the dendritic nucleation model has emerged as the dominant qualitative picture for lamellipodia formation. Implications of the dendritic nucleation model, such as an optimal orientation for filament growth and coupling the optimal orientation of filaments with spatial degrees of freedom to solve for an optimum filament density profile along the leading edge of a crawling cell, are discussed.

Chapter 2

Given the context of Chapter One, Chapter Two explores a new kinetic model where only branching and capping are included as the main aspects of filament regulation in lamellipodia. The branching can be viewed as the birth of new filaments, while the capping can be viewed as the death of filaments such that a population dynamics analysis is in order. Optimizing for the birth of new filaments, an optimal orientation of filaments with respect to the leading edge is related to the inherent branch angle that Arp2/3 generates between mother and daughter filaments. Since other kinetic models also produce the same optimum relationship, we address the generic feature of population models where orientation is an explicit property of the population's survival. Furthermore, we address the spatial dependence of the density filaments along the leading edge where the optimal orientation and a new secondary optimal orientation of filaments is included to arrive at a profile that more accurately models experiments than previous work. Finally, we address a recent controversy over the role of the Arp2/3 branching mechanism and the resulting network architecture.

Chapter 3

Chapter Three reviews the machinery needed to explore the mechanics of disordered, filamentous networks, where the disorder is typically modeled as random dilution of some lattice system. Starting from the general concept of constraint counting, a connection is made between the mechanical response of a disordered network of linear springs to the number of remaining unconstrained degrees of freedom in the system. This connection is the beginning of the field now known as rigidity percolation from which several theoretical approaches have emerged, one being effective medium theory (EMT). EMT is reviewed here for linear springs and

allows one to calculate, for example, the shear modulus as a function of the dilution of the lattice. Now, crosslinked networks of semiflexible filaments, such as the actin cytoskeleton, are naturally disordered as well, but involve bending energies in addition to stretching (linear spring) energies. The bending energy, even for an individual semiflexible filament, results in a highly nonlinear force-extension curve at large enough extension, for example. It turns out that an EMT has been previously developed for crosslinked semiflexible filament networks, where the crosslinks are freely-rotating (just as in the linear spring case). We review this semiflexible EMT here.

Chapter 4

Chapter Four continues the study of disordered, filamentous networks using effective medium theory. However, given the importance of Arp2/3 in forming lamellipodia from a filament generation standpoint, we ask about its mechanical role as an angle-constraining crosslinker between the mother and daughter filament as well as the mechanical role of another angle-constraining crosslinker, filamin A, which is prevalent in lamellipodia. Therefore, we study the effect of two types of crosslinkers on the mechanics of filamentous networks with the first type being the usual freely-rotating crosslinkers, such as α -actinin, and the second being angle-constraining crosslinkers. We find that the two types of crosslinkers can affect cooperatively as well as redundantly the mechanics of these networks. As an example of cooperativity, we find that the addition of angle-constraining crosslinkers lowers the onset of rigidity to the point where the network first forms spanning structures (geometric percolation). With just freely-rotating crosslinkers, the onset of rigidity occurs further beyond the point at which the network first forms spanning structures. As an example of redundancy, both the purely free-

rotating crosslinked networks and the compositely crosslinked networks exhibit a qualitatively similar mechanical property where deformation in the network can pass from a purely non-affine dominated regime to a purely affine regime upon increasing the average filament length in the system.

Chapter 1

Lamellipodia Growth, Form and Physics

Motion of a living system can be accomplished in many different ways. In large, multicellular organisms motion derives from the collection of many cells working in concert. For example in vertebrates, motion comes about by a series of nerves impulses from the central nervous system to muscles which contract and pull the skeleton in a coordinated fashion to produce motion. There exists a balance of internal and external forces and torques that are changing in time and must be adapted to in order for the process of locomotion to continue. Given the length scale on which most vertebrates live, motion is mostly effected by gravity and, hence motion, is mostly concerned with achieving mechanical equilibrium with gravity. However, when one examines smaller organisms, such as individual cells, where the length scale in which they live is about 10^{-6} times smaller than vertebrates, gravity plays a minor role due to their small mass. On these small length scales, other forces are far more dominant. One can ponder how locomotion is sustained in these smaller living systems. What forces need to be

overcome and what mechanisms are employed to deal with them? D'arcy Thompson, a pioneering mathematical biologist and author of the scientific classic, *On Growth and Form*, pointed out [1],

“The predominant factors are no longer those of our scale; we have come to the edge of the world of which we have no experience and where all of our preconceptions must be recast.”

There two main methods of cellular locomotion in single cell, or colonies of cells. The first is by use of a flagellum or many flagella. Long biopolymers, which are bundled together by crosslinking proteins, form a flagella that can undulate when active protein motors pull on them. In sperm, protein motors pull on the long biopolymer cables relative to one another causing these undulations. In *E. Coli*, many flagella are connected to a protein rotary motor which rotates one end of flagella into a cork screwing type motion. In either case, flagella are used to allow cells or colonies of cells to swim in fluid environments. This implies that environmental forces are hydrodynamic and typical cell speeds are low enough such that the swimming occurs at low Reynolds number [2].

The second form of locomotion is accomplished by crawling along a substrate. These systems share a common feature with their swimming counterparts in that they also employ biopolymers as a mechanism for locomotion, but unlike undulating a static assemblage of cables, they continually grow them in the direction of motion. Crawling usually occurs along a substrate in which these cells are attach. This implies that the most dominant forces are due to the interaction between the cell and substrate elasticity. It is one aspect of this type of locomotion that we will focus on in this thesis. Of, course, in crawling and swimming cells, the mechanisms for locomotion that are available were brought on by aeons of evolution and have adapted to accommodate the surrounding environment resulting in

a deliberate and coordinated series of internal biochemical/biomechanical queues that initiate and sustain motion.

1.1 Crawling: Model cell - The keratocyte

Cells crawl to heal wounds, to create organs, and to spread cancer, the latter of which can have deleterious effects. The main cell type that has emerged as the front runner in the theoretical and experimental study of cell crawling is the fish keratocyte cell, a cell that exists on the scales of fish and crawls to heal wounds. Fish keratocyte cells are among the fastest movers, crawling up to speeds of $0.2 \mu\text{m}/\text{sec}$ (compared to $1 \text{m}/\text{sec}$ for vertebrates). For an image of a keratocyte cell, see Fig. 1.1).

Cells crawl by the constant growth and active manipulation of their intracellular skeleton, known as the cytoskeleton. The cytoskeleton is made up of filamentous proteins, such as intermediate filaments, microtubules, and F-actin, that polymerize, depolymerize, crosslink, get severed, etc. with the assistance of other globular proteins. These filaments also provide structural support for the cell. When a cell begins to crawl in a particular direction, it extends its cytoskeleton in that direction (see the red line in Fig. 1.1). This extension, or growth, is driven by filament nucleation and polymerization, in particular, and is typically thin, approximately 100-200 nanometers in width. The location of this new growth at the leading edge occurs in what is known as the *lamellipodium* [3]. While actin cytoskeletal growth is taking place in the lamellipodium pushing the cell forward [4, 5, 6], contraction of the existing cytoskeleton at the rear of the cell is occurring so that the rear of the cell can catch up with its front resulting in motion as opposed to just extension. There is also dismantling of cytoskeleton in

Type	monomer	k_{on} ($(\mu M)^{-1} s^{-1}$)	k_{off} (s^{-1})	persistence len. (l_p)
F-actin	G-actin	9.2	2.9×10^6	$17 \mu m$
Microtubels	Tubulin	2 – 10	0.1	1 – 5 mm
Intermediates	Ex.vimentin	Variable	Variable	$1 \mu m$

Table 1.1: Three classes of biopolymers and their properties found in the cellular cytoskeleton. In the case of intermediate filaments, there is a reasonable range of variation as classified by type I through VI. One example is vimentin, which is type III. The values were obtained from *in vitro* experiments.

various places since the cell is a closed system in terms of its cytoskeleton. Therefore, it must recycle material to continue the process of cytoskeletal growth at the front given the finite amount of cytoskeletal material. In addition to extension at the front and retraction at the rear, there is also interaction of the cell with the substrate via adhesion protein complexes that are assembled in the front and disassembled in the rear (see *right* Fig. 1.1 [7]). All of these different processes in cell crawling are coordinated such that as the keratocyte is crawling along, its motion can be regarded as steady-state motion[8, 9].

While the process of cell crawling involves cytoskeletal growth, retraction, and adhesion, here we focus on the cytoskeletal growth aspect, or lamellipodia formation. To address lamellipodia formation, we will now describe several important players involved: F-actin, Arp2/3, and capping proteins.

1.1.1 F-actin

The cytoskeleton is used for a multitude of duties that the cell must carry out, for example maintaining cell shape, locomotion, growth and division(mitosis/miosis). The cellular cytoskeleton contains several different biopolymers [10], which each have distinct polymerization rates and mechanical properties (see table 1.1) [11,

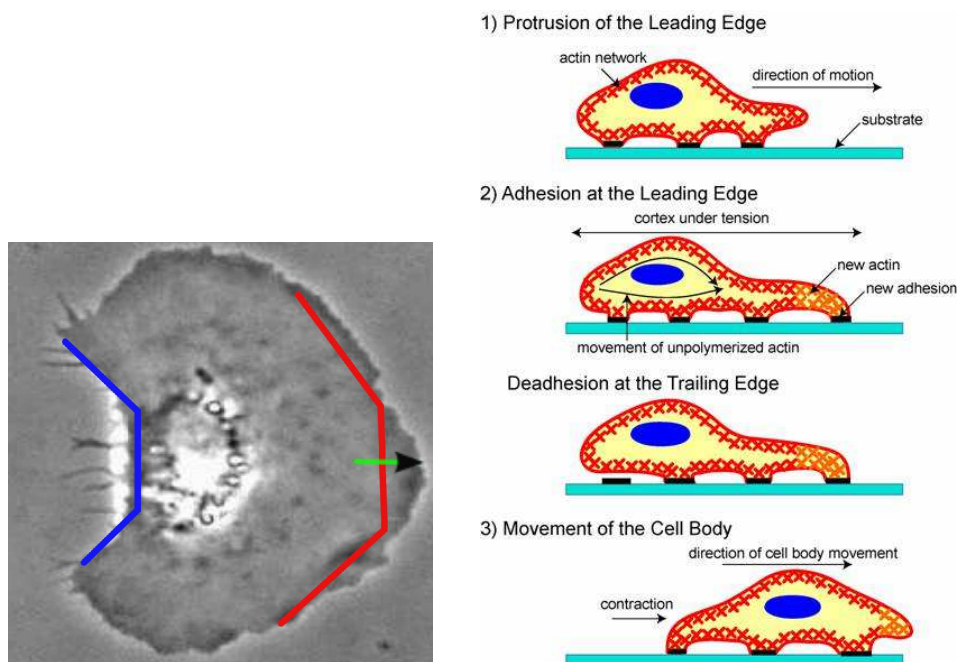


Figure 1.1: *Left* Image of a keratocyte in glide motion. **Red**: Leading edge of the lamellipodium, **Blue**: Posterior of the cell where the cytoskeletal network is disassembled. **Green/Black Arrow**: Indicates direction of motion and length ($\sim 2\mu m$) of the lamellipodium $1\mu m$. [J. Cell Bio., Vol. **178**, p. 1207 (2007)]; *Right* Schematic of cell crawling by extension of the lamellipodium via actin polymerization. [Int. J. Biol. Sci. Vol. **3**, p. 303 (2007)]

12, 13, 14], to carry out its duties. The most dominant biopolymer is the actin biopolymer [10]. The actin filament, or simply F-actin, is a polar homopolymer filament with a *plus* (+) or *barbed* end where G-actin monomers are added and a *minus* (−) or *pointed* end (see Fig. 1.2), where depolymerization occurs.¹ Because the difference in the off/on rates, a phenomenon known as treadmilling [6, 3, 15] can occur where there is net motion of the center of mass of the filament.

The diameter of a single actin monomer, G-actin, is roughly $5.4nm$ and has a molecular weight of $42kDa$. G-actin monomers assemble into actin filaments by converting ATP into ADP with a k_{on} rate of $12\mu M^{-1}s^{-1}$ and a k_{off} of $8.0s^{-1}$

¹Depolymerization can occur at the plus end as well but the rate is about 8 times slower.

from the minus end [16]. As monomers are added to the plus end there is a natural double helix structure which induces a twist of monomers with a repetition length of 37 nm [17]. This twist in turn sets filament elongation at roughly half the monomer diameter $\delta \sim 2.7\text{ nm}$ per monomer.

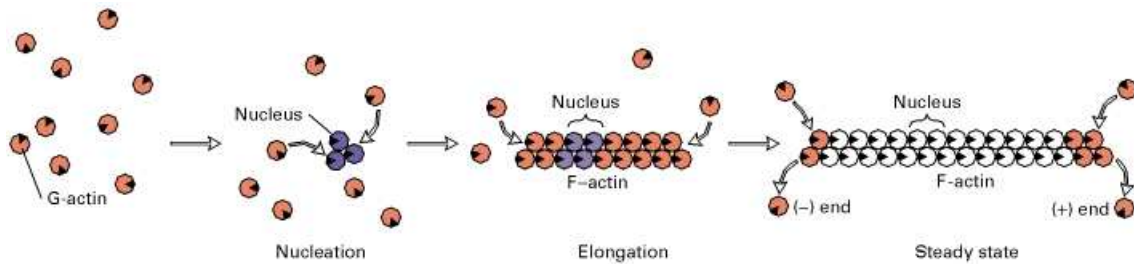


Figure 1.2: From left to right the nucleation and elongation of a F-actin filament by the polymerization of G-actin. In steady state the addition and subtraction of monomers at the ends of the filament occurs at a rate in which the total mass of the filament is unchanged, a process known as *treadmilling*. [Courtesy of Lodish H, et al., *Molecular Cell Biology*. 4th ed., W. H. Freeman, New York, (2000)]

F-actin has intrinsic mechanical properties due to the strength of the bonds between ADP bound monomers. Briefly, polymers can be characterized by their *persistence length*, which is a temperature dependent property. For filaments much shorter than the persistence length, the filament acts as an elastic beam, i.e. bending energy. For filaments much longer than the persistence length, the filament acts as a Gaussian chain. In other words, the filament can be modeled as a random walk, i.e. no bending energy. Technically, the persistence length, l_p , is the length scale beyond which the tangent-tangent correlation of a polymer of length l vanishes (see chapter three section 3.4 for more details) [18]. Unlike many organic polymers with a persistence length of a couple monomers, actin is fairly stiff with a persistence length of about $17\ \mu\text{m}$. This stiffness in single filaments is extremely useful for cells to maintain cell shape, where average lengths of filaments in the cytoskeleton are much less than the persistence length. The mechanical properties of actin will be explored more in later chapters.

1.1.2 Growth at the leading edge - The Arp2/3 protein

In the previous Sec. it was pointed out that polymerization is the main propulsive force behind cell motion. Extending preexisting filaments can only occur by the addition monomeric G-actin. The generation of new filaments can also come from the spontaneous dimerization of G-actin. However, the polymerization of the new filaments will be random with respect to the direction of motion, since nucleation and growth have no preferred direction with respect to the leading edge. However, the cell must direct this new growth in the direction of leading edge or the motion will certainly halt since filament growth will not keep up the membrane. How can the cell direct the polymerization of F-actin filaments such that new growth will be focused in the direction of the leading edge of the cell?

The answer to this question is actin-binding protein known as the Arp2/3 protein. Arp2/3 has a molecular weight of 224 *kDa* and a physical size of 10 – 14 *nm* [6]. Arp2/3 mimics the plus end of an actin dimer [19] which has the ability to proliferate and direct new growth due to a preferred orientation induced by Arp2/3 binding to existing filaments. Arp2/3 nucleates new filaments only after it is activated by the WASP (Wiskott-Aldrich Syndrome Protein) family of proteins[20, 21, 19]. The WASP protein is a membrane protein that concentrates near the leading edge. Once the Arp2/3 is activated, it binds with nearby G-actin monomers creating a nucleation core called a mini-filament (dimers or trimers). The Arp2/3 complex then integrates into the cytoskeletal network by binding to pre-existing filaments to form a *daughter filament* branch. Once the Arp2/3 has become bound to an existing filament the minus end of the filament is now capped by the Arp2/3 complex and can not depolymerize from it's minus end, though it can eventually debranch. The Arp2/3 bound mini-filament forms a branch which makes a regular angle with respect to plus end of the mother filament of $\sim 67^\circ \pm 12^\circ$

[6, 22]. As the branching progresses, provided G-actin is plentiful at the leading edge, filament growth towards the leading edge of the crawling cell is promoted. In addition, the network will take on a *dendritic*-like structure [6, 15, 16, 22](See Fig. 1.3). It is believed that Arp2/3 is primarily activated and incorporated into the network within the first $\sim 100\text{ nm}$ of the leading edge membrane. Possible mechanisms for its production/activation/release into the cytoskeletal network can be mechanical or chemical signaling. Studies of *in vivo* networks have shown that the average number of branch points per filament length is about 100 nm^{-1} .

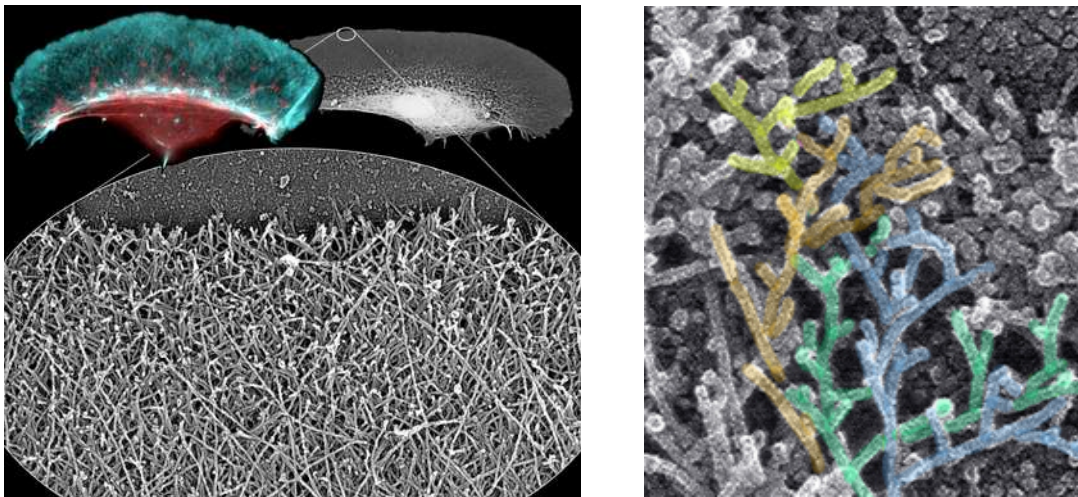


Figure 1.3: *Left* Electron micrograph of a Sec. of the lamellipodia showing a dense network of integrated actin filaments; *Right* Smaller scale image of a dendritic branch of actin filaments formed by the incorporation of activated Arp2/3 protein. [J. Cell Biol., Vol. 145, p. 1009 (1999)]

1.1.3 Death at the leading edge - Capping proteins

While filament growth ensures that the lamellipodia continues to push the membrane in the direction of motion, what mechanism ensures that the G-actin concentration at the leading edge is maintained at roughly $\sim 100\ \mu\text{M}$? Since the cell is a closed system, the available amount of G-actin is finite. Therefore regulation of its consumption is a concern for sustaining locomotion. To accomplish this

regulation, capping proteins are employed to halt the further polymerization of existing filaments.

Once a filament is capped it will no longer keep up with the leading edge during locomotion since G-actin can no longer bind to the filament's plus (+) end. Moreover, since activated Arp2/3 is located near the leading edge, the chance of a branching event occurring once a filament is capped decreases significantly [22]. Capped filaments eventually do not contribute to cell pushing (see next Sec.) and become disassociated from the network by *severing* proteins, which disassemble F-actin. G-actin monomers are then recycled and eventually flow back up to the leading edge where they are reintegrated into growing/nucleating filaments. Death, as well as birth, is required for the sustaining motility in a system with finite resources.

Studies suggest that capping protein is key in developing and regulating the dendritic actin network found in the lamellipodium [23]. However, capping does not prevent the side-binding of an activated Arp2/3 nucleator to a capped filament. Therefore, the growth of new, shorter, branched filaments is promoted, as opposed to extending existing filaments, in addition to aiding in the recycling of material.

1.1.4 Forces - Do “you” have what it takes?

Now that filament nucleation has been addressed, let us estimate how many filaments are required to extend the leading edge of the cell. As filaments grow behind the membrane at the leading edge, eventually they will come in contact with the membrane and exert a force on it. What sort of forces are required to propel the membrane forward? The membrane can have a thickness ranging from $7.5 - 10 \text{ nm}$ [24]. Force estimates for moving a Sec. of membrane of size $1 \mu\text{m}$ is

10 – 20 pN [25]. Does the Brownian ratcheting of growing filaments provide for enough force?

As for a back-of-the-envelope calculation, assuming that the thermally fluctuating filaments are approximately hookian springs with an effective spring constant of $\kappa \sim 0.16 pN/nm$ [4], then the force exerted per filament when a new monomer is added to the filament tip on the membrane is $\sim 0.4 pN$ (assuming that filament tips are perpendicular to the membrane edge and the tip increases by $2.7 nm$) [5]. When the force exerted by the membrane per filament is equal to the maximum ratchet force that a single filament can produce, then the number of filaments in which motion is stalled is $20/0.4 \sim 50$, or $50 \mu m^{-1}$. Therefore, the number of filaments per nanometer can not go below this value. Experimental evidence using florescently label G-actin suggests that the density of F-actin near the leading edge is peaked near the middle and estimates of number of actin filaments exceed $10^2 \mu m^{-1}$ [9, 26]. Therefore, the crawling cell is not limited by the membrane as it should not be. I should also point out that the estimated force needed to stall polymerization per filament (see Fig. 1.4 [27]) is about $2 - 7 pN$ [4, 5].

Nano-Newtons of force are needed stall single migrating cells [28]. This scale is consistent with the stalling force of individual filaments since for a $10 \mu m$ span, the number of filaments is in the thousands.

1.1.5 The Dendritic Nucleation Model (DNM) - Fitting the pieces together

To further investigate how filament nucleation and polymerization shapes the morphology of lamellipodia, one has to consider the kinetics of these processes. Fundamentally, the internal ongoings of the cytoskeleton are biochemical. Reaction pathways of various proteins and ATP hydrolysis help regulate the motion of keratocytes and other crawling cells. The connection between the biochemistry of

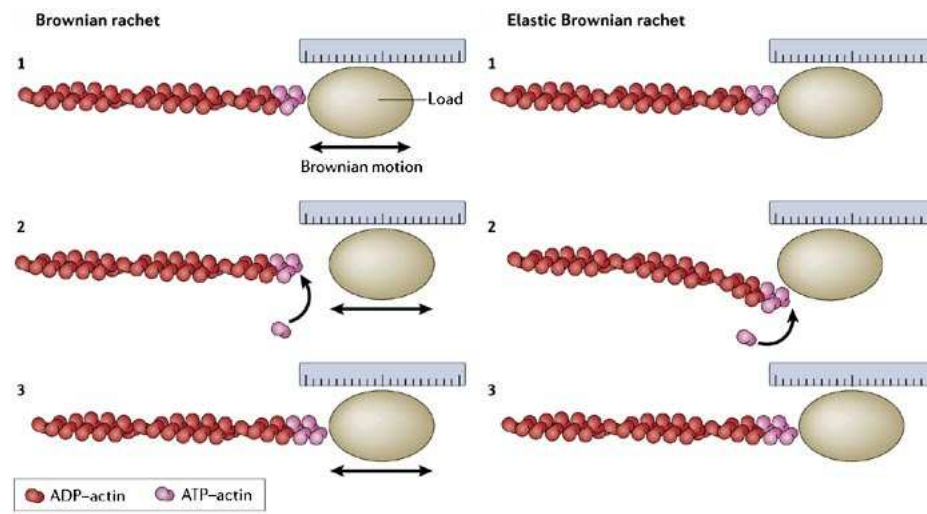


Figure 1.4: Two models for the protrusion of the leading edge membrane by the polymerization of F-actin. *Left* The original Brownian ratchet model, Brownian fluctuations of the leading edge membrane open up space between the filament tip allowing for actin to polymerize. When the membrane returns it has advanced forward due to the increase in length of filaments by the addition of monomers; *Right* Modification to the Brownian ratchet model, bending elastic energy stored in the filament due to thermal fluctuations of the filament tip allow for the addition of G-actin monomers when the tip is bent away from the leading edge. Bending back toward the membrane the increase in filament length advances the membrane edge. [Nature Reviews: Molecular Cell Biology **7**, p. 404 (2006)]

the cell, the structure of the cellular cytoskeleton, and the forces that it exerts/senses on/from the external world is still lacking. However, a simple, qualitative picture sometimes comes to the rescue such that one is able to obtain some quantitative understanding of the underlying properties which determine what one observes *in vitro* and even *in vivo*. One such contribution is the *Dendritic Nucleation Model* (DNM) [6]. Given Arp2/3 and its ability to nucleate new filamentous actin at a higher rate than dimerization, the central tenet of the DNM is that the predominant pathway of new filament generation is via Arp2/3 nucleating new branched filaments off of preexisting ones.

In addition, the branching occurs at a regular angle of $70^\circ \pm 7^\circ$ with respect to the plus end of the mother filament [6]. Therefore, continual integration of fila-

mentous actin with Arp2/3 will form a dendritic array of actin filaments which will push against and support the leading edge membrane during locomotion. Moreover, growing plus ends will meet the membrane at a regular angle close to 45° due to the inherent branch angle given previously, which can provide for mechanical stability [6]. (See fig 1.5).

Now, given the qualitative framework of the dendritic nucleation model, what sort of predictions or retro-dictions can one make about cytoskeletal dynamics and the resulting structure/morphology of the cytoskeleton itself?

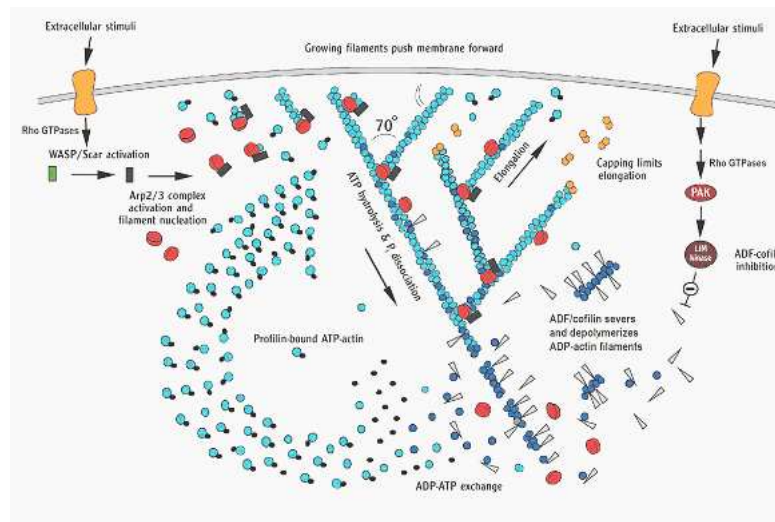


Figure 1.5: Schematic of the role of Arp2/3 in the dendritic nucleation model as well as other important agents such as capping proteins. [Adapted from Annu. Rev. Biochem., Vol. **70**, p. 649]

1.2 Theoretical implications of the DNM: Population dynamics

In light of the Dendritic Nucleation Model (DNM) one can investigate the orientation of filaments with respect to the membrane at the leading edge of a crawling

cell. Given that branching occurs at roughly a 70° between mother and daughter filaments, is it possible to see this preferred orientation of filament tips in a population dynamics sense? This orientation with respect to the normal of the leading edge was measured in chemically frozen cells and indeed there is a preferred angle of tip orientation of roughly half of the branch angle [6, 15].

Since branching is the central tenet of the DNM, one can quantify branching as lamellipodia having two populations of filaments: 1) branches or daughters and 2) mother filaments. Mother filaments can give birth to daughters at a certain rate(probability) when an activated Arp2/3 binds to the side or tip of a mother filament. Mother filaments can become capped at the plus end which will prohibit further polymerization, and the filament will die since it will not be able to keep up with the leading edge. Moreover, branches or daughters attached to a capped mother now become the new mother which, in turn, incorporate a new branch allowing the process. It is possible to have branches that form on capped mothers, but if one assumes tip branching then a capped tip will not incorporate a new branch [29]. If the branch is a side branch then one would expect that it would not be able to keep up with the membrane edge and hence these populations would die off quickly.

A population model along these lines was introduced by Maly and Borisy [22]. In this model, there are two populations which are coupled via their branching (*birth*) rates, b , and coupled to their respective orientation angles $(\theta, \theta - \psi)$ defined with respect to the membrane edge through their capping (*death*) rate, c (see Fig. 1.6). The population of mother filaments is denoted by n_1 and is oriented at an angle θ with respect to the normal of the leading edge. For a branch angle of ψ , the second population, denoted by n_2 , represents the progeny of population n_1 and is oriented at $\theta - \psi$. The capping rates depend on the orientation in a

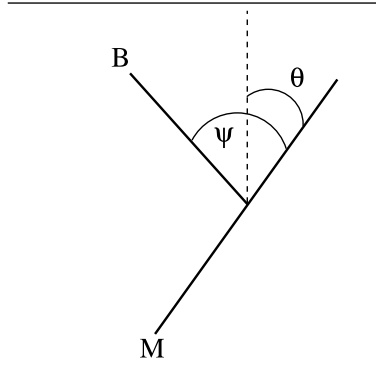


Figure 1.6: Schematic of the Maly and Borisy population model for daughter filaments branching (B) from mother filaments (M) at an angle ψ . Filaments have a higher probability to be capped the farther they are oriented from the leading edge membrane (θ). (solid horizontal line)).

way which enhances the probability of filament death for angles which are large (defined by the normal of the leading edge) since filaments angled away from the leading edge are more likely to get capped because the membrane will not “be in the way”. The Eq.s for this model are

$$\begin{aligned} \frac{dn_1}{dt} &= \frac{b}{2}n_2 - \frac{cp_0}{\cos(\theta)}n_1 \\ \frac{dn_2}{dt} &= \frac{b}{2}n_1 - \frac{cp_0}{\cos(\theta - \psi)}n_2. \end{aligned} \quad (1.1)$$

In this model, capping can significantly reduce either population because as θ or $\theta - \psi$ approaches $\pi/2$ then $\cos^{-1}() \gg 1$. The parameter p_0 depends on the cell velocity and the polymerization rate.

1.2.1 Fitness: Optimum orientation

One important feature of this system is its optimum behavior. Its optimal behavior will help determine its evolutionary fitness. Fisher’s fitness is a measure of “evolutionary success” in that it is a measure of rates of a certain mutation, or

trait, to increase, which is unlike adaptation where the concern is more on whether or not the specific trait is useful for survival [30, 31].

To measure fitness, one can look at the *Malthusian measure*, which is to look at the maximum likeliness for proliferation of a trait in future progeny [32]. To see this mathematically one can analyze the set of dynamical Eq.s in 1.1. The general solutions to these coupled Eq.s are a linear superposition of exponential functions with four multiplicative constants which are determined by initial conditions (initial population density) and two dynamic rates λ_i which are determined by the eigenvalues of the linear system. The largest, positive eigenvalue maximizes for proliferation/growth.

For this particular model, the largest, positive eigenvalue, $\max[\lambda_i] \equiv \lambda(\theta)$, is given by

$$\lambda(\theta) = \frac{1}{2}cp_0 \left\{ \sqrt{\left(\left[\frac{\cos(\theta) - \cos(\theta - \psi)}{\cos(\theta) \cos(\theta - \psi)} \right]^2 + \left(\frac{b}{cp_0} \right)^2 - \frac{\cos(\theta) + \cos(\theta - \psi)}{\cos(\theta) \cos(\theta - \psi)} \right)} \right\} \quad (1.2)$$

When a mutation is fit the likelihood of it being passed on to future progeny is a maximum of the fitness function given above. In this case one would like to know for which values of θ the fitness function has a global maximum. In other words, for which values of θ is $\lambda(\theta)$ a maximum. This fitness criterion leads to

$$\theta_* = \pm \frac{\psi}{2}. \quad (1.3)$$

In other words, the maximum fitness of filament tips of the two population is when filaments are alternating symmetrically in their orientation about the normal of the leading edge membrane [22]. For a branch angle of $\psi \sim 70^\circ$, the leading edge

filaments with alternate with an orientation of $\theta \sim \pm 35^\circ$, thereby agreeing with experiments.

Thermal fluctuations of the filaments have some effect on the branch junction, which has its own thermal stiffness[20]. These fluctuations can be modeled as noise in the branch angle ψ , which may then affect the above optimal result. Incorporating angular fluctuations into the above model is discussed in chapter 2 on page 37.

1.3 Theoretical implications of the DNM: Spatial distribution of filaments

In the previous Sec. (1.2), an optimal orientation of filaments with respect to the leading edge of the lamellipodium was predicted in mean field to be half of the branch angle, which is in accordance with experiment[22]. However, the previous model is a mean field one in that one cannot capture, by construction, any spatial degrees of freedom. Given the results of the previous, one spatial degree of freedom will be addressed, namely the direction along the leading edge.

1.3.1 The Graded Radial Extension Model (GRE) - Relating orientational and spatial degrees of freedom

Cell shape is important during locomotion for a crawling cell. As the keratocyte glides along, takes on a regular canoe-like shape [8, 9, 26, 33]. To make the connection between cell shape and the underlying kinetics of filament polymerization/depolymerization and extension/retraction of the leading edge one has to propose a consistent model that accounts for the average speed of locomotion and distribution of protrusion rates along the leading edge. Two possible scenarios

emerge: 1) All points along the membrane edge move with exactly the same velocity (magnitude and direction) as the cells crawling velocity, this is known as the Parallel Extension(PE) Model; 2). The velocity of points along the leading edge are *graded* and the average velocity (integrated over the membrane) is parallel to the cells crawling velocity, this is known as the Graded Radial Extension(GRE) model [8] (see Fig.1.7). Evidence that supports the GRE model is lamellar ridges rotate away from the lamellipodium apex. Following a point defined by cytoplasmic thick regions, experimentalist found that these ridges move along the edge as a function of time and are eventually retracted at the rear, thus ruling out that all points along the membrane edge move at the same velocity as the cell's velocity [34]. Moreover there is a reasonable explanation for why perhaps the edge speed is graded. Since polymerization is the main driving force behind cell locomotion, a graded edge velocity is expected when polymerization rates have slowed due to membrane resistance in places where actin filament density is less [8, 26]. Hence cell shape/morphology is linked to cytoskeletal dynamics. Moreover, as filaments move across the leading edge due to a geometric lateral flow velocity (discussed in Sec. 1.2) the chance of becoming capped grows in time. Therefore, the density of filaments should decrease at the outer reaches of the leading edge due to capping. This further suggests a graded density of filaments along the leading edge of the lamellipodium [8, 9].

1.3.2 Filament density along the leading edge

To investigate the spatial distribution of filaments one can assume that there are two orientations of filaments, which follows the relation in Eq. 1.3. This will naturally give rise to two populations that alternate in their orientation symmetrically on either side of the normal to the leading edge. The two populations are denoted by p^\pm respectively. Furthermore, in continuing on with the spirit of the DNM

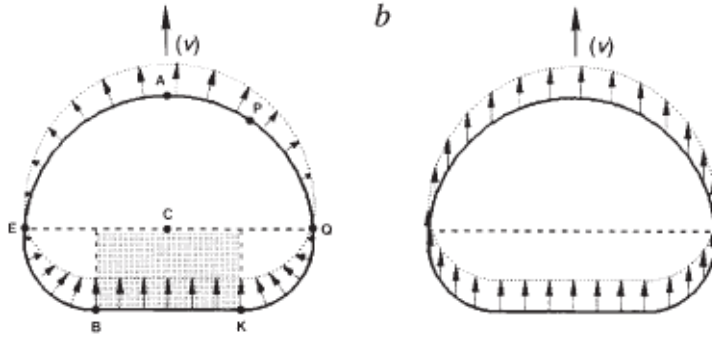


Figure 1.7: Comparison of the GRE model with that of the PE model. [Nature **362**, pg. 167 (1993)]

discussed in Sec. 1.1.5 the two populations of filaments (\pm) along the leading edge of the lamellipodium are coupled via their branch rates, which depends on the total population.

A particular model of filament density which incorporates these properties was constructed by Grimm et al [26] and is stated in the Eq.s

$$\frac{\partial p_{\pm}}{\partial t} = \mp \frac{\partial}{\partial x} (v^{\pm} p^{\pm}) + \beta b_{1,2}(p^{\mp}) - \gamma p^{\pm}. \quad (1.4)$$

The first term on the RHS measures the *lateral flow* of filaments tips along the leading edge. In accordance with the Graded Radial Model discussed in Sec. 1.3.1, for a cell moving at a speed V , the filaments will flow from the apex of the lamellipodium to the “edges” at a rate which determined by purely geometric considerations (see diagram below).

To find the rate at which filaments laterally flow across the leading edge, consider that the profile of the leading edge is determined from a function of both space and time, $f(x, t)$. The lateral speed in this geometry is given by

$$v^{\pm}(x, t) = \frac{\mp \partial f / \partial t}{\partial f / \partial x - \cot(\theta_{\pm})}. \quad (1.5)$$

For details of the calculation see appendix A. Assuming that at the ends, the

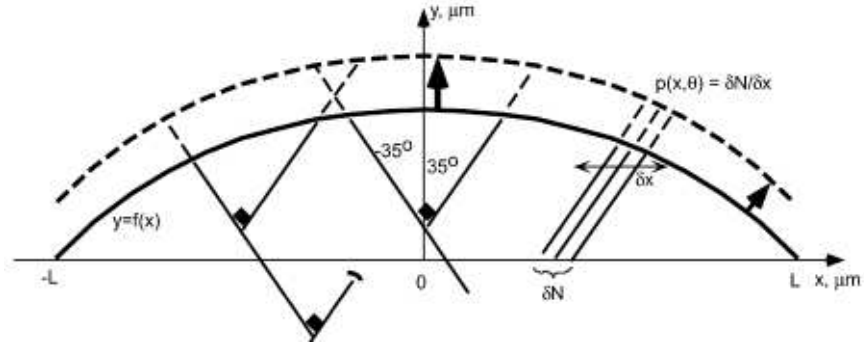


Figure 1.8: Schematic of filament lateral flow due to expansion of the leading edge consistent with the Graded Radial Extension Model. [Eur. Biophys. J., Vol. **32**, p. 563 (2003)].

density of filaments is (for a lamellipodium of length L),

$$p^-(L) = 0, \quad p^+(-L) = 0. \quad (1.6)$$

These boundary conditions specify that, for example, for +(right) oriented filaments (see Fig. 1.8), the density should vanish because +(right) will be polymerizing into the bulk of the lamellipodium and thus not supporting the membrane and will become capped more easily.

The dynamical Eq.s given in Eqs.1.4 predict two types of steady state distributions. The first type is when the value of the boundaries are given by Eqs. 1.6 and is always convex when the capping rate γ is at most comparable to the dimensionless velocity $\epsilon = V/L\gamma$ [9, 26, 33]. This convex profile has been measured using immunofluorescence labeling of F-actin and is given in Fig. 1.9. However, when the boundaries are assumed to have some non-zero value this can generate the second type of distribution which exhibits a concave profile with more filamentous material at the boundaries than in the middle. This suggest that polymerization there would cease and the lamellipodium would collapses [9, 33]. These two density

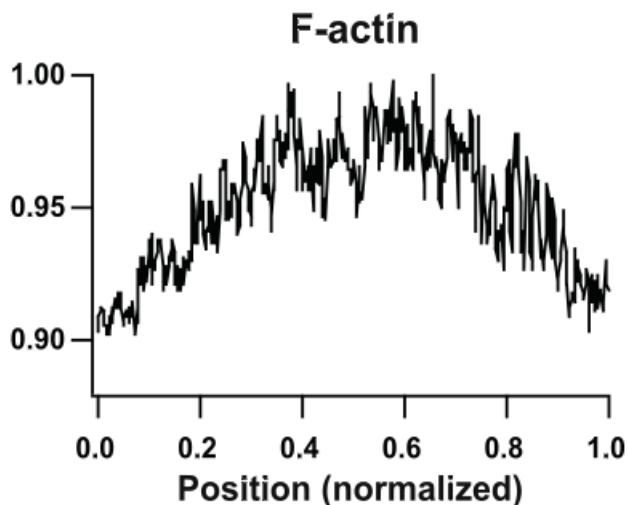


Figure 1.9: Experimentally measured filament distribution of F-actin along the leading edge of a live crawling cell using immunofluorescence labeling. The peak of intensity occurs at the midpoint of the lamellipodium. [PLoS Biol., Vol. **5** p. 2035 (2007)]

profiles will be discussed more in chapter 2 in Sec. 2.2.

1.4 Conclusion to chapter 1

The motion of crawling cells, such as keratocytes, is accomplished from the active forces that are generated by the Brownian ratcheting [4] of filament tips at the leading edge (fig 1.1). As the F-actin lengthens by incorporating G-actin, steric interactions between filament tips and the membrane push with $0.4 pN$ per filament. Collectively the filament network must generate forces of the order of $10 pN$ to move $1 \mu m$ of membrane. Keratocyte membranes are on average about $10 \mu m$ across which would require forces of the order of one hundred piconewtons and observed filament densities easily exceed this force such that the cell can indeed crawl. Furthermore, typical cell speeds ($0.05 - 0.5 \mu s^{-1}$) suggest that the actin polymerization rate would have to be in a range of $\sim 2.0 - 11.0 \mu M^{-1} s^{-1}$, which

is indeed the case for *in vivo* measurements [22].

To accomplish the high degree of actin polymerization needed for typical cell speeds the cell must nucleate new F-actin material at the leading edge. This is accomplished by branching new material off of existing filaments via the activated Arp2/3 protein complex [6, 15]. Following the framework *Dendritic Nucleation Model*(DNM)[6], Arp2/3 is activated at or near the membrane leading edge where actin is polymerized into minifilaments (dimers and trimers) where Arp2/3 prevents depolymerization of the newly formed minifilaments. Mini-filaments are then integrated into the existing network at a rate of 0.43 s^{-1} [16]

The Arp2/3 protein induces a regular branch angle of roughly 70° between the plus ends of the mother and daughter filaments [15, 16, 22]. This branch angle produces a preferred orientation of filament tips with respect to the leading edge membrane of half of the branch angle symmetrically on either side of the membrane normal (see Eq.s 1.2 and 1.3) [16, 22, 33]. Filaments in the network can also become capped, which arrests any further polymerization and eventually become severed/disassembled and recycled into the available free monomer solution. The overall process forms a dendritic array of filaments in the network as predicted by the DNM 1.1.5 (See Figures 1.3 and 1.5).

Population models described in Sec. 1.1 representing the number density of mother and daughter F-actin in the network also exhibit a preferred optimal orientation that is also governed by Eq. 1.3). Furthermore, this orientation is still preferred even in the presence of noise as discussed in the upcoming chapter.

Assuming the optimal orientation ($\theta = \pm\psi/2$) is the preferred one, spatial degrees of freedom of filaments along the leading edge are explored (See Sec. 1.2). As

the leading edge is propelled forward via the Brownian ratcheting (see Fig. 1.4) of filaments polymerizing at the leading edge. Filaments with either plus(+) or minus(-) orientation laterally flow along the leading edge toward the rear of the cell. The density at any location is determined by this flow velocity and the local/global branching and capping rates as well as the filament density at the boundary (discussed in Sec. 1.2). The filament density profile provides the cell with its characteristic shape (see Figs 1.1 and 1.3), since the protrusion rate is directly related to the polymerization rate and hence the density of filaments at any position along the membrane edge.

To summarize, the process of filament branching provides for a large enough filament density to extend the membrane, assuming that the pushing force of one filament is simply scaled by the number of unbranched filaments. In addition, the branching not only helps establish the morphology of the network but also the spatial distribution of filaments, which gives the cell shape during locomotion. Moreover, branching may have an additional role in that it could facilitate a more rigid structure by increasing the chance for filament overlaps and locations for crosslinking neighboring filaments together (see Chapter 2, Sec. 2.2.2) [35]. Branching may even lead to direct consequences for the “extreme” mechanics of these networks which has been already experimentally observed [36]. Of course, morphology helps determine rheology, which, in turn, affects the morphology. Finally, in the next chapter, we explore morphological implications of the branching of Arp2/3 based on assumptions that differ somewhat from the ones presented in this chapter.

To understand how the different properties fit together in these systems is to, for the time being, perform a piecewise analysis and invoke the approximation that the pieces are the sum of their parts. To quote Thompson,

Whether they do or do not, it is plain that we have no clear rule or guidance as to what is “vital” and what is not; the whole assemblage of so-called vital phenomena, or properties of the organism, cannot be clearly classified into those that are physical in origin and those that are sui generis and peculiar to living things. All we can do meanwhile is to analyze, bit by bit, those parts of the whole to which the ordinary laws of the physical forces more or less obviously and clearly and indubitably apply [1]. – D’Arcy Wentworth Thompson

Chapter 2

Optimal Orientation of Branched Cytoskeletal Filaments

The process of cell motility involves a number of components—the actin cytoskeleton, the cellular membrane, an assortment of actin-binding proteins, molecular motors and integrins—that assist the cell in changing shape so that it can move in a particular direction [37]. Naturally, one assumes that the interplay between the various components has been tuned to form structures that optimize for efficient motility. To test this assumption quantitatively is not necessarily an easy task given the dynamically complex structures that emerge as a cell crawls. However, theoretical descriptions of complex biological systems rooted in simplicity may help to identify key interactions so that the sophistication of cell motility may be better quantitatively understood [38, 39].

In order for the cell to crawl in a particular direction, the cell extends itself. This extension, otherwise known as the lamellipodium, is facilitated by the growth and restructuring of the actin cytoskeleton. Over the past ten years or so, the dendritic nucleation model has emerged as the dominant conceptual picture of

this reorganization [6, 40]. The dendritic nucleation model asserts that cytoskeletal growth is initiated by membrane-bound proteins, such as PIP_2 , that activate WASP. WASP, in turn, activates Arp2/3, a protein that nucleates new filaments from preexisting ones. At the point of nucleation, the branch angle takes on a somewhat regular angle of 70 degrees with respect to the mother filament [6, 15]. This nucleation takes place at/near the cell membrane and leads to a tree-like, or dendritic structuring of the actin cytoskeleton.

New filament growth must be accompanied by some system of regulation, since unregulated birth of branched actin filaments can lead to a redundant use of finite resources in a cell. It has been shown in purified reconstituted systems that Arp2/3 and G-actin alone are insufficient for motility [41, 42]. Additional regulation of the existing actin cytoskeleton is required for rapid G-actin turnover. This regulation is partially assisted by capping proteins, which attach to the plus ends of filaments and stop polymerization. In other words, the filament dies. Also, filaments further back from the leading edge debranch and get severed, eventually becoming part of the finite pool of G-actin. All of these processes are qualitatively described by the dendritic nucleation model. For a unified quantitative description of such processes see Ref. [43].

Using the branching (birth) and capping (death) processes as a basis for formation of lamellipodia, we give quantitative evidence to support the notion that form/morphology of the dendritic network is optimized to facilitate cell motility. More specifically, we propose a mean field model for the birth and death rates as a function of filament orientation with respect to the leading edge. We then optimize for filament reproduction at the leading edge, which provides an optimal relation between the branch angle and the angle with respect to the leading edge that agrees with experimental observation [15].

We must point out that there exists an earlier mean field model, which predicts

the same optimal relation between the branch angle and the angle of orientation with respect to the leading edge. However, the earlier model has a different physical basis [22]. In keeping with the scientific method, we study further implications of the two models in order to make other retrodictions/predictions to distinguish them. For example, by studying the implications of our model on the spatial organization of filaments, we propose a new shape for the filament density along the leading edge. The shape may account for an observed “excess” filament density along the outer edges of the lamellipodia beyond what current modeling predicts [33]. We also make comparisons with a more recent orientational model [44].

Finally, our analysis of spatial information allows us to investigate a recent experimental study of lamellipodia made by Urban and collaborators using electron tomographic images of cytoskeletal networks [35]. They found that overlapping actin filaments were much more prevalent than branched filaments. Based on this data, they proposed an alternate model for the reshaping of actin filaments near the leading edge—that polymerization and cross-linking are the main ingredients for cellular extension and not Arp2/3, which is relegated to a non-branching nucleating agent of new filaments just as dimerization nucleates new filaments. We implement a discrete, spatial simulation of our model to measure, for example, the ratio of overlaps to branch points to determine if the prevalence of overlaps rules out the dendritic nucleation model. We also use the full two-dimensional spatial information of the filament tips to discuss implications for the buckling of the network.

The paper is organized as follows: Section II introduces and analyzes the mean field, orientational birth-death model. Comparisons with earlier mean field models, as well other generalizations, are addressed. Fluctuations about the mean field solutions are investigated. Section III studies the coupling between the orientational degrees of freedom and the spatial degrees of freedom, such as analyzing

the full two-dimensional information of filament positions via discrete simulations. Section IV discusses the implications of our results.

2.1 Mean field models

2.1.1 Collision-based model

Actin filaments contain an inherent polarity where actin monomers associate with the plus end of the filament and dissociate from the minus end [45, 46, 47]. This polarity allows for directed assembly such that the cell can extend itself in a particular direction. While extension via polymerization is one mechanism for extension, the dendritic nucleation model [6, 40] asserts that extension via nucleation of branched filaments off pre-existing ones is also important. Support for the dendritic nucleation model has come about, for example, from electron micrograph images [15] of branched actin networks in lamellipodia, from the knocking out of Arp2/3 preventing the formation of lamellipodia [19] and from reconstituted systems of purified proteins [41]. In these reconstituted systems, motility can be induced by using a small number of purified proteins combined *in vitro* which can reach speeds, for optimal concentrations, of $2.2 \mu\text{m min}^{-1}$. It was observed that motility cannot occur with activated Arp2/3 alone. Additional proteins, which facilitate a *steady state* of G-actin concentration, are essential [41]. These proteins are capping proteins, which cap polymerizing plus ends and ADF/Cofilin, which cuts actin filaments. Both proteins help replenish the G-actin pool.

To test some of the dendritic nucleation model assertions, let us construct a mean field model with branching and capping and investigate various experimental consequences. As for the branching, *in vitro* studies suggest a preferred angle of 70° with respect to the plus end of the mother filament [6]. Therefore, for now, we assume that the branching angle is some fixed angle ψ from the plus end.

We will also assume that Arp2/3 branches off the side of pre-existing filaments with a preference towards the plus end as has been observed experimentally [48]. Moreover, we assume that the nucleation of a branch occurs at and/or very near the membrane. Of course, if branching takes place only at the membrane, then the initial structure of the network is dictated by the shape of the membrane. If the Arp2/3 is released from the membrane upon activation and then collides (binds) with actin filaments, then the network structure is less dependent on the shape of the membrane. Recent experiments observed space-filling polymerization of filopodia into gaps between the edge of the network and the membrane [49]. Such an observation has to yet found with Arp2/3 nucleation, however.

So, assuming that side-branching occurs and that the branch is nucleated at/near the membrane, the branching probability depends on the orientation of the filament. The more the filament is parallel with the leading edge, the higher the cross-section for collision between the globular Arp2/3 and the one-dimensional filament and, hence, nucleation. More precisely, the branching rate contains a $|\sin(\theta)|$ dependence, where $\theta = 0^\circ$ is normal to the leading edge.

As for the death rate, filament plus ends get capped at a rate c . We will not assume any angular dependence for the capping rate. The capping protein-plus end binding is a globular-to-globular collision. Furthermore, the task of the capping protein is to regulate the length of filaments such that growth is channeled into developing new filaments and not into extending pre-existing ones [50]. Elongating pre-existing filaments leads to a system longer filaments on average, which are more susceptible to buckling [51]. Channeling new filament growth should, therefore, be independent of filament orientation. In addition, channelling growth into branches allow for further spreading of lamellipodia, which increases cell contact with the surface in order to build more focal adhesions.

Based on the above assumptions, we construct a set of kinetic equations that

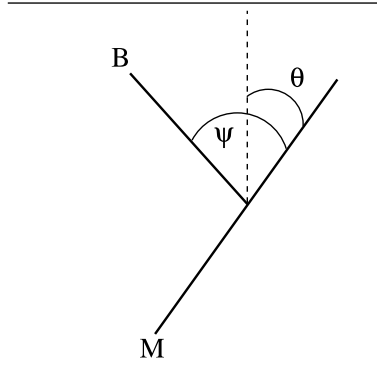


Figure 2.1: Schematic of the orientation of a branched filament (B) in relation to its mother filament (M) and the horizontal line denotes the leading edge.

take into account the orientation of filaments, which branch off preexisting filaments and get capped. We restrict ourselves to $-90^\circ < \theta < 90^\circ$ since we are only interested in “forward” growth. We first consider $\psi > 45^\circ$ and $0^\circ < \theta < \psi$. In this regime, there are two populations of filaments, filaments oriented at angle θ , denoted by n_1 , and filaments oriented at an angle $\theta - \psi$, denoted by n_2 . (There is a reflection symmetry about $\theta = 0^\circ$. We will only deal with $0^\circ < \theta < 90^\circ$ and use the reflection symmetry to extend our results to $-90^\circ < \theta < 0^\circ$.) The kinetic equations for this first case are

$$\frac{dn_1}{dt} = \frac{b}{2} |\sin(\theta - \psi)| n_2 - cn_1 \quad (2.1)$$

and

$$\frac{dn_2}{dt} = \frac{b}{2} |\sin(\theta)| n_1 - cn_2, \quad (2.2)$$

where b denotes the magnitude of the branching rate. The factor of $1/2$ is because branching on the “backside” of the mother filament is a less-likely collision given the activation of Arp2/3 at the membrane and we do not consider it here.

We now rephrase famous “the form follows function” optimization guideline as a population biology problem [52, 32, 31]. We assume the cytoskeletal system is

maximizing for “population” growth so that the cell can extend itself efficiently. To determine this maximal growth, we compute the eigenvalues for the above set of equations and determine the relationship between θ and ψ such that the largest of the two eigenvalues is maximized (and positive). The eigenvalues for the above set of equations are

$$\lambda_{1,2} = -c \pm \frac{b}{2} \sqrt{|\sin(\theta)| |\sin(\theta - \psi)|}. \quad (2.3)$$

It is easy to see that the largest eigenvalue is maximized when $\theta^* = \psi/2$. Of course, $\theta^* = -\psi/2$ is another optimal solution via symmetry.

Next, we investigate $\psi < \theta < 90^\circ$ (and $\psi > 45^\circ$). In this second regime, there are three orientations of filaments with n_3 denoting filaments oriented at $\theta - 2\psi$. The set of kinetic equations for this second case are

$$\frac{dn_1}{dt} = \frac{b}{2} |\sin(\theta - \psi)| n_2 - cn_1, \quad (2.4)$$

$$\frac{dn_2}{dt} = \frac{b}{2} |\sin(\theta)| n_1 + \frac{b}{2} |\sin(\theta - 2\psi)| n_3 - cn_2, \quad (2.5)$$

$$\frac{dn_3}{dt} = \frac{b}{2} |\sin(\theta - \psi)| n_2 - cn_3. \quad (2.6)$$

Once again, assuming activation of Arp2/3 at the membrane, nucleation is unlikely to occur on the “backside” of a mother filament with respect to the membrane and the kinetic equations become

$$\frac{dn_1}{dt} = -cn_1, \quad (2.7)$$

$$\frac{dn_2}{dt} = \frac{b}{2}|\sin(\theta)|n_1 + \frac{b}{2}|\sin(\theta - 2\psi)|n_3 - cn_2, \quad (2.8)$$

$$\frac{dn_3}{dt} = \frac{b}{2}|\sin(\theta - \psi)|n_2 - cn_3. \quad (2.9)$$

The n_1 population eventually dies off such the above equations simplify further to

$$\frac{dn_2}{dt} = \frac{b}{2}|\sin(\theta - 2\psi)|n_3 - cn_2, \quad (2.10)$$

$$\frac{dn_3}{dt} = \frac{b}{2}|\sin(\theta - \psi)|n_2 - cn_3. \quad (2.11)$$

With the transformation of $\theta' = \theta - \psi$, we map back to the first set of kinetic equations such that the largest, positive eigenvalue occurs again at $\theta'^* = \pm\psi/2$. If $\psi = 45^\circ$, there exists another optimum at $\theta^* = 67.5^\circ$. However, this initial orientation will die away and the $\pm 22.5^\circ$ will survive. So we have the same optimization as in the first case, i.e. it is redundant. This result is different from the initial model [22], where the optima occur at $\theta = 0^\circ, \pm\psi$. Of course, for $\theta = 0^\circ$, the critical buckling load is the smallest, i.e. filaments are more susceptible to buckling. While this property is not optimal for rheology, bundled filaments can increase the critical buckling load [53]. For our model, there can be no optimum at $\theta = 0^\circ$.

If we increase ψ beyond 60° , the second optimization peak is outside of the range of interest ($\psi < \theta < 90^\circ$). However, consider $\psi = 70^\circ$. As θ increases from 70° to 90° , the reproductive growth enhances monotonically. For $\theta = 90^\circ$, the daughter filaments are subsequently oriented at 20° and -50° . While these initial

90° filaments are not precisely optimized for growth, their growth is maximum for the interval, $\psi < \theta < 90^\circ$. Therefore, we deem these 20° and -50° filaments as suboptimal orientations. Figure 2.2 depicts the optimal orientations and the suboptimal, or subdominant, orientations. We conjecture that the subdominant orientations of filaments may serve as reinforcements for cross-linking. Depending on the initial spatial arrangement and orientation of the filaments, the subdominant orientations may help to increase overlaps and spreading. It is interesting to note that only for $\psi > 60^\circ$, the second redundant optimum is removed. The observed branch angle is reasonably close to this value.

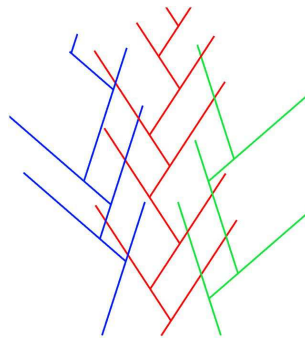


Figure 2.2: Depiction of the optimal orientation (red) and the two suboptimal ones (blue, green).

Experiments on keratocytes have measured the distribution of orientation of filaments normal to the leading edge [22]. There are two maxima in the distribution occurring at $\pm 35^\circ$. Assuming that the branch angle is indeed 70° , our optimization analysis provides an explanation for this experimental finding. However, we should mention that Koestler and collaborators have conducted a more recent experiment on the orientation of filaments [54]. They observed a broad distribution between the angles of -75° to 75° . One could argue that the subdominant orientation of filaments could account for further spreading of the distribution and, therefore, perhaps the more recent data.

2.1.2 Comparison with other models

How does the above model compare with the one constructed and analyzed by Maly and Borisy [22] (This model is discussed in chapter 1 in section 1.2)? The Maly/Borisy model is consistent with the Brownian ratchet model [4, 5] for filament elongation near a membrane. In the Brownian ratchet model, leading edge filaments polymerize only if there exists enough space between the membrane and the tip of the filament. As the filaments fluctuate, transient gaps open up between the filament and the membrane, allowing actin monomers to attach to the plus end of the filament. Once the filament bends back to its original straight configuration, it is now longer and, therefore, pushes against the membrane moving it forward. This process, however, is limited to the size of the fluctuations that occur between the membrane and the tip of the leading edge filament. In support of this notion, experiments involving changing the membrane tension have shown that there exists an inverse relationship between the lamellipodial extension velocity and the apparent membrane tension [55]. However, more recent experiments suggest more complicated mechanisms may be at play [28].

Given the space limitation between the membrane and the fluctuating tip, there is an orientational degree of freedom that the filaments can exploit in this polymerization process. By varying the angle at which the tip makes with the membrane initially, the amount of space between the two can change if the membrane moves forward over a time t at a velocity v_{mem} . In particular, $\delta k_p \rho_m p \cos(\theta) = v_{mem}$, where δ is the G-actin diameter, k_p is the polymerization rate, ρ_m is the G-actin concentration, and p is the probability that the filament tip is not obstructed by the membrane. Maly and Borisy [22] assert that the capping of a filament is only possible if the growing filament tip is not obstructed by the membrane, hence capping occurs at a rate cp . Since $p \propto 1/\cos(\theta)$, the larger θ is, the more likely the filament will be capped.

As for the branching, in the Maly/Borisy model, the branching rate does not contain any angular dependence. In other words, the kinetic equations read

$$\frac{dn_1}{dt} = \frac{b}{2}n_2 - \frac{cp_0}{\cos(\theta)}n_1 \quad (2.12)$$

$$\frac{dn_2}{dt} = \frac{b}{2}n_1 - \frac{cp_0}{\cos(\theta - \psi)}cn_2, \quad (2.13)$$

where $p_0 = v_{mem}/\delta\rho_mk_p$. Maly and Borisy show that for $\cos(\psi) < p_0 < \cos(\psi/2)$, the optimal relation between θ and ψ is, as above, $\theta^* = \pm\psi/2$. However, for $p_0 < \cos(\psi)$, the optimal orientations are zero and $\pm\psi$.

A more recent orientational model assumes a θ -independent, zeroth-order branching rate, a θ -independent, first-order capping rate, and a θ -dependent outgrowth rate that kills single filaments outgrowing the bulk of the network [44]. The model exhibits two different, stable patterns, the same two exhibited by Maly and Borisy [22], $\theta = \pm\psi/2$ or $\theta = 0, \pm\psi$. The two patterns cannot coexist. Parameters such as the capping rate determine which pattern prevails. The authors argued that their model can explain the experimentally observed load-dependence of the network velocity at a given force [56]. Our model cannot exhibit the latter pattern and our subdominant pattern for $\psi > 60^\circ$ does coexist with the primary, or optimal, one.

2.1.3 Generalized birth/death rates

While each mean field model has a different physical basis, the selection criterion for maximal growth yields the same optimal relationship, $\theta^* = \pm\psi/2$. How generic is this result? To begin to answer this, we consider the most general version of our population equations such that both the birth-rate and the death-rate depend on

the orientation of the branched filaments. Therefore, we begin with

$$\frac{dn_1}{dt} = B_1(\theta, \psi)n_2 + D_1(\theta, \psi)n_1 \quad (2.14)$$

$$\frac{dn_2}{dt} = B_2(\theta, \psi)n_1 + D_2(\theta, \psi)n_2, \quad (2.15)$$

for $0^\circ < \theta < 90^\circ$. We define the matrix, $\mathbf{Q} \equiv \mathbf{Q}(\theta, \psi)$ such that we can represent the set of linear coupled equations vectorially as $\dot{\mathbf{n}} = \mathbf{Q}\mathbf{n}$, where

$$\mathbf{Q} = \begin{pmatrix} D_1(\theta, \psi) & B_1(\theta, \psi) \\ B_2(\theta, \psi) & D_2(\theta, \psi) \end{pmatrix}. \quad (2.16)$$

Defining $\bar{\mathbf{Q}} = \mathbf{Q}/\text{Det}[\mathbf{Q}]$, the eigenvalues of $\bar{\mathbf{Q}}$ are given by

$$\lambda_{+,-} = \frac{\text{Tr}[\bar{\mathbf{Q}}] \pm \sqrt{\text{Tr}[\bar{\mathbf{Q}}]^2 - 4}}{2}. \quad (2.17)$$

With this result, three scenarios emerge:

<i>Condition</i>	<i>Eigenvalues</i>
(1) $ \text{Tr}[\bar{\mathbf{Q}}] < 2$	$\lambda_{+,-} \rightarrow \mathbb{C}$
(2) $ \text{Tr}[\bar{\mathbf{Q}}] = 2$	$(\lambda_+ = \lambda_-) \rightarrow \mathbb{R}$
(3) $ \text{Tr}[\bar{\mathbf{Q}}] > 2$	$(\lambda_+ > \lambda_-) \rightarrow \mathbb{R}$

(2.18)

To determine the largest, real eigenvalue, we focus on condition 3. Dropping the +,- notation, the optimization condition is determined by

$$\partial\lambda = \text{Tr}[\partial\bar{\mathbf{Q}}] \left(1 + \frac{\text{Tr}[\partial\bar{\mathbf{Q}}]}{2\sqrt{\text{Tr}[\bar{\mathbf{Q}}]^2 - 4}} \right) = 0 \quad (2.19)$$

such that

$$\text{Tr}[\partial_\theta \overline{\mathbf{Q}}] = 0. \quad (2.20)$$

In other words, the optimization condition occurs when the matrix $\partial_\theta \overline{\mathbf{Q}}$ is rendered traceless. One, of course, also needs to evaluate the second derivative to check for a maximum.

With the help of the Jacobi formula for the derivative of the determinant of a matrix and using the linearity of the trace operator, the optimization condition for \mathbf{Q} must satisfy (assuming the trace of $\partial_\theta \mathbf{Q}$ is zero),

$$\text{Tr}[\mathbf{Q}^{-1} \partial_\theta \mathbf{Q}] = 0. \quad (2.21)$$

If we analyze the case where the two death rates are θ -independent, then the optimal condition is

$$\partial_\theta (B_1(\theta, \psi) B_2(\theta, \psi)) = 0. \quad (2.22)$$

For example, if $B_1(\theta, \psi)$ is ψ -independent and $B_2(\theta, \psi) = B_1(\theta - \psi)$, then the optimal condition is $\theta^* = \psi/2$ as long as $B_1(\theta)$ is an even function (provided the second derivative is negative at that point). If B_1 is a trigonometric function, then the periodicity should not be too small such that other maxima appear within the $0^\circ < \theta < 90^\circ$ range. So, $B_1 = \cos(\theta)$ yields the same optimal relation between θ and ψ as would many other functions. It is possible to broaden this analysis. We leave this for future work. Our point now is that the optimal finding of $\theta^* = \pm\psi/2$ alone just not necessarily justify the model. One needs to explore further implications of the model in order to distinguish it from other potential models. We shall pursue this tact in the next section.

2.1.4 Fluctuations

Is the optimal relationship between θ and ψ robust in the presence of fluctuations? To answer this question, following Maly and Borisy [22], we assume that the angle between the two types of filaments exhibits Gaussian fluctuations with a mean of ψ and a variance of σ^2 . If we define $n(\theta, t)$ as the density of filaments at the leading edge at time t and orientation θ , then the dynamic equation for $n(\theta, t)$ (for $-\psi < \theta < \psi$) is given by

$$\frac{\partial n(\theta, t)}{\partial t} = \frac{b|\sin(\theta)|}{\sqrt{8\pi}\sigma} \int_{-\psi}^{\psi} (e^{-\frac{(\theta'+\psi-\theta)^2}{2\sigma^2}} + e^{-\frac{(\theta'-\psi-\theta)^2}{2\sigma^2}}) n(\theta', t) d\theta' - cn(\theta, t). \quad (2.23)$$

In steady state $n(\theta, t \rightarrow \infty) \equiv q(\theta)$, we arrive at

$$\frac{|\sin(\theta)|}{\sqrt{8\pi}\sigma} \int_{-\psi}^{\psi} (e^{-\frac{(\theta'+\psi-\theta)^2}{2\sigma^2}} + e^{-\frac{(\theta'-\psi-\theta)^2}{2\sigma^2}}) q(\theta') d\theta' = \frac{c'}{b'} q(\theta), \quad (2.24)$$

where $\frac{c'}{b'}$ is now an unknown eigenvalue such that the above assumption is justified. We use the quadrature method to numerically solve for $q(\theta)$ for different values of σ . Figure 2.3 depicts the results. The maximum of $q(\theta)$ correspond well with the largest, positive eigenvalue found previously. As σ increases, the maxima remain robust, but are become less pronounced. These results indicate that the optimal relation of $\theta^* = \pm\psi/2$ is robust to fluctuations.

It is certainly worth comparing this result with the fluctuation results of Maly and Borisy [22]. The steady state orientation in the presence of noise here is very similar to the Maly/Borisy model [22], at least for intermediate values of p_0 . This new computational result is, therefore, somewhat nontrivial given that one would assume the fluctuations to be sensitive to the details of the underlying kinetics. Further investigation along the lines of Section IIc is needed to pursue understanding of this possible genericity despite differing details of the kinetics.

2.2 Orientation influencing spatial organization

2.2.1 Filament density profile along the leading edge

Optimization for growth in lamellipodia leads to a relationship between the branch angle ψ and the orientation of filaments relative to the leading edge, or θ . To date, there exist three models, each rooted their in own physical basis, that yield $\theta^* = \pm\psi/2$. In order to further differentiate between these models, we investigate the distribution of filament tips along the leading edge.

Previous work investigating the filament density along the leading edge has invoked the following set of assumptions [26, 9, 33]. Filaments are either oriented with $+35^\circ$ or -35° with respect to the leading edge. Their respective densities along the leading edge x are denoted by $\rho^+(x, t)$ and $\rho^-(x, t)$. These filaments undergo lateral flow in their respective directions. Filaments with either orientation can spawn filaments with the opposite orientation ($\pm \rightarrow \mp$) from their own. Also, both types of filaments can get capped. Therefore, the equations for both filament densities along the leading edge, whose position is denoted by x , are

$$\frac{\partial \rho^\pm}{\partial t} = \mp \frac{\partial}{\partial x}(v\rho^\pm) + \frac{b}{B}\rho^\mp - c\rho^\pm \quad (2.25)$$

with $B = \int_{-L/2}^{L/2} dx(\rho^+(x) + \rho^-(x))$, where L is the length of the lamellipodium and v is the lateral flow speed, which is proportional to the speed of the crawling cell.

Previous analysis of the above equation yields a total filament density in steady state that is peaked at the center of the cell, provided the filament density at the edges is sufficiently small. More specifically, for the boundary conditions, $\rho^+(-L/2, t) = 0$ and $\rho^-(L/2, t) = 0$, $\rho_+(x, t \rightarrow \infty) + \rho_-(x, t \rightarrow \infty) = \frac{\pi b}{2 Lc} \cos(\frac{\pi x}{L})$. Therefore, near the center the profile is an inverted parabola [9, 33]. If the boundary condition is adjusted to a higher concentration, eventually, the inverted parabola becomes a parabola with the total filament density higher at the sides

than in the center. Assuming $\frac{v}{L} \ll c$, we define a dimensionless time, $\tau = ct$, a dimensionless position $s = x/L$, and dimensionless densities, $\tilde{\rho}^\pm = \rho^\pm \frac{cL}{b}$, then Eq. 25 becomes

$$\frac{\partial \tilde{\rho}^\pm}{\partial \tau} = \mp \frac{\partial}{\partial s} \left(\frac{v}{cL} \tilde{\rho}^\pm \right) + \frac{1}{\tilde{B}} \tilde{\rho}^\mp - \tilde{\rho}^\pm. \quad (2.26)$$

If the boundary conditions at the ends of the lateral extent demand a large enough density, then the system will not be able to sustain the peak in density at the center of the leading edge. The larger the branching rate, the higher the allowed density at the ends can be with the system still sustaining an inverted parabola.

The inverted parabola in filament density along the leading edge is observed in experiments near its center [33]. However, there is an excess of the filament density towards the sides of the leading edge ($-L/2$ and $L/2$) that appears to be flat. This excess has not been accounted for in the current model. In light of the collision-based model introduced here, we propose that for $\psi < \theta < 90^\circ$ with $\psi \approx 70^\circ$, the subdominant pattern, whose growth is prevented from being fully optimized so as not to form a redundant pattern, may account for this excess. The axis of the subdominant pattern is at $\theta = -15^\circ$ as opposed to $\theta = 0^\circ$. There exists another pair centered at $\theta = 15^\circ$ by symmetry.

To test this proposal, we take the simplest approach by constructing the following six equations taking into account the two center populations (as before) and the two respective pairs of subdominant, or “off-center”, populations. For now, each respective pair of populations is not coupled to any other respective pair. Each pair occupies its own region along the lateral extent of the lamellipodia. We denote ρ_c^\pm as the original set, ρ_l^\pm as those directed toward the left side of the leading edge (from the birdseye perspective of cell), and ρ_r^\pm as those directed toward the right side of the leading edge to arrive at

$$\frac{\partial \rho_c^\pm}{\partial t} = \mp \frac{\partial}{\partial x}(v\rho_c^\pm) + \frac{b}{B_c}\rho_c^\mp - c\rho_c^\pm \quad (2.27)$$

$$\frac{\partial \rho_l^\pm}{\partial t} = \mp \frac{\partial}{\partial x}(v\rho_l^\pm) + \frac{b_2}{B_l}\rho_l^\mp - c\rho_l^\pm \quad (2.28)$$

$$\frac{\partial \rho_r^\pm}{\partial t} = \mp \frac{\partial}{\partial x}(v\rho_r^\pm) + \frac{b_2}{B_r}\rho_r^\mp - c\rho_r^\pm \quad (2.29)$$

where $B_c = \int_{-\frac{L}{4}}^{\frac{L}{4}} dx(\rho_c^+(x) + \rho_c^-(x))$, $B_l = \int_{-\frac{L}{2}}^0 dx(\rho_l^+(x) + \rho_l^-(x))$, and $B_r = \int_0^{\frac{L}{2}} dx(\rho_r^+(x) + \rho_r^-(x))$. Note the different spatial regions for each respective pair of populations. Of course, the delineation is not so clear cut in practice. Also, $b_2 < b$ to allow for a slight decrease in branching at the edges of the leading edge. Finally, we assume v does not vary between the different pairs.

To solve for the steady state filament density distribution, we use the following boundary conditions. We set $\rho_c^+(-L/4, t) = 0$, $\rho_c^-(L/4, t) = 0$, $\rho_r^+(0, t) = 0$, $\rho_r^-(L/2, t) = \rho_0$, $\rho_l^-(0, t) = 0$, $\rho_l^+(-L/2, t) = \rho_0$. As for the asymmetric boundary conditions on ρ_r^\pm and ρ_l^\pm , it is reasonable to assume that near the lateral center of the leading edge, the density of $\rho_r^+(0, t) = 0$. However, towards the sides of the leading edge, $\rho_r^-(L/2, t)$ may not necessarily vanish as there may be some skewing of the axis along which the subdominant populations are propagating due to the focal adhesions. The same goes for ρ_l^+ . For the symmetric boundary conditions for ρ_c^\pm , the same cosine steady state solution exists as before (only over a smaller interval). For the ρ_r^\pm and ρ_l^\pm populations, the steady state solutions are sinusoidal. (If $\rho_r^+(0, t) = \rho_1 \ll 1$, then the steady state solution is a linear combination of sine and cosine). These solutions are plotted in Figure 2.4. We use $\frac{v}{Lc} = 0.01$, $b_2 = 0.6b$, and $\tilde{\rho}_0 = 0.3$. Typical lateral speeds are of order 0.1 microns/sec for fast-moving keratocytes, typical lengths of leading edges are tens of microns and typical capping rates are tenths per second to per second [26, 40]. We have also checked these solutions numerically.

When we sum up the various densities to arrive at the total density, we can account the observed excess filament density at the lateral edges of the lamellipodium while still having the overall proper shape found experimentally near the center of the system. Indeed, there is a small dip in the center of the system, this dip may be difficult to observe experimentally and is presumably washed out once noise and other details are incorporated into the modeling. For instance, the revised model may be further updated to include coupling between the different populations via branching in terms of the overlapping regions. We leave this for future work. We should also note that the two previous orientational models, at least for $\theta^* = 0^\circ, \pm\psi$, would yield a filament density distribution that is sensitive to the initial distribution of filaments along the leading edge since the $\theta = 0^\circ$ does not flow laterally. Such a sensitivity should be investigated in order to rule out the possibility of the $\theta = 0^\circ, \pm\psi$ pattern.

2.2.2 Two-dimensional, discrete simulation

To further study how filament orientation affects the spatial distribution of filaments, we construct a two-dimensional kinetic simulation with explicit filaments. A two-dimensional approach is reasonable given that lamellipodia are typically flat structures with a thickness of approximately 100 nanometers, extending several microns into the body of the cell and approximately 10 microns across the cell. The simulation algorithm is as follows:

- (0) Initialization: A filament is initialized at the origin of the system with an angle θ and a length 100 nm.
- (1) Branching: A random number, r , is chosen from the sine distribution. Should $r < \sin(\theta)$ (with $\theta < 90^\circ$), a branch point is chosen along the initial filament. Where the branch point occurs is uniformly chosen over some part of the current

filament length as measured from the growing end. The length is denoted by f . This constraint restricts the branching to occur near the leading edge of the network. The branch filament emerges at an angle ψ with respect to the mother filament. Gaussian fluctuations about the branch angle, with variance σ^2 , are also studied.

(3) Capping: A random number, s , is chosen uniformly between zero and unity. If $s < c$, the filament gets permanently capped and no longer extends. Also, no further branching can occur along it.

(4) Every uncapped filament grows by an additional 100 nm in its initially chosen direction (polymerization).

(5) Steps (1)-(4) are repeated for each uncapped filament until capped.

Figure 2.5 demonstrates output from the simulation for a branching angle of 70 degrees with $\sigma = 10^\circ$. Note that we do not explicitly incorporate a membrane into the simulation and we allow for overlaps of filaments due to the thin, third dimension. Also, unless specified otherwise, the time step in the simulation is 0.30 seconds, assuming a constant G-actin concentration of $10 \mu M$, the branch rate is $33.33 s^{-1} \mu m^{-1}$ and the capping rate is $0.83 s^{-1}$ [26, 40].

Growth: We first investigate the optimal relation between θ and ψ . In keeping with the mean field analysis, we compute the average number of uncapped filaments generated each time step, denoted as G , with an upper bound of 1000 filaments. Note that here we do not distinguish between the two populations, mother and daughter. If the average number of uncapped filaments grows with time, the growth is exponential. Of course, eventually, the system reaches a steady state presumably due to a finite amount of Arp2/3 or other mechanisms. To study the approach to steady state, one must incorporate recycling of G-actin monomers via depolymerization, severing and debranching as well. Such mechanisms have

been explored by the autocatalytic model developed by Carlsson [57]. In the autocatalytic model, there is an initial overshoot in the number of filaments that has now been observed experimentally [58].

We present measurements of G , averaged over 4000 samples, as a function of θ . Unless otherwise specified, $f = 25$ nanometers. We observe in Figure 2.6 that the optimal relation, $\theta^* = \pm\psi/2$, holds in the two-dimensional simulations. We also see evidence of the subdominant population of filaments for $\theta > \psi$. For $\psi = 70^\circ$, the growth at $\theta = 90^\circ$ is more comparable to the growth at θ^* than for $\psi = 80^\circ$. Again, perhaps the subdominant pattern for $\theta = 90^\circ$ contributes to increased spreading and/or overlaps between generations following the initial filaments. For a smaller capping rate, more growth occurs as evidenced in Figure 2.6, though the same optimal relation holds, as expected. When fluctuations are added to the branch angles, the distinguishing feature of zero growth at $\theta^* = \psi$ remains robust as expected. Moreover, G broadens near the maximum. See Figure 2.7. Broadening was also observed in the mean field simulations with noise.

Overlaps: Urban and collaborators use electron tomography to observe many more overlaps than branches in lamellipodia [35]. Their technique allows one to probe the three-dimensional aspect of the cytoskeleton such that filaments that appeared to be branches in two-dimensional electron micrograph images turn out to be overlapping filaments. Based on the prevalence of overlaps, Urban and collaborators proposed a new model for the structuring of lamellipodia [35]. Arp2/3 nucleates new filaments near the membrane (just as dimerization does) such that there is no pre-existing filament and, hence, no memory of its orientation. In other words, there is no branching.

However, we would like to point out that the prevalence of overlaps does not rule out a branched model. In fact, the existence of overlaps is rather natural in a branched model. If each subsequent generation of branches becomes exponen-

tially smaller in length, then there will be no overlaps. This is how one embeds a Bethe lattice—a tree graph—in a plane such that there are no overlaps. See Figure 2.8. If this exponential decrease in length with each generation does not occur, then overlaps are expected. While the original electron micrographs indicate that the filament length increases further back towards the cell body, we do not expect an exponential increase. Therefore, there will be crossings/overlaps between branches. In fact, the overlaps can be reinforced by cross-links thereby increasing the temporary rigidity of the network.

To test this idea, we measure the number of overlaps and compute the ratio, χ , of the number of overlaps to the number of branch points for each particular θ . See Figure 2.9. We see that the ratio peaks where there is optimal growth. Moreover, as the capping rate decreases, the filaments grow longer also allowing for more overlaps. We compare the branched model with a fixed branch angle (plus small fluctuations) to a branched model where the branch angle is uniformly random between 1 and 89 degrees. We do this to disrupt the inheritance in orientation of the fixed branch angle. So, Arp2/3 merely nucleates a filament off a pre-existing filament with no memory of filament orientation. We model the lack of inheritance with the completely random branch angle to capture some aspect of the recently proposed unbranched model.

We observe that the number of overlaps compared to the number of branch points is rather large (exceeding 10) for certain initial filament orientations. Indeed, the notion of many overlaps does not rule out the notion of branching. A decrease in the capping rate increases χ , as expected, since the filaments are typically longer. Moreover, χ rather small for the random branch angle as compared to the fixed branch angle model. The lack of inheritance reduces the number of potential overlaps. The reduction in overlaps should also ring true for a completely non-branched Arp2/3 nucleation model as proposed by Urban and collaborators.

In Figure 2.9, we also plot the overlap for different branch angles. Note that for $\psi = 70^\circ$, χ is approximately the same for those filaments originally oriented at $\theta = 35^\circ$ and for $\theta = 90^\circ$, the subdominant population of filaments.

Filament tip spatial distributions: Finally, using the two-dimensional discrete simulation, we compute the spatial distribution of filament tips. See Figure 2.10. From one filament centered at $x = y = 0$, we observe spreading in the x -direction of the dendritic array by several microns. While there is not much difference between the different branch angles, for the random branch angle model, the broadening in the x -direction is enhanced. However, that broadening is not supported by a large number of overlaps making the network more susceptible to buckling. As for the y -direction, the smaller branch angle allows for more forward growth, as expected, however, the overlap ratio is also smaller. For the random branch angle, the growth in the y -direction is the largest, but, again, there is not much structural support via overlaps.

Combining the overlap data with the distribution of x -data we observe that the system is spreading out in the x -direction as well as overlapping. The spreading allows for the construction of focal adhesions with which the cells temporarily adhere to the surface. The overlaps enhance structural support. Both features are simultaneously possible in a branched model via the dendritic nucleation model. In the absence of the branches, the system cross-links, albeit not as effectively as a branched model, but does not spread out in the x -direction. Moreover, the proliferation of branches (G), from a material standpoint, results in the effective strengthening of the material as the meshwork size, the distance between overlaps, decreases with an increasing number of branches. If one were to suspend disassembledly of the network, this gradation can be modeled via a spatially varying elastic modulus. More specifically, if one were to model the quasi-two-dimensional lamellipodia as a thin elastic plate with a spatially varying elastic modulus, then (1)

the buckling instability softens in that the system does not undergo discontinuous mode changes and (2) the system becomes more robust against out-of-plane buckling as the elastic modulus increases along the direction of axial compression [59]. Therefore, branching accounts for spreading, reinforcements via overlaps, and gradation. Only reinforcement is possible in a nonbranching model for a fixed Arp2/3 concentration.

2.3 Conclusion to chapter 2

Invoking a geometric notion for collision-based branching between globular Arp2/3 and linear, actin filaments, we constructed a mean field model for the orientation of actin filaments near the leading edge of a crawling cell. To study the model, we applied the approach of Maly and Borisy [22], who constructed and studied an initial mean field model with a different physical basis than ours. The Maly and Borisy approach [22] invoked a population biology framework with branching corresponding to birth and capping corresponding to death. More specifically, they used the Fisherian criterion [32, 31] for maximal reproduction as an optimization condition on the filament orientation. Similar to Maly and Borisy [22], we found consistency with previous measurements of the distribution of filament orientation with respect to the leading edge. In particular, the two, well-defined peaks in the distribution at $\theta^* = \pm 35^\circ = \pm \psi/2$ coincide with the optimal relation, assuming $\psi = 70^\circ$. The fact that both our kinetic model and Maly/Borisy model [22] obtain the same optimal relation despite the differing kinetic assumptions, even in the presence of noise, is interesting and calls for further differentiation.

Our Arp2/3-actin collision-based model predicts a subdominant population of filaments that may account for recent measurements on the distribution of filament orientation, which are in apparent contradiction with the earlier measure-

ments [54]. The more recent experiment reported a more broad distribution in filament orientation than previously measured. Moreover, the subdominant population of filaments may be invoked to more accurately model the filament density along the leading edge. Earlier modelling of the filament density demonstrated that larger filament densities in the center required smaller filament densities on the sides of lamellipodia [9, 33]. This requirement is not so consistent with observation, however. By extending the earlier filament density model to include the subdominant population of filaments, this requirement has been relaxed such that the revised filament density model results are more consistent with observations of “excess” filament density at the sides of the leading edge.

To go beyond mean field and study both the positional and orientational degrees of freedom of the actin network in its initial growth phase, we implemented a two-dimensional, kinetic simulation. The mean field optimization condition persists in the two-dimensional simulation, at least for small fluctuations in the branch angle. It would be interesting to extend our collision-based two-dimensional model to include debranching, depolymerization and severing so that we can analyze the approach to steady state and compare our results to the autocatalytic model developed by Carlsson [57], which was recently verified experimentally [58].

Very recent observations of lamellipodia in motile cells via electron tomography reported many more overlaps between filaments than previously estimated using two-dimensional electron micrograph images [35]. Urban and collaborators [35] used this observation to dispute the dendritic nucleation model and propose a new model of unbranched filament nucleation for lamellipodia construction. However, our measurements of the ratio of overlaps to branch points are of order 10 using a branched model. For a branched model to have no overlaps, the filament lengths must be exponentially decreasing in length with each generation, i.e. the planar embedding of a Bethe lattice in two-dimensions. The rather large ratio of

overlaps to branch points actually supports the dendritic nucleation model with its inherited branch angle. The inheritance increases the potential for overlaps and the pairing of filaments. In fact, the pairing observation was also used by Urban and collaborators [35] as a mark against the dendritic nucleation model. We must also point out that branching also promotes spreading of the network to more readily assemble focal adhesions, and gradation to make the network less susceptible to out-of-plane buckling.

There exists other evidence for an unbranched model for lamellipodia reconstruction promoting cell motility. Based on experimental observation, Briehner and collaborators [60] proposed an initial branching motility phase followed by a bundled-actin motility phase, facilitated by fascin or other cross-linking proteins. The notion of a filopodia-dominated phase of motility cannot be ruled out and may be one of many phases of cell motility. However, reconstituted experiments with Arp2/3-actin-fascin demonstrated that Arp2/3 is excluded from the bundling regions [61]. Recent modeling supports this notion [62]. Unfortunately, Urban and collaborators [35] were unable to determine the spatial location of the Arp2/3 in their experiments. We must also point out that the proposal of unbranched Arp2/3 nucleation implies that the filament density along the leading edge depends purely on the Arp2/3 and not on the pre-existing filament density. If the concentration of Arp2/3 is reasonably uniform along the leading edge, then the filament density profile will also be reasonably uniform near the center of the leading edge. Some such profiles were observed in “rough” crawling cells [33].

Finally, while we have addressed the optimization between the filament orientation and the branch angle, we have not addressed the optimization of the branch angle itself. Why does $\psi \approx 70^\circ$? From the results of this work, only when $\psi > 60^\circ$ is the redundant second optimum removed, thus paving the way for a suboptimal orientation whose center axis is not $\theta = 0^\circ$. These off-axis populations allow for

further spreading and overlapping. We also observe that the ratio of overlaps to branch points is approximately the same for the optimized orientation of $\theta = \pm 35^\circ$ as well as $\theta = \pm 90^\circ$ so that there is an elastic similarity between the two types of orientations. Other speculations as to why $\psi \approx 70^\circ$ may be rooted in structural optimization and the like.

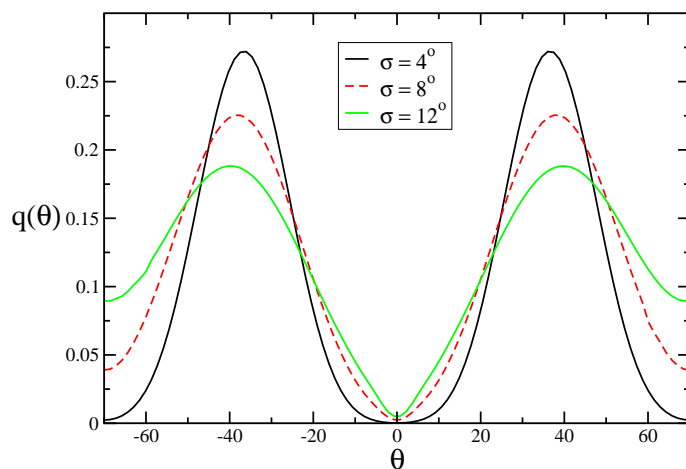


Figure 2.3: Plot of $q(\theta)$ for $\psi = 70^\circ$. For $\sigma = 4^\circ$, $\frac{c'}{b'} = 0.269$, for $\sigma = 8^\circ$, $\frac{c'}{b'} = 0.254$, and for $\sigma = 12^\circ$, $\frac{c'}{b'} = 0.213$.

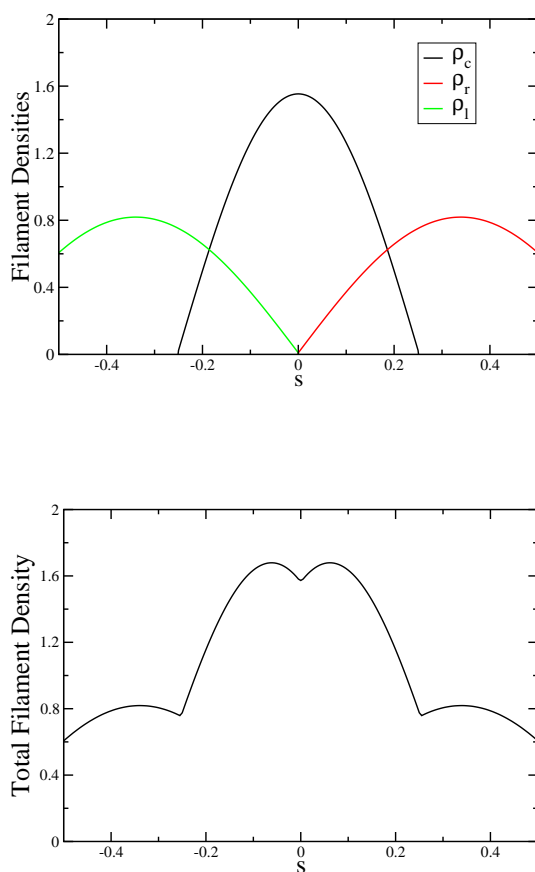


Figure 2.4: Left: Dimensionless filament densities along the leading edge, where $\rho_c = \tilde{\rho}_c^+ + \tilde{\rho}_c^-$, for example. Right: Total dimensionless filament density ($\rho_c + \rho_l + \rho_r$) along leading edge.

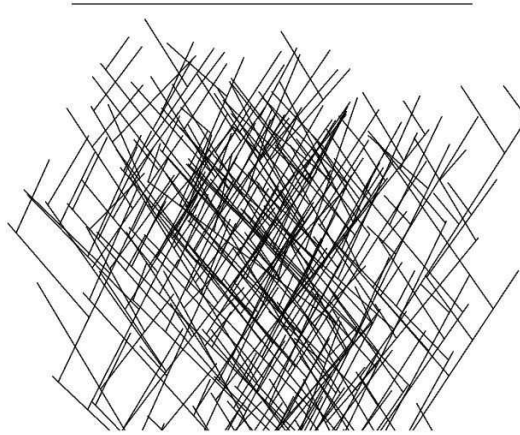


Figure 2.5: Discrete simulation output with $\psi = 70^\circ$, $\theta = 35^\circ$, and $\sigma = 10^\circ$. The length of the horizontal bar is 1 micron.

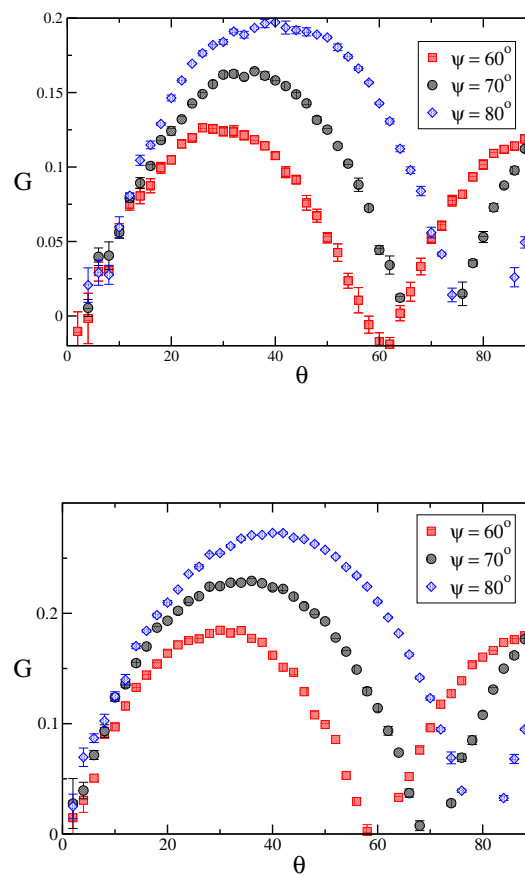


Figure 2.6: Left: Growth rate for different branch angles. Right: Growth rate for $c = 0.67 \text{ s}^{-1}$ (and so more growth than for $c = 0.83 \text{ s}^{-1}$).

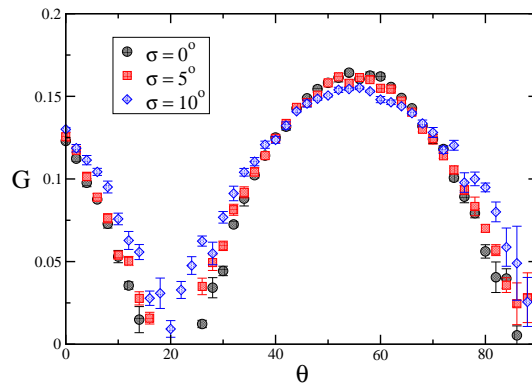


Figure 2.7: Growth rate for 70 degree branching angle with noise.

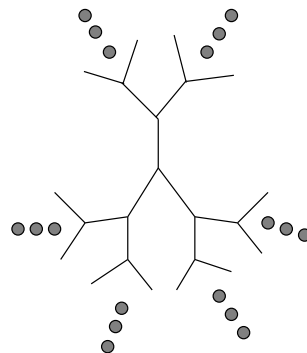


Figure 2.8: Bethe lattice with coordination number three. The circles indicate a repeating pattern.

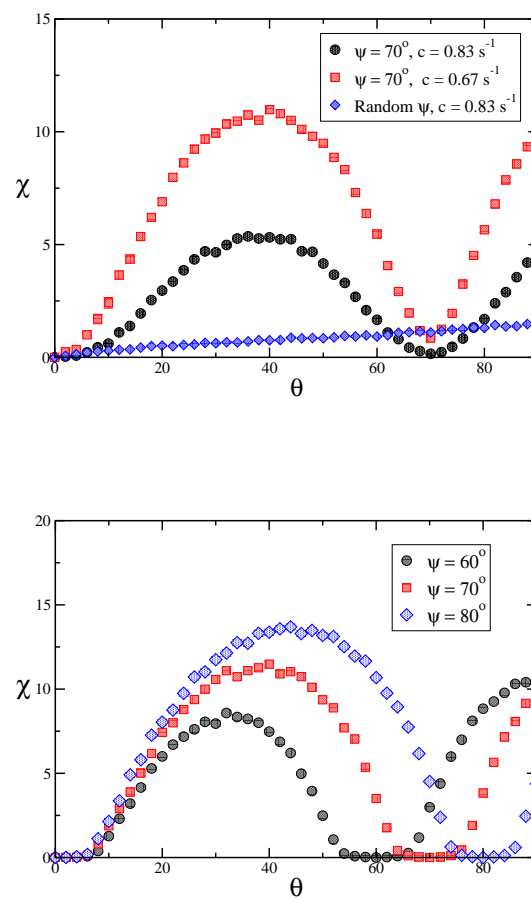


Figure 2.9: Left: The ratio of overlaps to branch points as a function of θ with $\sigma = 10^\circ$ for two fixed branch angle curves. Right: The ratio of overlaps to branch points as a function of θ for a smaller capping rate (more overlaps). Here, $\sigma = 0^\circ$.

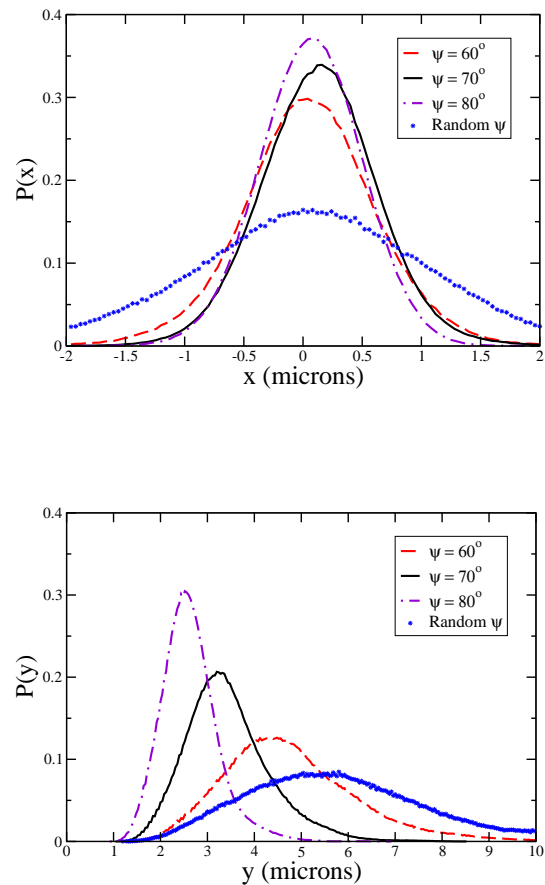


Figure 2.10: Left: Spatial distribution of filament tips in the x -direction (horizontal) for $\psi = 60^\circ, 70^\circ, 80^\circ$ and the random branch model. Right: Spatial distribution of filament tips in the y -direction (vertical) for $\psi = 60^\circ, 70^\circ, 80^\circ$ and the random branch model. For both plots, $\sigma = 10^\circ$.

Chapter 3

Rigidity and Random Networks

In the previous two chapters, I have focused on morphological characteristics of lamellipodia. For instance, based on our kinetic model for the birth and death of F-actin at the leading edge, it was found that the ratio of overlapping filaments to branched filaments can exceed 10, depending on the branching and capping rates and the orientation of filaments with respect to the leading edge. I now ask the questions: How are these filaments crosslinked? What is the mechanics of the branched filaments and the interaction with the mother filament? How does the modeling of the crosslinker affect the overall mechanics of the cytoskeletal network?

Lamellipodia are known to be rich with two types of crosslinkers: α -actinin and filamin A [63]. Experiments on actin filaments crosslinked by α -actinin demonstrate that α -actinin is a very flexible crosslinker allowing for rotations between the two filaments [64]. Filamin A, on the other hand, does not allow for rotations between the two filaments and crosslinks them at a reasonably regular angle [65, 66]. In addition, Arp2/3 plays the dual role of branched filament nucleator and crosslinker between the mother and daughter filaments. Since Arp2/3

“cross-links” the filaments at a regular angle, the Arp2/3 can be considered as another angle-constraining cross-linker in addition to the filamin A.

Given these different types of crosslinkers, freely-rotating and angle-constraining, I would like to investigate the mechanics of model lamellipodia. To establish the background needed to pursue such an investigation, I embark on the presentation of a few topics in the study of the rigidity of random networks, the classic example of which is the random spring network. I use the term “random” since model lamellipodia and the actin cytoskeleton, in general, is a random, or disordered, network of cross-linked filaments as evidenced by the electron micrograph images.

3.1 Constraint counting

Given a set of N points in a space of dimension d , suppose I wanted to form a rigid cluster containing these points by connecting them together in order to form a rigid frame. How many connections would one need to constrain the cluster such that all independent motions of the individual points, each under some given external force, are frozen out? James Clerk Maxwell first answered this question in his famous letter entitled “On the calculation of the equilibrium and stiffness of frames” published in 1864 [67]. In this letter, Maxwell was concerned with calculating the extension of a frame which is a collection of rods/springs connected together. To answer the question above, it is easy to see that one would need exactly the number of constraints as there are *degrees of freedom* in the system. In any dimension, the number of independent degrees of freedom are,

$$\Omega = dN - d(d + 1)/2. \quad (3.1)$$

The first term on the RHS counts the individual degrees of freedom. For two-body interactions dependent only on the distance between the two points, there are, for

example, $2N$ degrees of freedom in 2 dimensions for N points. The second term on the RHS is the number of *rigid body* motions. In 2 dimensions, there are 2 translations and 1 rotation ($2 + 1 = 2 * 3 / 2 = 3$) to arrive at 3. This means for any set of points with no pre-ordained order or topology, in 2 dimensions, the system will be statically determined if $2N - 3$ bonds are connecting the points in that space together.

There is, however, a problem that arises when one considers the following example. Suppose I have a set of 6 points in 2 dimensions, according to the number of degrees of freedom Eq. 3.1 I need $2 * 6 - 3 = 9$ rigid constraints. Imagine that these points are arranged on a square grid (see Fig. 3.1). I now place rigid

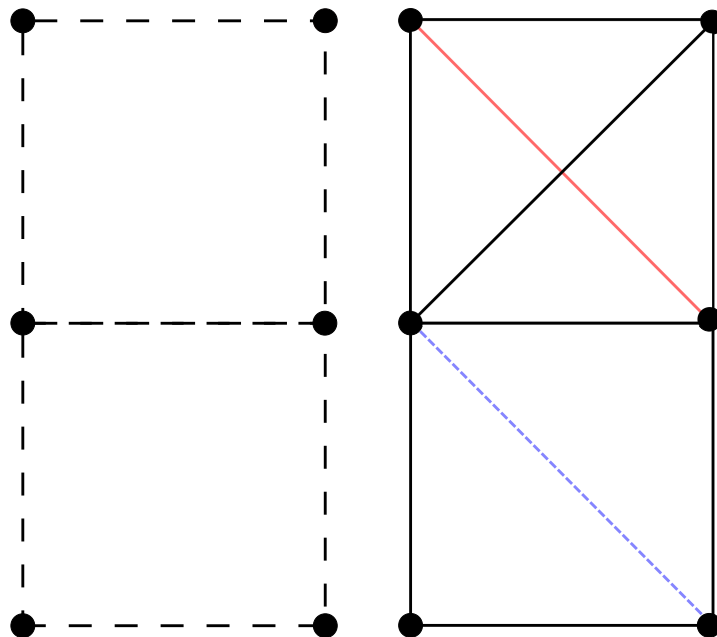


Figure 3.1: (Left) Schematic of the set of unconnected points on a 2 dimensional square grid; (Right) Schematic of one configuration of bonds. The **red** bond is redundant, while the **blue** dashed line is where the red one should be placed if the frame is to be rigid.

constraints (bars) between the nodes (vertices) until I have at most 9 of them. Looking at the bond configuration on the right of Fig. 3.1, it can be seen that the structure will not be stable if the remaining bar is placed along the red line. It will

not be rigid under an infinitesimal shear because the lower box with hinged (freely rotating) vertices is *floppy* under shear. In contrast, when I place the redundant bond along the blue dashed line the network suddenly becomes rigid under any deformation. I then conclude that constraint counting alone will not guarantee stability, because I may have some misplaced *redundant* bonds as in the case when the red bond is occupied. Indeed, the topology of the structure plays some role in the rigidity of these networks.

One remark that should be made for a rigid frame is that the network of bonds connecting the vertices must be geometrically *spanning* or *percolated*. In general, percolation is a phase transition in the connectivity of a system [18]. In these systems one can imagine that placing bonds/bars which are rigid or semi-rigid with some probability p , then ask at what *occupation* probability does the system become connected. To be connected means whether or not the network of disordered bonds spans from one edge of the system in (d dimensions) to the other (this definition can be extended to infinite systems as well). The type of percolation for our example (Fig. 3.1) is also referred to as *scalar* percolation, or *geometric* percolation.

Scalar quantities can be transported through a network that is geometrically percolated or spanning, for example fluid in network of pipes [68]. Typically, the density of bars randomly placed in a network at which the onset of spanning occurs is lower than the density of bars required for the onset of rigidity, another phase transition. The onset of rigidity in random networks can be referred to as rigidity percolation. Since rigidity percolation involves the transmission of forces, or vectors, one can view rigidity percolation as vectorial quantities being transmitted across the network [69]. The transition from not rigid to rigid will be addressed in the next Sec..

The distinction between scalar transmission and vector transmission separates

the two classes of problems, although attempts have been made to suggest the two belong in the same universality class provided the vector problem can be viewed as independent copies of the scalar problem [70]. It has only been shown to be consistent for the Born model in the scalar limit [109, 71].

3.2 Maxwell's floppy modes

In keeping with the idea that a network may be geometrically percolated but not rigid as in Fig. 3.1, how can one characterize the number of floppy modes in the system, i.e. those modes with zero energy cost for finite deformations of the system? It is these modes that will dominate at the onset of rigidity. One possible method is to assign a potential between nodes of the network. This way I could in principle calculate a dynamical matrix and count all of the finite non-zero Eigenfrequencies of the system, which would be the rank of the dynamical matrix. This number represents the number of normal modes in the system and when compared to the number of degrees of freedom would give us the number of floppy modes that characterize how rigid the network is [72]. However, this method would depend on a particular realization of the random network and would be computationally expensive.

The method of Maxwell [67] counting simplifies this calculation (at least for simple systems) greatly. In more complicated systems, it can still provide a good estimate for the number of floppy modes [72]. In practice, one can imagine a system of N vertices in d dimensions as before. Counting the number of independent constraints (N_C) that are imposed on the nodes by either rigid connections or elastic potentials. This number depends on the form of the interaction and the coordination number, z . The coordination number represents the number of connections each node has to its neighbors. The fraction of floppy modes is simply

given by

$$f = \frac{N * d - N_C}{Nd} = 1 - \frac{N_C}{Nd}. \quad (3.2)$$

As an example, I will calculate the number of floppy modes N sites on a triangular lattice (See Fig. 3.2) with only central force interactions.

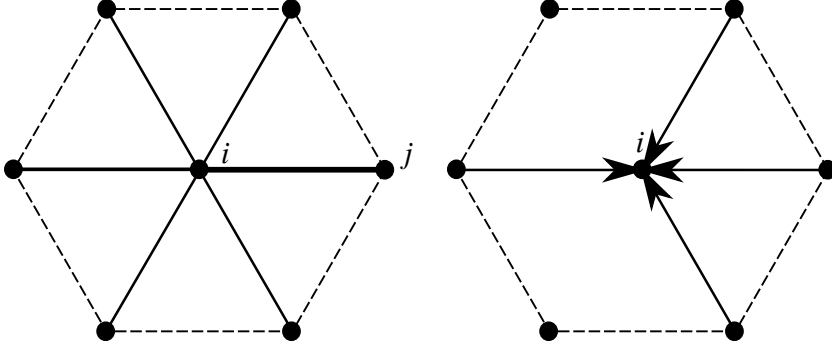


Figure 3.2: (Left) Unit cell of a triangular lattice. Lattice node(site) i has at most 6 nearest neighbors j . (Right) The lattice site i is in static equilibrium when there is at least 4 neighbor connections.

To count the number of independent constraints N_C , I start with a lattice with no bonds or connections between sites. Then place a connection between two sites i and j with a probability p . For the lattice in Fig. 3.2 each site (i) can be connected to at a maximum of 6 neighbors, hence $z_{max} = 6$. However, on average when placing bonds randomly with probability p there will be an average number of bonds $\bar{z} = z * p$. Finally, each pairwise connection is counted twice hence the factor of $1/2$ which gives $N_C = \bar{z}N/2$. The expression for the fraction of floppy modes becomes

$$f = \frac{Nd - \frac{1}{2}Npz}{Nd} = 1 - \frac{pz}{2d}. \quad (3.3)$$

This expression is remarkably simple in that it only depends explicitly on the coordination number z and the dimension of the space. It must be pointed out that every system in d dimensions will have other floppy modes coming from d translations and $d * (d - 1)/2$ rotations [72], which are omitted.

When the fraction of these modes vanishes ($f = 0$) one finds the *critical* occupation probability p_r at which the system exhibits a phase transition from being floppy to being completely rigid. In this example one can solve Eq. 3.4 to arrive at $p_r = 2/3$ with an average coordination number of $\bar{z} = 4$ (See Fig. 3.2.)

Maxwell counting turns out to be quite accurate for this specific case in finding the location of the transition and it can even be extended to cases where bond bending interactions are taken into account such as in the case of the Kirkwood potential [73]. Once the network is rigid, adding more bonds contributes only redundant constraints. These redundant constraints can be quantified by augmenting Eq. 3.4 to incorporate the probability of having a redundancy, $N_r = r(p)$,

$$f = \frac{N * d - \frac{1}{2}Npz}{Nd} + \frac{N_r}{Nd} = 1 - \frac{z}{2d}(p - r(p)) \quad (3.4)$$

Measuring the number of redundancies is equivalent to measuring the number of floppy modes, which implies that the probability of redundancies vanishes for $p < p_r$. In other words, the vanishing of redundancies is dual to the fraction of floppy modes vanishing for $p > p_r$ [74]. For the triangular lattice, when $p = 1$, $r(1) = 1/3$ and, of course, $f(1) = 0$.

3.3 Effective Medium Theory (EMT)

I have shown in the previous Sec. that a lattice of randomly placed bonds will have a finite number of floppy modes (zero-frequency) deformations when the probability of placing bonds on the lattice is less than or equal to the critical value p_r . As the network becomes sufficiently occupied with bonds, there is a macroscopic elastic response of the system. Suppose I wish to calculate the elastic moduli of a disordered network for $p > p_r$. However, the disorder in the system makes it such that the microscopic coupling between sites on the lattice cannot be so

easily related to the macroscopic response of the system as it can for an ordered system. In other words, the mechanical response of the individual nodes may not be easily related to the mechanical stiffness of the bonds that connect them, but may depend on longer range interactions, particularly near a transition [72]. In contrast, for a fully ordered network one can relate the macroscopic response of the network to the microscopic lattice elastic constants.[75].

How does one compute the macroscopic elastic properties of a disordered network? Instead of considering the disordered system explicitly, one can map the network to an effective network where all of the bonds are present and all have the same effective strength. This effective network is just an average (*mean*) of the disorder in the initial system. Since the fluctuations due to disorder are averaged out, one arrives at precisely the mean field scheme one uses to treat other statistical systems such as the Ising ferromagnet [76]. In these systems, in high enough spatial dimensions, it is assumed that spatial heterogeneities are weak such that all gradients of the microscopic order parameter are vanishingly small and that all of the physical phenomena are governed by an average order parameter. One can use the similar concepts implemented in spin systems in these elastic systems where fluctuations due to one “wrong” bond in the system can be computed and averaged over.

Next, I will discuss an example of how one constructs an effective medium theory (EMT) for a disordered network of central force interactions [77, 78, 79]. It must be pointed out that this treatment can be extended to systems with other types of constraints beyond two body interactions [80]. I will address this extension in a later Sec..

3.3.1 Disorder and fluctuations

I begin with the total energy, E , of the system, or

$$E = \frac{\alpha}{2} \sum_{\langle ij \rangle} p_{ij} (\mathbf{u}_{ij} \cdot \mathbf{r}_{ij})^2, \quad (3.5)$$

where \mathbf{u}_{ij} and \mathbf{r}_{ij} is the displacement vector from equilibrium and the lattice unit vector of the bond between sites i and j respectively. Here I assume the small deformation limit of the lattice sites with respect to the unit bond vector defined by \mathbf{r}_{ij} such that transverse motion is neglected [81, 82] (See Appd. B). Thus, to first order the linear springs only depend on the projection of the displacement vector and the undisturbed lattice vector. Finally, the interaction has as an elastic stiffness α .

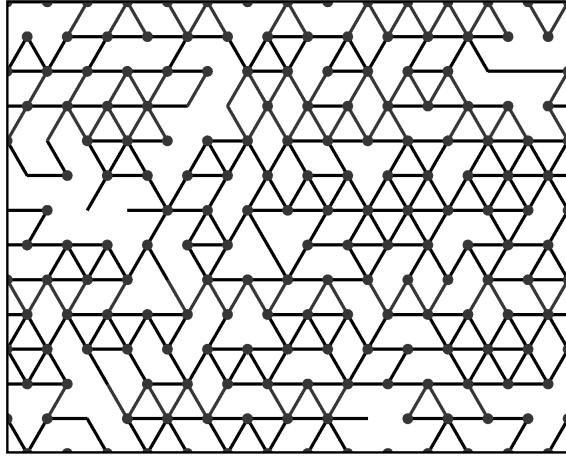


Figure 3.3: A section of a bond diluted triangular lattice with $p > p_r$.

Next, I consider a perfect network of *effective* springs all of spring constant α_m . The effective spring constant represents the amount of disorder in our initial system. I now impose a uniform strain on the network such that all of the springs are uniformly deformed by an amount δu_m . Now replace a bond in the perfect lattice between sites i and j with a spring which has a “different” elastic constant

of α' . Since there is a bond with a different spring constant between sites i and j , the deformation of that bond will have an “extra” displacement compared to the surrounding ones which are assumed to be displaced by an amount δu_m . To “fix” the displacement of the different bond to be at the correct length I impose a second “virtual” force (f) on the bond ij to make it displaced by an amount δu_m . By superposition I can add f to the force (\bar{f}) that is already present due to the initial uniform dilation, or

$$\bar{f} - f = \alpha' \delta u_m. \quad (3.6)$$

By force balance I know that, $\bar{f} = \alpha_m \delta u_m$. I can now determine the virtual force to restore the bond ij to the correct displacement δu_m , which is given by the Eq.,

$$f = (\alpha_m - \alpha') \delta u_m. \quad (3.7)$$

To determine the extra displacement δu when the different bond is between sites i and j I need an Eq. which relates f to δu . To do this I consider the same network in the unstrained state (no uniform dilation) and apply the same force f (equation 3.7) to the bond ij with the different bond α' in place. Again, to relate f to δu , I begin with the perfect lattice where all the bonds have elastic strength α_m (see Fig. 3.4). Since the displacement of the bond ij upon applying f will depend on the surrounding network there will be an effective spring constant

$$\alpha_{eff} = \alpha_m / a^*, \quad (3.8)$$

where $0 < a^* < 1$.

Note: The Origin of a^*

One way to visualize the effective spring constant due to the surrounding network is to consider just part of the unit cell of a triangular lattice (a square with one extra bond along the diagonal figure 3.4).

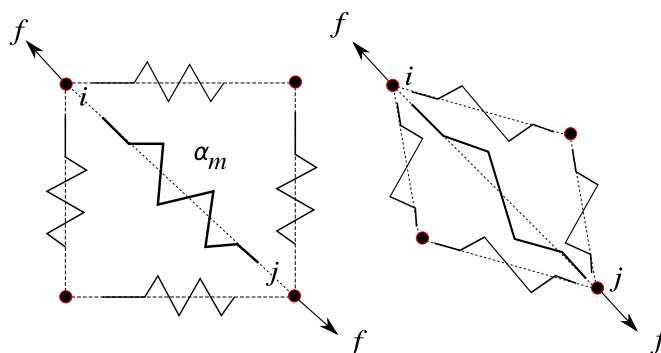


Figure 3.4: To construct a triangular lattice we start with a square lattice and add a diagonal constraint. Shown here is $1/3$ of the triangular unit cell.

Consider pulling on the two corners of the box with a force f . This will stretch the corners (i.e the bond ij) by an amount δu as well as displacing the surrounding springs connecting site i and j . The displacement of the surrounding springs contribute to the elastic stiffness between sites i and j . Hence, I need to consider the various combinations of the parallel and series components in the square cell. The edges have a springs in series and these two are in parallel with the diagonal spring connecting sites i and j . The effective spring constant of the cell is just the addition of 3 parallel components,

$$\alpha_m + \left(\frac{\alpha_m}{2} + \frac{\alpha_m}{2}\right) = 2\alpha_m. \quad (3.9)$$

Comparing the above Eq. with Eq. 3.8 gives $a^* = 1/2$. Although this simple example highlights the concept of an effective spring between neighboring sites i and j , extending this analysis to the entire cell is not as straight forward.

End Note

The effective spring constant between sites i and j will be changed by removing the diagonal spring α_m in between them, such that the effective spring constant becomes,

$$\alpha'_m = \frac{\alpha_m}{a^*} - \alpha_m. \quad (3.10)$$

Now replace the missing spring with one which has a stiffness equal to α' (different bond). This bond will be in parallel with the effective spring network (See Fig. below 3.5) and the relationship between f and δu is

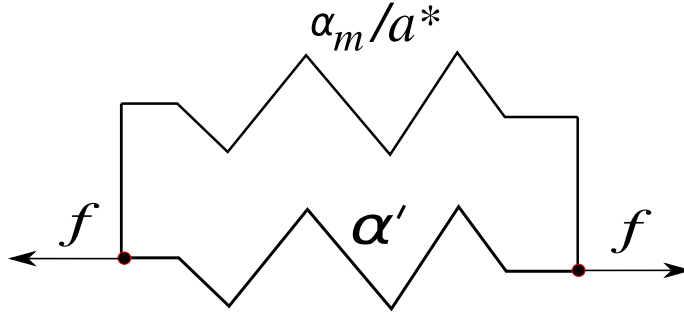


Figure 3.5: The effective spring network after combining all series and parallel sub-networks.

$$f = (\alpha'_m + \alpha')\delta u. \quad (3.11)$$

Equating the above Eq. to Eq. 3.7 and solving for the extra displacement δu yields

$$\delta u = \frac{\delta u_m(\alpha_m - \alpha')}{\left(\frac{\alpha_m}{a^*} - \alpha_m + \alpha'\right)}. \quad (3.12)$$

To compute the effective spring constants in mean field I want the fluctuations caused by the extra displacement δu due to having a different elastic stiffness between the sites i and j to vanish on average. To perform the averaging, the disorder probability distribution is given by

$$P(\alpha) = p\delta(\alpha - \alpha') + (1 - p)\delta(\alpha'). \quad (3.13)$$

Now ensemble average δu over the distribution of spring constants α' and adjust the value of α_m to ensure that the fluctuations in the extra displacement vanishes [77]. In other words, I demand that the macroscopic properties of the perfect effective lattice be identical as the disordered one. Therefore, I can describe our disordered system on average as an effective one with the appropriate effective spring constants α_m . This prescription leads to a constitutive relation for the value of the effective medium spring constant α_m and the amount of bond disorder p , or

$$\frac{\alpha_m}{\alpha} = \frac{(p - a^*)}{1 - a^*}. \quad (3.14)$$

The effective elastic constant vanishes if $p \leq a^*$ but is finite if $p > a^* \equiv p_{iso} = \frac{2d}{z}$, where z is the coordination number and d is the dimension of the space. Therefore, I expect the transition to be second order and the scaling of the shear modulus to be linear near the *isostatic* point $G \sim \alpha(p - p_{iso})$ [77, 79]. The isostatic point refers to the location where a network of central force bodies becomes rigid. In networks which incorporate bending interactions as well as central force interactions, the isostatic point becomes important as a location for another transition, namely the non-affine to affine transition. Nonaffinity and isostaticity are discussed in more detail in Sec. 3.4.4.

Although a simple explanation of a^* was given here, full discussion and calculation from a dynamical matrix approach can be found in Appendix B. I will demonstrate that this method can be extended to other types of interactions such as bond-bending interactions as first simulated by Sahimi [80] and analytically executed by Das [81].

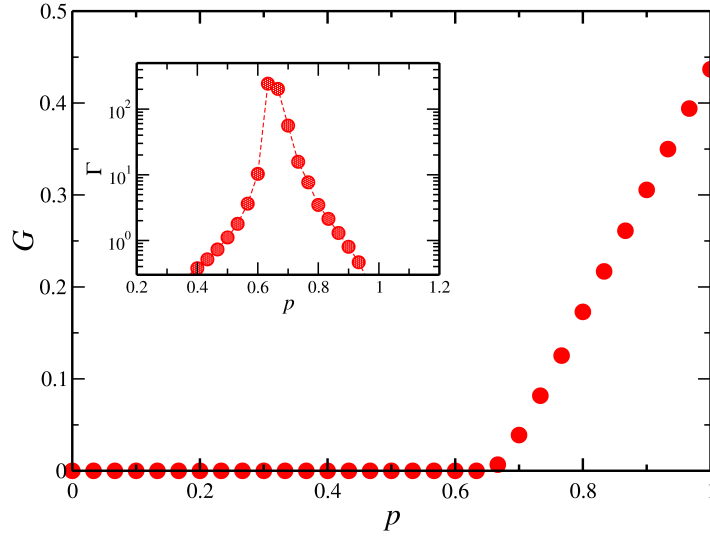


Figure 3.6: Plot of the shear modulus G varying the bond occupation probability p . The transition to a rigid network happens for $p \simeq 2/3$ for this simulation with a system size of $N = 128 \times 128$ lattice sites. Inset shows the nonaffinity of the deformations within the lattice. As p approaches the isostatic point (p_{iso}) the nonaffinity parameter (Γ) diverges which signals the transition from a floppy network to a rigid one (See section 3.4.4 and chapter 4 for details).

3.4 Filament bending networks

Over the last decade and a half, studies of networks of entangled and crosslinked semiflexible biopolymers have been approached experimentally and theoretically [83, 84, 85, 86, 87, 88, 89]. As for the crosslinked systems, some biological crosslinkers are permanent, while most are dynamic in that they bind two filaments over some time scale. Systems with dynamic crosslinkers and entangled solutions are technically viscoelastic. However, despite the transient nature of the entanglements or crosslinks, over intermediate time scales of interest, the system behaves elastically, i.e. as if the entanglements/crosslinks are permanent. It is this regime that I will focus on.

Typical *in vitro* concentrations for entangled solutions of F-actin having a macroscopic elastic response range between $36 \mu\text{g/ml}$ to 2mg/ml . At this con-

centration, the average distance between filaments that cross is about $0.3 \mu m$ [83]. In these studies, it was found that the macroscopic properties of these networks can be almost entirely explained by the micromechanics of the constituents of the network, namely the semiflexible biopolymers [83, 85, 86, 87, 90, 91, 92]. Therefore, I will review some of the mechanics of individual semiflexible polymers.

3.4.1 The semiflexible chain

Semiflexible polymers are different from their fully flexible counterparts in that they have an inherent bending stiffness allowing them to stay fairly straight even when exposed to a thermal bath at room temperature. Their mechanics is controlled by this bending in much the same way a rod or cylinder is when subjected to an external load. I can quantify this by writing a Hamiltonian with a term proportional to the local tangent vector describing the deviation from a completely straight conformation [93].

$$\mathcal{H} = \frac{\kappa}{2} \int ds \left(\frac{\partial^2 \vec{r}(s)}{\partial s^2} \right)^2 \quad (3.15)$$

For a chain of length l , $\vec{r}(s)$ is the position along the chain as a function of the chains contour length s (see Fig. 3.7). The bending stiffness can be related to the intrinsic mechanical properties of the chain which is given as $\kappa = EI$, where E is the Young's modulus and I is the moment of inertia of a cross-section of the chain if I assume it to be approximately solid [11].

When a filament chain is under tension as it would be in a strained crosslinked or entangled network, it will resist this tension because it prefers to be undulated due to the thermal fluctuations. The length scale on which these fluctuations persist when there is no tension is given by the persistence length of the chain l_p . This length is defined by the tangent-tangent correlation function, where $\vec{t}(s) \equiv$

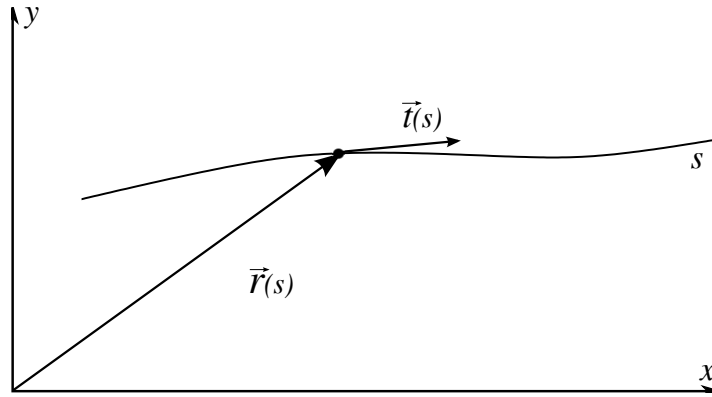


Figure 3.7: Schematic of the position vector $\vec{r}(s)$ along a section of a semiflexible chain as a function of the chain's contour coordinate s . Also shown the unit tangent vector $\vec{t}(s)$.

$\frac{\partial \vec{r}(s)}{\partial s}$, or

$$\langle \vec{t}(s) \cdot \vec{t}(0) \rangle \simeq e^{-s/l_p}. \quad (3.16)$$

I have now introduced the two main length scales in this system, the contour length of the chain l and the persistence length l_p . In two-dimensions, $l_p = \frac{\kappa}{k_B T}$. Single chain mechanics will depend entirely on these two length scales. The typical persistence length of actin is $\sim 17 \mu m$. The average length of actin in the cytoskeleton can be on the order of 100 nm to $1 \mu m$, so fluctuations will be quite small and one can justify the so-called *weak bending* limit $l \ll l_p$. Please see Appendix C for details [11].

3.4.2 Force-extension of a semiflexible chain

Consider a force f acting on a stiff chain of length l at some temperature T . Since the force that is applied will be “pulling” out the thermal fluctuations of the chain, the coupling to f must come from the local tangent field of the chain characterizing the *crumpledness* in the chain. I write the Hamiltonian for the

chain under tension as,

$$\mathcal{H} = \frac{1}{2} \int ds \left[\kappa \left(\frac{\partial^2 \vec{r}(s)}{\partial s^2} \right)^2 + f \left(\frac{\partial \vec{r}(s)}{\partial s} \right) \right]. \quad (3.17)$$

The first term in the integrand is the energy contribution due to bending the chain and the second term is energy contribution due to the coupling with the external force f . It is the work done on the chain. For $l < l_p$, then the chain is almost straight with some deviation from its central axis denoted by x . Therefore, $\vec{r} \approx [u(x), v(x)]$ with $s \approx x$ and $u(x)$ and $v(x)$ are the two independent transverse directions to the central axis [11, 92].

Fourier transforming both terms in the Hamiltonian for one transverse direction, I arrive at a sum over all fluctuating modes of the chain,

$$FT[\mathcal{H}] = \frac{l}{4} \sum_q (\kappa q^4 + f q^2) u_q^2. \quad (3.18)$$

The expectation value for the q^{th} fluctuation in this Boltzmann ensemble is

$$\langle u_q^2 \rangle = \frac{4k_B T}{l(\kappa q^4 + f q^2)} \quad (3.19)$$

This gives the contraction of the chain under a tension f as (see Appendix C)

$$\langle \Delta l \rangle = k_B T \sum_q \frac{1}{\kappa q^2 + f}. \quad (3.20)$$

The extension of the chain can now be determined as a function of pulling force f , which is just the difference between the projected length in the presence of the tension and in the absence of the tension, i.e. $\delta l = \langle \Delta l \rangle_f - \langle \Delta l \rangle_0$. At small

forces, the force-extension relation is linear, or

$$\delta l = \frac{l^4}{90l_p\kappa} f. \quad (3.21)$$

This relation provides us with an estimate of the effective linear response of the chain and the effective stiffness of the chain,

$$\alpha = \frac{90l_p\kappa}{l^4}. \quad (3.22)$$

At larger forces, the force-extension relation becomes nonlinear and ultimately the force diverges with the inverse square of the distance from full extension.

The above linear force-extension relation has been used to estimate the elastic moduli for entangled semiflexible polymer solutions at small strains (in the elastic regime). The linear relation is merely modified by a simple factor of the number of chains in a plane parallel to the shear and the length of the polymer is replaced with its length between entanglements [83]. For densely crosslinked networks, the entanglement length is the mesh size of the network. For less dense networks, the above single chain Hamiltonian is invoked to estimate the probability of one chain intersecting transversely with another chain. The scaling predictions from such an analysis has been verified in experimentally [83, 84].

3.4.3 EMT for semiflexible chains

A network composed of semiflexible filaments when placed under external stress will respond in accordance with the mechanics which governs the individual filament chains. As pointed out in the previous Sec., the mechanics of semiflexible chains is governed by two length scales. The first is the physical length (contour length) of the polymer chain, l , and second length scale is the resistance to thermal undulations of the chain, l_p , the persistence length. This length scale is governed

by its diameter and its Young's modulus, E . When considering random networks of semiflexible filaments there emerges one more natural length scale—the distance between crossings of neighboring chains, i.e. entanglements/crosslinks, l_c . Entanglements prohibit filaments from passing through one another but can allow for chains to translate with respect to one another on long timescales. This behavior leads to a rich viscoelastic response of networks of filaments. In contrast, permanent crosslinks (with which I deal with from now on) prohibit filaments from sliding with respect to one another but allow for free rotations. These networks also form a diverse response under an imposed external strain which is due to the type of crosslinker and the mechanics of the semiflexible polymers.

These three length scales, l , l_p , and l_c , allow for a wide range of behaviors in the mechanical response of these networks [90, 91, 94, 85, 86]. Here, I focus on studying the behavior of these networks as described by a disordered two-dimensional lattice. In this treatment, the distance between crosslinks in the network is much smaller than the persistence length and the filaments are treated as stiff rods [81]. As in Sec. 3.3.1, I will construct an effective medium theory to study the macroscopic elastic network properties. In previous theoretical treatments of stiff fiber networks, it was found that they can behave differently depending on the concentration of filaments in the network [85, 86]. For dense networks with many crosslinks, the primary modes of deformation are mostly affine, or stretch dominated deformations which probe the inherent stretching stiffness of the filaments, which was discussed in the previous Sec. 3.4.1 and quantified in Eq. 3.22. In contrast, when networks are dilute and the distance between filament crossing is large, nonaffine deformations are preferred in the network and energy is primarily stored in the bending of filaments [81, 82]. It should also be pointed out that even networks of central force (purely stretching) interactions exhibit strong nonaffine deformations near the isostatic point, or the onset of rigidity. Nonaffine defor-

mations in either case signal where the rigidity transition is taking place. Even for networks with bending and stretching interactions there is a bend to stretch crossover near the isostatic point where nonaffine deformation play a significant role in the transition [81, 82].

To construct the EMT, I start with a similar discretized version of the energy given in Eq. 3.17,

$$E = \frac{\alpha}{2} \sum_{\langle ij \rangle} p_{ij} (\mathbf{u}_{ij} \cdot \mathbf{r}_{ij})^2 + \frac{\kappa}{2} \sum_{\langle ij \widehat{h} = \pi \rangle} p_{ij} p_{jk} ((\mathbf{u}_{ji} + \mathbf{u}_{jk}) \times \mathbf{r}_{ji})^2 \quad (3.23)$$

The first term on the RHS is the stretching energy of the filaments, which is motivated by the linear force-extension relation and the elastic stiffness α representing the contribution of thermal fluctuations to the linear response of the filaments under tension. The second term on the RHS is the energy which comes from the bending of filaments and is represented here as a three-body interaction where there exists a penalty for collinear bonds on the lattice to bend with respect to one another. To introduce filaments of a finite length on the network, I populate the lattice with bonds at probability p . In the sums over bonds ij , $p_{ij} = 1$ if a bond is occupied between sites ij or 0 if its not. For bond-bending there is a three-body interaction so two bonds need to be present in order for the interaction to contribute to the total energy (See Fig. 3.8). It has been pointed out in other models that bending should be treated an effective single bond percolation process, but this type of argument fails to predict the correct rigidity threshold [82].

Given the energetics above, I can now calculate the effective spring contributions when considering the same arguments given in Sec. 3.3.1 for just linear hookean springs. One must now pay attention to deformations which couple to

bending modes and those that couple to stretching modes. However, for small lattice site displacements these modes will be decoupled, so I can treat deformations parallel to a bonds and deformations perpendicular to bonds independently [78, 81]. This property also ensures that the dynamical matrices are decoupled and the effective springs constants in the ordered lattice are

$$\begin{aligned}\alpha_m &= \frac{\alpha}{a^*} \\ \kappa_m &= \frac{\kappa}{b^*}.\end{aligned}\tag{3.24}$$

Here, a^* and b^* can be found independently in terms of the dynamical matrix $\mathbf{D}(s)$. Please see Appendix B for calculation details.

$$\begin{aligned}a^* &= \frac{d}{Nz} \sum_{\mathbf{k}} [\mathbf{D}_s(\mathbf{k})\mathbf{D}^{-1}(\mathbf{k})] \\ b^* &= \frac{d}{Nz} \sum_{\mathbf{k}} [\mathbf{D}_b(\mathbf{k})\mathbf{D}^{-1}(\mathbf{k})]\end{aligned}\tag{3.25}$$

where $\mathbf{D}(\mathbf{k}) = \mathbf{D}_s(\mathbf{k}) + \mathbf{D}_b(\mathbf{k})$ and s and b refer to stretching and bending respectively. Despite the fact that I have added a new type on interaction on the triangular lattice, there still are the same number of independent degrees of freedom that need to be constrained. As shown in Appendix B in Sec. B.2, $a^* + b^*$ is equal to a quantity which purely depends on the ratio between the dimension of the space ($2 * d$) and coordination number (z) of the lattice site (Eq. B.21). Therefore, it is expected that

$$a^* + b^* = \frac{2d}{z}.\tag{3.26}$$

Finally, using the appropriate double bond disorder distribution, the effective

medium constants are given by

$$\begin{aligned} \frac{\alpha_m}{\alpha} &= \frac{p - a^*}{1 - a^*} \\ \frac{\kappa_m}{\kappa} &= \frac{p^2 - b^*}{1 - b^*}. \end{aligned} \quad (3.27)$$

Two things are apparent from the structure of the above Eq.s. First, the effective lattice elastic constants are decoupled. This is reasonable because I am assuming that the deformations in the lattice are small and, hence, decoupled. Second, κ_m depends on the square of the bond occupation probability since filament bending is a three-body interaction and, therefore, involves three lattice sites, or two bonds.

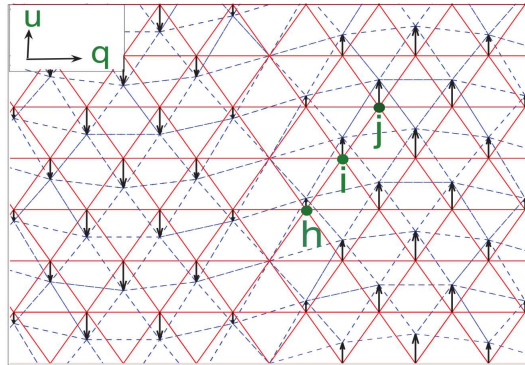


Figure 3.8: Bending interactions on the lattice involve three sites ijh . Bending is defined as the angle between the bonds \overline{ij} and \overline{ih} . In the undeformed (red) lattice the equilibrium configuration is when bond \overline{ij} and \overline{ih} are parallel. The deformed (blue) lattice is depicting a \mathbf{q} dependent strain \mathbf{u} . [Phys. Rev. Lett. Vol. 99, 038101 (2007)]

When the bond occupation is below a certain threshold p_r , the rigidity transition, the effective elastic lattice constants vanish. When $p = p_r$ is right at the onset of rigidity and $a^* = p_r$ and $b^* = p_r^2$. Plugging these values into Eq. 3.26 the

threshold for the onset of rigidity becomes

$$p_r^2 + p_r = \frac{2}{3} \rightarrow p_r = 0.457. \quad (3.28)$$

This threshold is lower than that of a network of just linear hookean springs (See Fig. 3.6 and Eq. B.21). This result is to be expected since there is an increase in the number of constraints in our system due to three-body interactions.

3.4.4 Nonaffinity

Under external strain, one can expect a mechanical response when the network is beyond the rigidity transition as discussed early in Sec. 3.3.1. In a disordered network how do the individual deformations of the bonds in the lattice contribute to the macroscopic response of the network? Do the lattice sites deform in accordance with the external strain deformation, or do they deform in some non-trivial manner? The answer is that it depends on the concentration of filaments (and to some extent the applied deformation field) in the network. For low concentration networks when bond bending interactions are present, under a general externally applied strain, the individual filaments will tend to prefer bending deformations. This is not surprising since I have put this behavior directly into the model. What is surprising is that bending deformations are also preferred when the network is under a simple shear strain. Simple shear is a linear or *affine* transformation on the network in that it only involves a rotation and stretch/compression of the sites or bonds in the network. In contrast, bending deformations are not at all affine since it is a higher order effect, hence nonaffine deformations.

Theoretical studies have suggested [85, 86, 95] that nonaffine deformations will

appear in dilute systems of filaments and the shear modulus will scale as [11]

$$G_{NA} = \frac{\kappa}{\xi^4} \sim c^4 \quad (3.29)$$

where κ is the bending stiffness, ξ is the mean distance between crosslinks, and c is the filament concentration. Lattice simulations of bond networks where bond bending interactions are present suggest that numerically the shear modulus will scale as the bending stiffness $G \sim \kappa$ where the mean distance between crosslinks is the lattice spacing of the network which is unity.

It has also been recently pointed out in the literature [82] that models where the bending stiffness is vanishing small, a divergence of the nonaffine deformations signals a crossover from purely-bending dominated to purely-stretching dominated regimes as the bond occupation probability is increase through the isostatic point *p_{iso}*. Again, the isostatic point is where a purely central force network becomes rigid. In addition, purely central force networks also exhibit highly nonaffine deformations right at the onset of rigidity (See Fig 3.6).

The connection between nonaffine deformations and the macroscopic elastic properties are still poorly understood and recent simulations of off/on lattice bending models exploring this relationship have just begun to understand this connection. This topic will be explored in chapter four of this thesis.

3.5 Conclusion to chapter 3

Starting from a very general concept of constraint counting, I asked whether a set of rigid rods when connected together in some fashion produces a frame that is rigid to perturbations. This allows one to characterize such systems by looking

at the number of *floppy* modes or zero-frequency modes the system possesses. This quantity turns out to actually measure the fraction of free degrees of freedom that have yet to be constrained (see Eq. 3.4). In central-force networks, the number of degrees of freedom grows as the number of particles (nodes) times the dimension of the space that the network is embedded in. When the number of floppy modes vanishes one can identify a point where the network becomes rigid, called the *rigidity percolation transition*. The bond occupation probability at the rigidity transition (p_r) can be related to two physical properties of the network 1) the dimension of the space and 2) the coordination of the underlying lattice.

To gauge the macroscopic response of a disordered network, one can map the disorder to a perfect lattice with effective lattice elastic constants using *effective medium theory*. The theory allows one to calculate the effective elastic lattice constants as a function of the microscopic disorder. This is accomplished by relating the effect of deleting a single bond and replacing with a bond with a different spring constant and then calculating the effect that virtual forces have on neighboring sites where the bond was replaced. The dynamical matrix of the perfect network characterizes the effect that sites where bonds were deleted “feel” from their neighbors in the unit cell.

Using the EMT framework one can model crosslinked networks of semiflexible polymers, such as the actin cytoskeleton. One has to incorporate the mechanics of semiflexible polymers by introducing a bending term between lattice bonds. Furthermore, bond stretching can be interpreted as linear response of a semiflexible chain when entropic fluctuations are pulled out under tension. When these two effects are added to the lattice, the rigidity percolation transition point moves down to a lower value than for just linear central force springs. This implies that disordered networks of filaments are more dilute than those with just central force networks. This effect arises purely from the addition of longer range interactions

like that of bending. Studying cytoskeletal networks can also be done by simulating the disordered networks (see chapter 4). Simulations provide a more deeper probe to study the micromechanics of the lattice directly as opposed to mean field theories where all spatial information is absent.

In conclusion, the framework for studying disordered networks meshes nicely with studying disordered biomaterials such as the actin cytoskeleton. I will explore this more in chapter 4 where the addition of different types of crosslinking agents is addressed and how they can effect the overall mechanics of the cytoskeleton. This new analysis provides insight into why there exists multiple types of crosslinkers in the actin cytoskeleton, an example of which is the lamellipodium.

Chapter 4

Redundancy and Cooperativity-Mechanics of Cross-linked Filamentous Networks

The mechanical response of most cells arises from the mechanics of its cytoskeleton, a polymeric scaffold that spans the interior of these cells, and its interaction with the extra-cellular environment. The cytoskeleton is made up of complex assemblies of protein filaments cross-linked and bundled together by a variety of accessory proteins. For example, there are approximately 23 distinct classes of accessory proteins such as fascin, α -actinin, and filamin A [63] that cross-link filamentous-actin (F-actin), a major component of the cytoskeleton that is responsible for the mechanical integrity and motility of cells. Given the multitude of cross-linkers, several natural questions arise: Are the different types

of cross-linkers redundant, or do they each serve specific functions? Do they act independently or cooperatively? What are the consequences of their mechanics for the mechanical integrity and response of the cell? What optimization principles are at play in determining the mechanical integrity and response of the cell?

A mutation study of *dictyostelium discoideum* cells lacking a particular actin cross-linking can still grow, locomote, and develop, though with some defects, thereby suggesting at least partial redundancy in the cross-linker's mechanical function [96]. On the other hand, two types of cross-linkers working cooperatively may produce enhanced mechanical response. This cooperativity has been demonstrated in stress fibers cross-linked with the actin binding proteins (ABP) α -actinin and fascin, where stress fibers containing both α -actinin and fascin were more mechanically stable than stress fibers containing only α -actinin or fascin [97]. In addition, it has been found that two different cross-linkers are required for actin bundle formation *in vivo* [98]. It could also be the case that different cross-linkers work independently of one another such that the dominant cross-linker dictates the mechanical response of the network [99]. Given these various possibilities, how the cell uses different cross-linking proteins to optimize for certain mechanical characteristics is an important open issue in cytoskeletal mechanics.

Here, we address this redundancy versus cooperativity issue by studying a model network of semiflexible filaments cross-linked with two types of cross-linkers. We first study the mechanical properties of the model network with one type of cross-linker and then add the second type of cross-linker and look for mechanical similarities and differences with the original model network. In addition, we also address the redundancy versus cooperativity issue of two types of cross-linkers for networks made of flexible filaments.

As for the two types of cross-linkers, we consider cross-linkers that allow the crossing filaments to rotate freely (freely-rotating cross-links) and cross-linkers

that constrain the angle between two filaments. The ABP α -actinin is a candidate for the former type of cross-linking mechanics: optical trapping studies demonstrate that two filaments bound by α -actinin can rotate easily [64]. As an example of the latter, we consider filamin A (FLNa), which binds two actin filaments at a reasonably regular angle of ninety degrees, suggesting that FLNa constrains the angular degrees of freedom between two filaments [65, 66]. Here, we do not take into account the possible unfolding of FLNa since the energy to unfold filamin A is large [65, 100, 84], nor do we take into account the kinetics of FLNa since we seek to understand fully the mechanics in the static regime first. There exist other possible examples of angle-constraining cross-linkers such as Arp2/3 that serves a dual role as an F-actin nucleator and a cross-linker [20]. While its role as a nucleator has been emphasized in lamellipodia formation [101, 15], its role constraining the angle between the mother and daughter filaments is presumably also important for lamellipodia mechanics. Better understanding of the mechanical role of Arp2/3 in lamellipodia may also help to distinguish between the dendritic nucleation model for lamellipodia formation and a new model where Arp2/3 only nucleates new filaments but does not produce branches [35].

In studying the mechanical properties of compositely cross-linked filamentous networks, we focus on the onset of mechanical rigidity as the filament concentration is increased above some critical threshold. This onset is otherwise known as rigidity percolation [70, 79, 77, 78, 102, 80, 88, 89]. Above this critical threshold, both experiments and theoretical studies of F-actin networks have observed distinct mechanical regimes. For dense, stiff networks the mechanical response is uniform or affine and the strain energy is stored predominantly in filament stretching modes. While for sparse, floppy networks one finds a non-affine response dominated by filament bending where the observed mechanical response of the network is inhomogeneous and highly sensitive to the lengthscale being

probed [85, 86, 87, 103, 95, 90, 91, 81]. It has been recently reported that there exists a *bend-stretch* coupled regime for intermediate crosslinking densities and filament stiffnesses [82].

While considerable progress has been made in understanding the mechanics of cytoskeletal networks that are cross-linked by one type of cross-linker, compositely cross-linked networks are only beginning to be explored experimentally [99, 104] as are composite filament networks with one type of cross-linker theoretically [105, 106].

Here we investigate the mechanics of such networks as a function of the concentration and elasticity of the cross-linkers and the filaments.

4.1 Model and methods

We arrange infinitely long filaments in the plane of a two-dimensional triangular lattice. The filaments are given an extensional spring constant α , and a filament bending modulus κ . We introduce finite filament length L into the system by cutting bonds with probability $1 - p$, where $0 < p < 1$, with no spatial correlations between these cutting points. The cutting generates a disordered network with a broad distribution of filament lengths. When two filaments intersect, there exists a freely-rotating cross-link preventing the two filaments from sliding with respect to one another. Next, we introduce angular springs with strength κ_{nc} between filaments crossing at 60° angles with a probability p_{nc} , where *nc* denotes non-collinear. These angular springs model the second type of cross-linker. See Fig.4.1 for a schematic.

We study the mechanical response of this disordered network under an externally applied strain in the linear response regime. For simplicity we set the rest length of the bonds to unity. Let \mathbf{r}_{ij} be the unit vector along bonds and

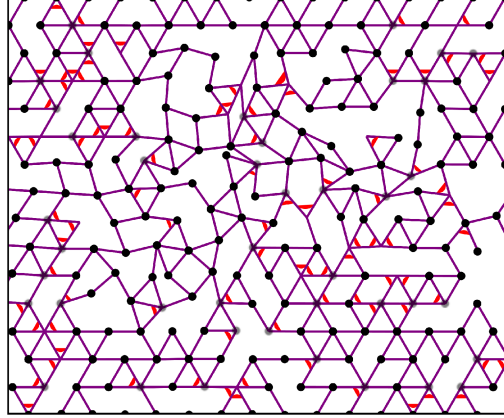


Figure 4.1: Deformed configuration a compositely cross-linked semiflexible network with 2.7 percent strain, with bond occupation probability $p = 0.64$, and angle-constraining cross-linker occupation probability $p_{nc} = 0.15$. The purple lines denote semiflexible filaments, the red arcs denote angle-constraining cross-links, the black circles represent nodes where all crossing filaments are free to rotate, while the grey circles denote nodes where some of the crossing filaments are free to rotate. The filament bending stiffness relative to stretching stiffness $\kappa/\alpha = 10^{-6}$ and the stiffness of angular cross-links relative to stretching stiffness $\kappa_{nc}/\alpha = 10^{-6}$.

$\mathbf{u}_{ij} = \mathbf{u}_i - \mathbf{u}_j$ the strain on the bond ij . For small deformation u , the deformation energy is

$$\begin{aligned}
 E = & \frac{\alpha}{2} \sum_{\langle ij \rangle} p_{ij} (\mathbf{u}_{ij} \cdot \mathbf{r}_{ij})^2 + \frac{\kappa}{2} \sum_{\langle ijk=\pi \rangle} p_{ij} p_{jk} ((\mathbf{u}_{ji} + \mathbf{u}_{jk}) \times \mathbf{r}_{ji})^2 \\
 & + \frac{\kappa_{nc}}{2} \sum_{\langle ijk=\pi/3 \rangle} p_{ij} p_{jk} p_{nc} \Delta\theta_{ijk}^2
 \end{aligned} \tag{4.1}$$

where p_{ij} is the probability that a bond is occupied, $\sum_{\langle ij \rangle}$ represents sum over all bonds and $\sum_{\langle ijk \rangle}$ represents sum over pairs of bonds sharing a node. The first term in the deformation energy corresponds to the cost of extension or compression of the bonds, the second term to the penalty for the bending of filament segments made of pairs of adjacent collinear bonds, and the last term to the energy cost of change in the angles between crossing filaments that meet at 60° angle. Fur-

thermore, for small deformations $\Delta\theta_{ijk} = (\mathbf{u}_{ji} \times \mathbf{r}_{ji} - \mathbf{u}_{jk} \times \mathbf{r}_{jk}) \cdot (\mathbf{r}_{ji} \times \mathbf{r}_{jk}) = -\frac{(\mathbf{u}_{ji} \cdot \mathbf{r}_{ji} + \mathbf{u}_{jk} \cdot \mathbf{r}_{jk})}{2} + u_{ik} \cdot \mathbf{r}_{ik}$. It is straightforward to see that the angular spring \widehat{ijk} between ij and jk will contribute to an effective spring in parallel with ik , giving rise to an enhanced effective spring constant $\mu = \alpha + \frac{3}{2}\kappa_{nc}$.

4.1.1 EMT - Collinear and non-collinear bending

We study the effective medium mechanical response for such disordered networks following the mean field theory developed in [77, 78] for central force networks and [81] for filament bending networks. The aim of the theory is to construct an effective medium, or ordered network, that has the same mechanical response to a given deformation field as the depleted network under consideration. The effective elastic constants are determined by requiring that strain fluctuations produced in the original, ordered network by randomly cutting filaments and removing angular springs vanish when averaged over the entire network.

Let us consider an ordered network with each bond having a spring constant μ_m , a filament bending constant for adjacent collinear bond pairs κ_m , and an angular bending constant $\kappa_{nc,m}$ between bonds making 60° angles. Under small applied strain, the filament stretching and filament bending modes are orthogonal, with stretching forces contributing only to deformations along filaments (\mathbf{u}_{\parallel}) and bending forces contributing only to deformations perpendicular to filaments (\mathbf{u}_{\perp}), and hence we can treat them separately. The angular forces due to the angular (non-collinear) springs, when present, contribute to stretching of filaments as discussed earlier, where we only consider three body interactions. For these springs to contribute to bending one needs to consider four-body interactions which is outside the scope of this paper and will be addressed in future work.

We start with the deformed network and replace a pair of adjacent collinear bonds with bending rigidity κ_m by one with a rigidity κ , and a bond spring with

extensional elastic constant μ_m by a spring with an elastic constant μ and the facing 60° angular spring by κ_{nc} . This will lead to additional deformation of the above filament segments and the angle which we calculate as follows. The virtual force that needs to be applied to restore the nodes to their original positions before the replacement of the bonds will have a stretching, a bending and an angular contribution: F_s , F_b , and F_θ . The virtual stretching force is given by $F_s = (\mu_m - \alpha - 3\kappa_{nc}/2)u_{\parallel,m}$, the virtual filament bending force is $F_b = (\kappa_m - \kappa)u_{\perp,m}$, while the virtual force to restore the angle is $F_\theta = (\kappa_{nc,m} - \kappa_{nc})\theta_m$, where $u_{\parallel,m}$, $u_{\perp,m}$ and θ_m are the corresponding deformations in the ordered network under the applied deformation field. By the superposition principle, the strain fluctuations introduced by replacing the above bending hinges and bonds in the strained network are the same as the extra deformations that result when we apply the above virtual forces on respective hinges and segments in the unstrained network. The components of this ‘‘fluctuation’’ are, therefore, given by:

$$\begin{aligned} d\ell_{\parallel} &= \frac{F_s}{\mu_m/a^* - \mu_m + \alpha + (3/2)\kappa_{nc}} \\ d\ell_{\perp} &= \frac{F_b}{\kappa_m/b^* - \kappa_m + \kappa} \\ d\theta &= \frac{F_\theta}{\kappa_{nc,m}/c^* - \kappa_{nc,m} + \kappa_{nc}} \end{aligned} \quad (4.2)$$

The effective medium spring and bending constants, μ_m , κ_m and $\kappa_{nc,m}$, respectively, can be calculated by demanding that the disordered-averaged deformations $\langle d\ell_{\parallel} \rangle$, $\langle d\ell_{\perp} \rangle$, and $\langle d\theta \rangle$ vanish, i.e. $\left\langle \frac{\mu_m - \alpha - 3\kappa_{nc}/2}{\mu_m/a^* - \mu_m + \alpha + 3\kappa_{nc}/2} \right\rangle = 0$, $\left\langle \frac{\kappa_m - \kappa}{\kappa_m/b^* - \kappa_m + \kappa} \right\rangle = 0$, and $\left\langle \frac{\kappa_{nc,m} - \kappa_{nc}}{\kappa_{nc,m}/c^* - \kappa_{nc,m} + \kappa_{nc}} \right\rangle = 0$. To perform the disorder averaging, since the stretching of filaments is defined in terms of spring elasticity of single bonds α , the disorder in filament stretching is given by $P(\alpha') = p\delta(\alpha' - \alpha) + (1 - p)\delta(\alpha')$. Filament bending, however, is defined on pairs of adjacent collinear bonds with

the normalized probability distribution $P(\kappa') = p^2\delta(\kappa' - \kappa) + (1 - p^2)\delta(\kappa')$. Similarly, for the angular springs, the normalized probability distribution is given by $P(\kappa'_{nc}) = p_{nc}p^2\delta(\kappa'_{nc} - \kappa_{nc}) + (1 - p_{nc}p^2)\delta(\kappa'_{nc})$. This disorder averaging gives the effective medium elastic constants as a function of p and p_{nc} as

$$\begin{aligned}
& p^3 p_{arp} \left(\frac{\mu_m - \alpha - 3\kappa_{arp}/2}{\mu_m/a^* - \mu_m + \alpha + 3\kappa_{arp}/2} \right) + (1 - p)p^2 p_{arp} \left(\frac{\mu_m - 3\kappa_{arp}/2}{\mu_m/a^* - \mu_m + 3\kappa_{arp}/2} \right) \\
& + p(1 - p^2 p_{arp}) \left(\frac{\mu_m - \alpha}{\mu_m/a^* - \mu_m + \alpha} \right) + (1 - p)(1 - p^2 p_{arp}) \left(\frac{\mu_m}{\mu_m/a^* - \mu_m} \right) = 0 \\
& \frac{\kappa_m}{\kappa} = \frac{p^2 - b^*}{1 - b^*}, \quad \text{and} \quad \frac{\kappa_{m,arp}}{\kappa_{arp}} = \frac{p_{arp} p^2 - c^*}{1 - c^*}. \tag{4.3}
\end{aligned}$$

The constants a^* , b^* and c^* for the network contribution to the effective spring constant μ_m/a^* of bonds, to the filament bending rigidity κ_m/b^* , and the bending rigidity κ_{nc}/c^* of angular springs making 60° angles respectively, are given by $a^*, b^*, c^* = \frac{2}{Nz} \sum_q Tr [\mathbf{D}_{s,b,nc}(q) \mathbf{D}^{-1}(q)]$. The sum is over the first Brillouin zone and z is the coordination number. The stretching, filament bending and non-collinear bending contributions, $\mathbf{D}_{s,b,nc}(q)$ respectively, to the full dynamical matrix $\mathbf{D}(q) = \mathbf{D}_s(q) + \mathbf{D}_b(q) + \mathbf{D}_{nc}(q)$, are given by:

$$\begin{aligned}
\mathbf{D}_s(q) &= \mu_m \sum_{\langle ij \rangle} [1 - e^{-i\mathbf{q} \cdot \mathbf{r}_{ij}}] \mathbf{r}_{ij} \mathbf{r}_{ij} \\
\mathbf{D}_b(q) &= \kappa_m \sum_{\langle ij \rangle} [4(1 - \cos(\mathbf{q} \cdot \mathbf{r}_{ij})) \\
&\quad - (1 - \cos(2\mathbf{q} \cdot \mathbf{r}_{ij}))] (\mathbf{I} - \mathbf{r}_{ij} \mathbf{r}_{ij}) \\
\mathbf{D}_{nc}(q) &= \frac{3}{2} \kappa_{nc,m} \sum [2(1 - \cos(\mathbf{q} \cdot \mathbf{r}_{ij})) + 2(1 - \cos(\mathbf{q} \cdot \mathbf{r}_{ik})) \\
&\quad - 2(1 - \cos(\mathbf{q} \cdot \mathbf{r}_{jk}))] \mathbf{r}_{ij} \mathbf{r}_{ik} \tag{4.4}
\end{aligned}$$

with \mathbf{I} the unit tensor and the sums are over nearest neighbors [77]. Note that for small q , $\mathbf{D}_b \sim q^4$ and $\mathbf{D}_s \sim q^2$ have the expected wavenumber dependencies for bending and stretching.

By definition, $a^* + b^* + c^* = 2d/z$, where $d = 2$ is the dimensionality of the system. At the rigidity percolation threshold $p = p_{rp}$, μ_m , κ_m and $\kappa_{nc,m}$ vanish, giving $a^* = p + p^2 p_{nc} - p^3 p_{nc}$, $b^* = p^2$ and $c^* = p^2 p_{nc}$. For semiflexible filament networks with only freely-rotating crosslinks i.e. filament stretching and bending interactions only, the rigidity percolation threshold is given by $p_{rp} = 0.457$. For networks with angle-constraining crosslinks, at $p_{nc} = 1$, we obtain rigidity percolation thresholds $p_{rp} = 0.405$ for the case of flexible filament networks, and $p_{rp} = 0.347$ for semiflexible filament networks. We also calculate how p_{rp} changes on continuously increasing p_{nc} from 0 to 1.

4.1.2 Numerical simulations

Simulations were carried out on a triangular lattice with half periodic boundary conditions along the shear direction for the energetic terms whose small deformation limit is given in Eq. (4.1). Networks were constructed by adding bonds between lattice sites with probability p . Next, a shear deformation was applied to the two fixed boundaries of magnitude $\pm\gamma$. The lattice was then relaxed by minimizing its energy using the conjugate gradient method [107] allowing the deformation to propagate into the bulk of the lattice. Once the minimized energetic state was found within the tolerance specified, in this case the square root of the machine precision $\sim 10^{-8}$, the shear modulus was then measured using the relation, $G = \frac{2E_{min}}{a_{cell}(\gamma L)^2}$, using small strains $< 5\%$, with L denoting the system length and a_{cell} denoting the area of the unit cell for a triangular lattice which is equal to $3\sqrt{3}$ in our units. System size $L = 64$ was studied, unless otherwise specified, and sufficient averaging was performed.

4.2 Results

4.2.1 Mechanical integrity as measured by the shear modulus

On a triangular lattice, networks made solely of Hookean springs lose rigidity at a bond occupation probability around $p_{rp,I} = 2/3$ [67, 108, 77]. This result corresponds to the central force isostatic point at which the number of constraints is equal to the number of degrees of freedom on average. In contrast, networks made of semiflexible filaments become rigid at a smaller p due to extra constraints placed on the system via filament bending. For semiflexible networks with freely-rotating crosslinks, our effective medium theory shows that the shear modulus, G , approaches zero at $p_{rp} = 0.457$ as shown in Fig.4.2 (a). This result is in good agreement with our simulation results yielding $p_{rp} = 0.442(6)$ and previous numerical results [82]. See Fig.4.2 (d). A different formulation of the EMT yields $p_{rp} \approx 0.56$ [82]. By introducing additional crosslinks that constrain angles between filaments at 60° , the rigidity percolation threshold is lowered. Our EMT yields $p_{rp} = 0.347$ and our simulations yield $p_{pr} = 0.348(4)$ for $p_{nc} = 1$ (Fig.4.2 (c) and (f)). The cooperative mechanical interplay between these crosslinks and their interaction with filaments allows the network to form a rigid stress-bearing structure at remarkably low crosslinking densities, almost immediately after it attains geometric percolation, $p_c = 2 \sin(\pi/18)$, which agrees with a calculation by Kantor and Webman [109]. For flexible filament networks, introducing angle-constraining crosslinkers also lowers the rigidity percolation threshold as compared to the isostatic point with the network attaining rigidity at $p_{rp} = 0.405$ for our EMT and $p_{rp} = 0.408(4)$ in the simulations ((Fig.4.2 (b) and (e)). Incidentally, our result agrees very well with a previous simulation [110]. We also compute analytically and numerically how p_{rp} changes with p_{nc} . See Fig.4.3(a), (b) and (c).

Note that p_{rp} is lowered continuously as the concentration of angle-constraining crosslinks is increased.

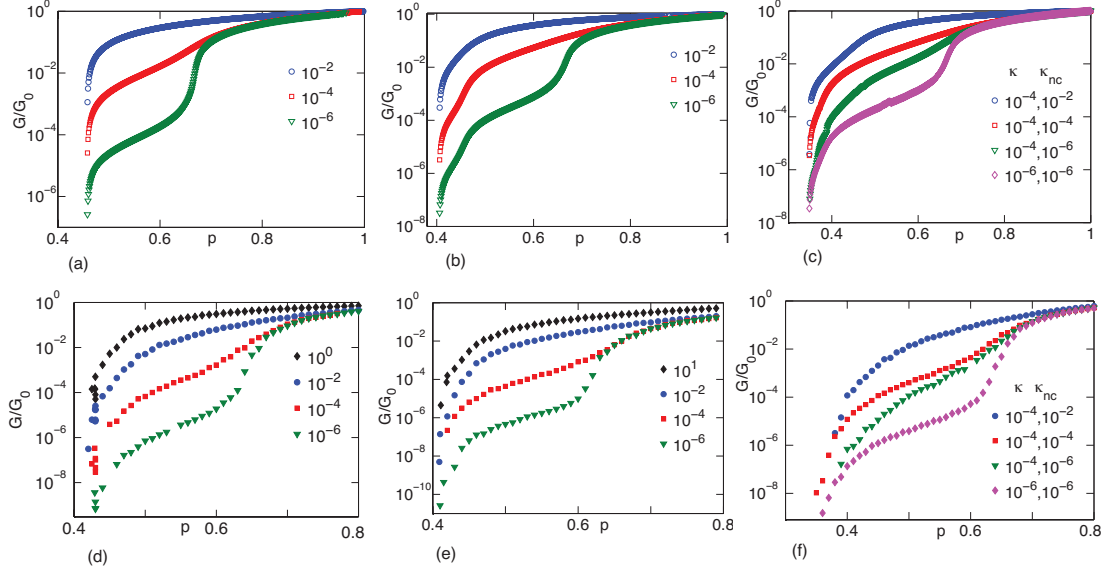


Figure 4.2: The shear modulus as a function of p for semiflexible networks with freely-rotating crosslinks ((a) and (d)), flexible networks with freely-rotating and angle-constraining crosslinks ((b) and (e)), and semiflexible networks with both crosslinkers ((c) and (f)). The top panels show results from the effective medium theory and bottom panels show results from the simulations.

Just above the rigidity percolation threshold, for a semiflexible network with freely-rotating crosslinks, we find a bending-dominated regime for sparse networks with the shear modulus eventually crossing over to a stretch dominated affine regime at higher filament densities. The purely stretch dominated regime is represented by the macroscopic shear modulus G staying almost constant with increasing p , while in the purely bend dominated regime the network is highly floppy and G is a sensitive function of p , decreasing rapidly as p is lowered. This behavior has been observed previously in [85, 86, 87, 103, 95, 81, 82]. For $\kappa \ll \alpha$, both the effective medium theory and the simulations yield a bend-stretch coupled regime, which is characterized by an inflection in G as a function of p as observed most clearly for $\kappa = 10^{-6}$ (with $\alpha = 1$).

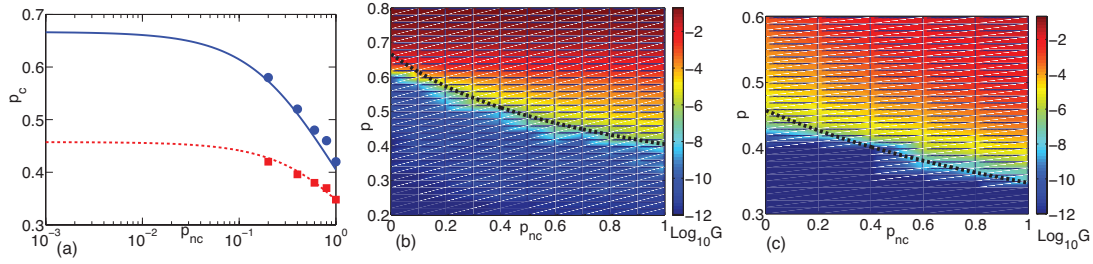


Figure 4.3: The presence of angular constraints allows these networks to have a finite rigidity even for small concentration of filaments. Figure (a) shows how the rigidity percolation threshold can be continuously lowered by increasing the concentration of angular springs for flexible (solid, blue) and stiff (dashed, red) networks. The lines correspond to the effective medium theory and the symbols to the numerical simulation. Figures (b) and (c) show the shear modulus (in logarithmic scale described by the colorbar) as a function of p and p_{nc} for flexible networks (b) and semiflexible networks (c). The parameter values studied are (b) $\kappa_{nc}/\alpha = 10^{-4}$ and (c) $\kappa/\alpha = 10^{-4}$, $\kappa_{nc}/\alpha = 10^{-2}$. The black dashed lines in (b) and (c) correspond to the effective medium theory prediction of the rigidity percolation threshold. For the flexible networks $L = 32$ while for semiflexible networks $L = 64$.

We find a similar non-affine to affine crossover for the compositely crosslinked flexible filament networks and semiflexible filament networks as p is increased. For the flexible filament networks, however, the bend-stretch coupling regime occurs for $\kappa_{nc} \ll \alpha$, i.e. κ_{nc} replaces κ . For semiflexible filament networks, as long as $\kappa_{nc} \lesssim \kappa \ll \alpha$, the bend-stretch coupled regime is robust (for fixed p_{nc}). In contrast, for $\kappa \ll \kappa_{nc} \ll \alpha$, the angle-constraining crosslinker suppresses the bend-stretch coupled regime and enhances the shear modulus to that of an affinely deforming network (for fixed p_{nc}). The mechanics of the network has been altered with the introduction of the second type of crosslinker.

4.2.2 Non-affinity parameter

To further investigate how the interaction of the crosslinkers affects the affine and non-affine mechanical regimes, we numerically study a measure for the degree of

non-affinity in the mechanical response, Γ , defined in Ref.[82] as:

$$\Gamma = \frac{1}{L^2} \gamma^2 \sum_i^N (\mathbf{u}_i - \mathbf{u}_{aff})^2. \quad (4.5)$$

The non-affinity parameter can be interpreted as a measure of the proximity to criticality, diverging at a critical point as we approach infinite system size. We find that Γ develops a peak at the rigidity percolation threshold, which progressively moves to smaller values of p as the concentration of angular crosslinkers p_{nc} is increased (Fig.4.4 (a)). A second peak develops near the isostatic point for $\kappa_{nc} \lesssim \kappa \ll \alpha$ as seen in Fig.4.4 (b). As both the collinear and non-collinear bending stiffnesses tend to zero, the network mechanics approaches that of a central force network, and the second peak in Γ at the isostatic point becomes increasingly more pronounced.

On the other hand, this second peak can be suppressed by increasing κ_{nc}/κ (Fig.4.4 (b)), or by increasing the concentration p_{nc} (Fig.4.4 (a)) even for very small values of κ/α . This further corroborates that adding angle-constraining crosslinkers to non-affine networks can suppress non-affine fluctuations, provided they energetically dominate over filament bending. The reason for this suppression can be understood by considering the effect of adding a constraint which prohibits the free rotation of crossing filaments. As the concentration of these non-collinear crosslinks p_{nc} is increased (at fixed avg. filament length) microscopic deformations will become correlated. The lengthscale associated with this correlation will increase on increasing either p or p_{nc} , and will eventually reach a lengthscale comparable to system size even at $p \sim p_{rp,I}$ at large enough concentration and/or stiffness of the angular springs. As a result the mechanical response of the network will approach that of an affinely deforming network. Upon decreasing the value of κ_{nc}/α relative to κ/α we again recover the second peak because energetically the

system can afford to bend collectively near the isostatic point.

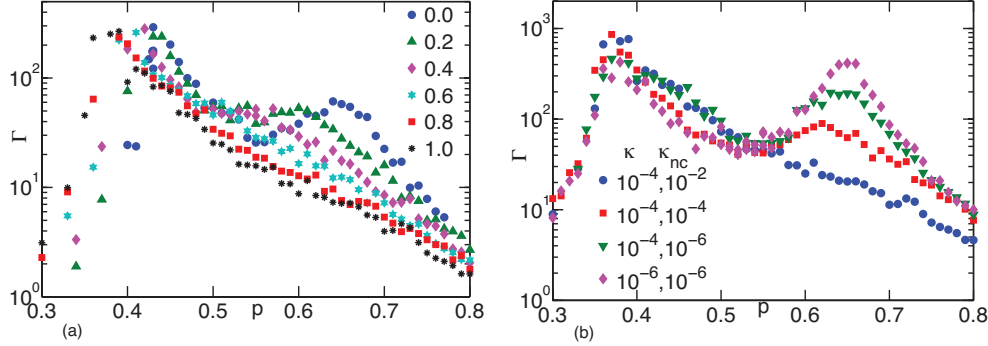


Figure 4.4: The non-affinity parameter Γ as a function of p for semiflexible networks with both types of crosslinkers. In (a) we show the effect of changing the concentration p_{nc} of the angle-constraining crosslinkers for $\kappa/\alpha = 10^{-4}$, $\kappa_{nc}/\alpha = 10^{-2}$, while in (b) we show the effect of changing their stiffness κ_{nc} .

4.2.3 Scaling near the isostatic point

Finally, using scaling analysis we quantify the similarity in mechanics between freely-rotating crosslinked semiflexible networks and compositely crosslinked flexible networks. To do this, we examine the scaling of the shear modulus G near the isostatic point with $\Delta p = p - p_{rp,I} \ll 1$. For $\kappa/\alpha \ll \Delta p$ (or $\kappa_{nc}/\alpha \ll \Delta p$), the shear modulus scales as $G = \alpha |\Delta p|^f \mathcal{G}_{\pm}(\frac{\kappa}{\alpha} |\Delta p|^{-\phi})$ (or $G = \alpha |\Delta p|^f \mathcal{G}_{\pm}(\frac{\kappa_{nc}}{\alpha} |\Delta p|^{-\phi})$) [82, 111]. For both (a) $\kappa = 0, \kappa_{nc} > 0$ and (b) $\kappa > 0, \kappa_{nc} = 0$, the EMT predicts $f = 1$ and $\phi = 2$ as shown in Fig.4.2.3(a) and (b), indicating that both types of networks demonstrate redundant, or generic, mechanics. To compare the EMT results with the simulations, we use the position in the second peak in Γ to determine the central force percolation threshold, $p_{rp,I}$, and then vary f and ϕ to obtain the best scaling collapse. For case (a), $p_{rp,I} = 0.666(3)$, $f = 1.1(1)$ and $\phi = 2.8(1)$. For case (b), $p_{rp,I} = 0.659(5)$, $f = 1.1(1)$ and $\phi = 2.9(1)$. Both sets of exponents are reasonably consistent with those found in Ref. [82] for a semiflexible network with freely-rotating crosslinks only. Preliminary simulations

for compositely crosslinked semiflexible networks indicate that the shear modulus scales as $G = \alpha|\Delta p|^f \mathcal{G}_\pm(\frac{\kappa}{\alpha}|\Delta p|^{-\phi}, \frac{\kappa_{nc}}{\alpha}|\Delta p|^{-\gamma})$ also with a similar f and a similar ϕ with $\phi = \gamma$.

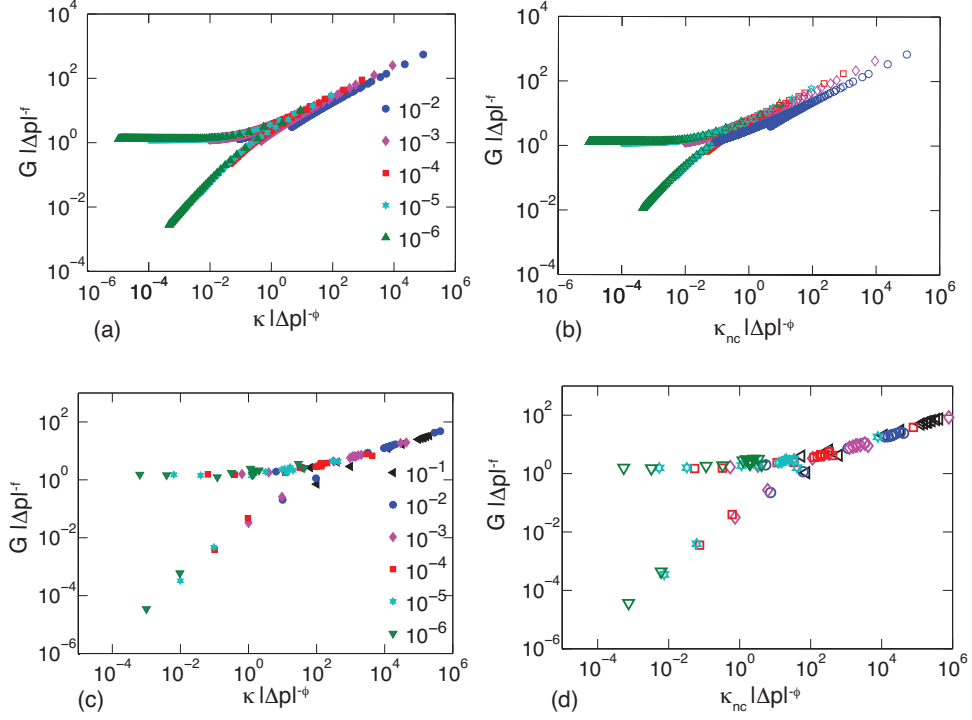


Figure 4.5: Close to isostaticity, the shear modulus G scales with $\Delta p = p - p_{rp,I}$ and κ (κ_{nc}) as $G|\Delta p|^{-f} = \kappa|\Delta p|^{-\phi}$. The effective medium theory predicts mean field exponents $f = 1$ and $\phi = 2$ for both semiflexible networks with freely-rotating crosslinkers (a) and compositely crosslinked flexible networks (b), while simulations predict $f = 1.1(1)$ and $\phi = 2.9(1)$ for semiflexible networks with freely-rotating crosslinkers (c) and $f = 1.1(1)$ and $\phi = 2.8(1)$ for compositely crosslinked flexible networks (d).

4.3 Conclusion to chapter 4

In the limit of small strain, we conclude that the presence of multiple crosslinkers in living cells can be simultaneously cooperative and redundant in response to mechanical cues, with important implications for cell mechanics. Redundant functionality helps the cytoskeleton be robust to a wide range of mechanical cues. On

the other hand, different crosslinkers can also act cooperatively allowing the system to vary the critical filament concentration above which the cytoskeleton can transmit mechanical forces. This may enable the cytoskeleton to easily remodel in response to mechanical cues via the binding/unbinding of crosslinkers (tuning concentration) or their folding/unfolding (tuning stiffness and type of crosslinker). Since the cytoskeleton consists of a finite amount of material, the ability to alter mechanics without introducing major morphological changes or motifs may play important role in processes such as cell motility and shape change.

4.3.1 Crosslinker mechanics: Cooperativity

In our study of two types of crosslinkers, crosslinkers that allow free rotations of filaments and crosslinkers that do not, we find two types of cooperative effects in the mechanics of such compositely crosslinked networks. The first cooperative effect depends on the relative concentration of the two types of crosslinkers and second depends on the relative stiffness of the angle-constraining crosslinkers to the bending stiffness of the individual filaments. The first cooperative effect can be most strikingly observed beginning with an actin/ α -actinin network and increasing the concentration of FLNa, with α -actinin representing the freely-rotating crosslinker [64] and FLNa representing the angle-constraining crosslinker [65]. By tuning the concentration of FLNa, the cell can modulate the minimum concentration of actin filaments necessary to attain mechanical rigidity, which can be essentially as low as the filament concentration required to form a geometrically percolating structure. This is in good agreement with the experimental observation that FLNa creates an F-actin network at filament concentrations lower than any other known crosslinker [65]. When the onset of mechanical rigidity is very close to the geometric percolation threshold, the system is optimizing for rigidity with the least amount of material. Such an optimization principle is reasonable

given the finite amount of scaffolding material in the cell. Increasing the FLNa concentration also suppresses the non-affine fluctuations near the rigidity percolation threshold by increasing the shear modulus of the network and giving rise to a more affine mechanical response while keeping the filament concentration fixed. Moreover, the cooperativity of α -actinin and FLNa working to enhance the mechanical stiffness of actin networks has recently been observed in experiments [104]. The addition of angle-constraining crosslinkers to flexible filament networks also decreases the concentration threshold required for mechanical rigidity, though the lower bound on the threshold is not as close as to geometric percolation as it is for semiflexible filaments. The lowering of the rigidity percolation threshold is independent of the energy scale of the crosslinker. It depends purely on the number of degrees of freedom the crosslinker can freeze out between two filaments, i.e. the structure of the crosslinker.

The second cooperative interplay between the two crosslinkers depends on the energy scale of the angle-constraining crosslinker to the filament bending energy. For $\kappa \ll \alpha$, the freely-rotating semiflexible filament system exhibits large non-affine fluctuations near the isostatic point. Upon addition of the angle-constraining crosslinkers, for $\kappa_{nc} \geq \kappa$, the non-affine fluctuations near this point become suppressed and the mechanics of the angle-constraining crosslinker dominates the system. Once again, with a small change in concentration of the second crosslinker, the mechanical response of the network is changed dramatically.

4.3.2 Crosslinker mechanics: Redundancy

We observe two redundant effects in these compositely crosslinked networks, the first of which depends on energy scales. For $\kappa_{nc} \ll \kappa$ with $\kappa \ll \alpha$, the non-affine fluctuations near the isostatic point in the freely-rotating crosslinker semiflexible filament network remain large even with the addition of the angle-constraining

crosslinker. In other words, the angle-constraining crosslinkers are redundant near the isostatic point. Their purpose is to decrease the amount of material needed for mechanical rigidity as opposed to alter mechanical properties at higher filament concentrations.

Redundancy is also evident in the mechanics of these networks sharing some important, generic properties. All three networks studied here (free-rotating crosslinked semibflexible networks and compositely crosslinked semiflexible and flexible networks) have three distinct mechanical regimes: a regime dominated by the stretching elasticity of filaments, a regime dominated by the bending elasticity of filaments and/or stiffness of angle-constraining crosslinkers, and an intermediate regime which depends on the interplay between these interactions. The extent of these regimes can be controlled by tuning the relative strength of the above mechanical interactions. In particular, the ratio of bending rigidity to extensional modulus of an individual actin filament is $\sim 10^{-3}$ [85, 86, 87]. Since the bend-stretch coupled regime has not been observed in prior experiments on *in-vitro* actin networks crosslinked with FLNa only, we conjecture that the energy cost of deformation of angles between filaments crosslinked with FLNa is larger than the bending energy of filaments. The qualitative redundancy becomes quantitative, for example, near the isostatic point where we obtain the same scaling exponents for G as a function of $p - p_{rp,I}$ and κ (or κ_{nc}) for the free-rotating crosslinked semiflexible network and the compositely crosslinked flexible network. Preliminary data suggests the same scaling extends to compositely crosslinked semiflexible networks. This result is an indication of the robustness of these networks and should not be considered as a weakness. Whether or not this robustness extends to systems experiencing higher strains such that nonlinearities emerge is not yet known.

4.3.3 Lamellipodia mechanics

The interplay between cooperative and redundant mechanical properties may be particularly important for the mechanics of branched F-actin networks in lamellipodia. Within lamellipodia, there exist some filament branches occurring at an angle of around 70° with respect to the plus end of the mother filament (referred to as Y -junctions). These branches are due to the ABP Arp2/3 [20]. During lamellipodia formation, these branches are presumed to be the dominant channel for filament nucleation. The mechanics of Arp2/3 can be modeled as an angular spring between the mother and daughter filament with an angular spring constant of approximately $10^{-19} J rad^{-2}$ [20]. In other words, Arp2/3 is an angle-constraining crosslinker for Y -junctions (as opposed to X -junctions), and thereby plays an important role in lamellipodia mechanics as demonstrated in this work. The mechanical role of Arp2/3 in lamellipodia has not been investigated previously and may help to discriminate between the dendritic nucleation model [101, 15] and a new model [35] by predicting the force transmitted in lamellipodia as a function of the Arp2/3 concentration.

In addition to Arp2/3, FLNa localizes at X -junctions in the lamellipodia and is thought to stabilize the dendritic network [112]. Both angle-constraining crosslinkers lower the filament concentration threshold required for mechanical rigidity in the system. Depending on the energy scale of FLNa as compared to the energy scale of Arp2/3, addition of the FLNa may or may not modulate, for example, the bend-stretch coupling regime at intermediate filament concentrations. Again, at times mechanical redundancy is needed and at times not. With three crosslinkers, the system can maximize the redundancy and the cooperativity. Of course, lamellipodia are dynamic in nature and are anisotropic since the Arp2/3 is activated from the leading edge of a cell. Both attributes will modulate the mechanical response.

Final remarks

We have demonstrated both cooperativity and redundancy in the mechanics of compositely crosslinked filamentous networks. We have done so while maintaining the structure of an isotropic, unbundled filament network. Of course, crosslinkers can alter the morphology of the network via bundling, for example. In other words, different crosslinkers serve specific functions. This specificity results in a change in microstructure. This will presumably affect the mechanics such that the cooperative and redundant interactions between multiple crosslinkers may differ from the above analysis. For example, the crosslinker that dominates in terms of creating the morphology will presumably dominate the mechanics. Schmoller and collaborators [99] suggest that crosslinker with the higher concentration determines the structure and, therefore, the mechanics. Instead of redundancy or cooperativity, the specificity leads to the simple additivity of two types of crosslinkers in that different crosslinkers act independently of one another. In this study, however, we find both cooperativity and redundancy in the network mechanics even in the absence of such structural changes [113], which, is arguably less intuitive and, therefore, more remarkable. Finally, while our focus here has been on the actin cytoskeleton as an example of a filamentous network, our results can be extended to collagen networks as well [114].

Conclusions

Cells crawl, in part, by the extension of their actin cytoskeleton in the direction in which they wish to crawl. This extension is known as the lamellipodium and the mechanisms by which it is initiated can be chemical and/or mechanical sensing at the leading edge membrane of the crawling cell. The extension occurs via the nucleation and polymerization of actin filaments in the direction of preferred motion. The nucleation of new filaments is important so that the cytoskeleton can exert the necessary forces per filament required to continually generate this protrusion at a fixed rate during glide motion. The main activator for filament nucleation is the protein Arp2/3. This protein integrates new filaments into the existing cytoskeletal network by branching new filaments off of preexisting ones near the leading edge. This branching leads to many emergent morphological and mechanical properties of lamellipodia. In this thesis, we investigated the morphology and mechanics of the actin cytoskeleton in the lamellipodium of a crawling cell as well as drew some connections between the two properties.

As for morphology, we explored the connection between the inherent branch angle induced by the Arp2/3 protein between the *mother* and *daughter* filament

and the orientation of filaments with respect to the leading membrane edge. Modeling the nucleation and capping of filaments in the network as birth and death processes respectively, we studied the maximum likelihood of the current filaments in the network to pass on their orientation with respect to the membrane edge to future generations and found an optimal orientation that agrees with experimental observation. Moreover, a new sub-dominant orientation emerged from our analysis, which could in principle allow for a more rigid network as well as allowing the cell to more easily change its crawling direction. The results from our population model for filament orientation were then encoded into a model for the variation in filament density along the leading edge to arrive at a density profile that is in better agreement with experimental results than previous models. We also studied the effect of branching on the overall spatial properties of the network such as the branching induced overlaps of filaments. This analysis helped us address recent controversy over the role of Arp2/3 and how it promotes filament nucleation. It was recently pointed out by the Small group [35], that Arp2/3 forms isolated, cables of F-actin which extend from the membrane edge, as opposed to branches. Their conjecture was based on the experimental observation that there are many more overlapping, presumably crosslinked filaments than branch points. However, we demonstrated that overlapping filaments are a natural emergent property of branching and that filaments oriented at the optimal angle proliferate these overlaps leading to more rigid, crosslinked network.

As for rheology, whether or not disordered networks of crosslinked F-actin form a rigid biomaterial depends on the number of these crosslinks and the mechanical properties of the crosslinks. There are a number of different crosslinkers present in lamellipodia such as filamin A (an angle-constraining crosslinker) and alpha-actinin (a freely-rotating crosslinker). In addition, Arp2/3 acts as an

angle-constraining crosslinker between mother and daughter filaments, in addition to being a nucleator of new filaments. In order to understand how these different crosslinkers affect lamellipodia mechanics, we reviewed the concept of rigidity by counting the fraction of degrees of freedom that are not yet constrained by some interaction in random networks. This fraction represents the number of *floppy modes* left in the system. When this number vanishes we identify this as the onset of rigidity, meaning that all degrees of freedom have been constrained. Filamentous networks of F-actin containing both bending and stretching energies should also display this transition between floppiness and rigidity when we tune the concentration of F-actin and/or the properties and concentration of the crosslinks in the network. We studied this transition and the effect that different cross-links have on a network of filaments in a bond-diluted triangular lattice.

In these compositely crosslinked filament networks, we found that the location of the onset of rigidity depends on the intrinsic properties of the crosslinks that are used to fasten neighboring filaments together. When crosslinks allow for free rotations of neighboring filaments with respect to one another, the average length of filaments at the onset of rigidity is larger than compared to a network containing both types of crosslinkers—freely-rotating and angle-constraining. This is because angle-constraining crosslinks remove a rotational degree of freedom. Here, the two crosslinkers act cooperatively to lower the rigidity threshold. We also studied a second transition in these networks which comes about when the relative strength of bending to stretching elastic response is $\ll 1$. When this criterion is met, the system undergoes a mechanical transition from a purely non-affine deformation dominated regime to a purely affine regime at the isostatic point. Moreover, we found that introducing angle-constraining crosslinkers can completely remove this transition when the energetic penalty for deforming angle-constraining crosslink is comparable to the penalty for stretching. On the other hand, both purely freely-

rotating crosslinked networks and compositely crosslinked networks demonstrate non-affine behavior near the onset of rigidity and eventually crossover to an affine deformation regime at larger concentrations of F-actin. In this way, both types of crosslinkers act redundantly. Compositely crosslinked filamentous networks provides the system with both redundant and cooperative interplay that can, for example, allow systems to become rigid even when the fraction of bonds on the lattice is right near the connectivity percolation transition.

In summary, the connection between the architecture or morphology of lamellipodia to its mechanical properties can be observed via one important visible feature, namely branching. Branching gives rise to specific morphological motifs which ensures that filaments remain oriented toward the protruding leading edge to sustain motion. Not only do filaments exhibit an optimal orientation because of branching, this optimum also provides the cytoskeleton with the appropriate density of filaments to push against the membrane and other external forces. Branching also provides for a maximally overlapped network of filaments. These overlaps provide the cell with a more rigid structure. The interplay of angle-constraining and freely-rotating crosslinks provide the cytoskeleton with a multitude of differing mechanical regimes that can be accessed by changing the relative concentrations of these cross-links. Finally, the ability to manipulate the actin cytoskeleton by actively changing its architecture as well as its mechanical response seems to be the main advantage behind the incorporation of the branching design principle into the lamellipodia of crawling cells.

Appendix A

Leading Edge Filament Density Profile

A.1 Lateral flow velocity

To begin, the full derivative of the function, $f(x, t)$ (see Fig. A.1), is

$$\frac{df}{dx} = \frac{\partial f}{\partial x} + \frac{\partial f}{\partial t}v(x, t)^{-1}, \quad (\text{A.1})$$

where $v(x, t) = dx/dt$. Rearranging this equation and noting that $v(x, t)$ changes direction for either \pm (left, right) populations, I arrive at

$$v(x, t) = \frac{\pm \partial f / \partial t}{\partial f / \partial x - df / dx}. \quad (\text{A.2})$$

The full derivative of f with respect to x is given by considering the tangent to the curve $f(x, t)$ as seen in Fig. A.1. One can see that the *tangent* of the angle θ

is

$$\tan(\theta) = \frac{\Delta x}{\Delta f} \rightarrow \frac{df}{dx} = \cot(\theta). \quad (\text{A.3})$$

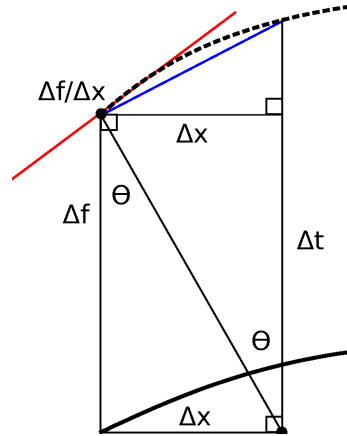


Figure A.1: Schematic of filament lateral flow due to expansion of the leading edge. Note that Δf is the full derivative of $f(x, t)$. The dashed curve is the leading edge at a time of $t + \Delta t$ and the position of the filament between the two solid dots has moved from x to $x + \Delta x$.

The lateral velocity can now be expressed as

$$v(x, t) = \frac{\mp \partial f / \partial t}{\cot(\theta) - \partial f / \partial x}. \quad (\text{A.4})$$

The angle θ is the optimal orientation angle which was found to be half of the branch angle as discussed in Sec. 1.2 and given by Eq. 1.2 [22].

Appendix B

Rigidity and Effective Medium Theory (EMT)

B.1 Linearized Energy: Stretching and bending interactions

B.1.1 Stretching

In Chapter 3, Eq. 3.5 gives the linearized energy of a central-force spring network. To arrive at that result, I first write the energy in terms of the displacement vectors of the bonds between sites i and j on the effective lattice,

$$E_s = \frac{\alpha_m}{2} \sum_{\langle ij \rangle} (|\mathbf{R}'_{ij}|^2 - |\mathbf{R}_{ij}|^2). \quad (\text{B.1})$$

Here the prime denotes the displaced bond by the strain \mathbf{u}_{ij} and $\hat{\mathbf{r}}_{ij} \equiv \frac{\mathbf{R}_{ij}}{|\mathbf{R}_{ij}|}$. Using the definition,

$$\mathbf{R}'_{ij} = \mathbf{R}_{ij} + \mathbf{u}_{ij}, \quad (\text{B.2})$$

to first order in the strain,

$$|\mathbf{R}'_{ij}| \approx |\mathbf{R}_{ij}| \left(1 + \frac{\mathbf{u}_{ij} \cdot \mathbf{R}_{ij}}{|\mathbf{R}_{ij}|} \right). \quad (\text{B.3})$$

Inserting this result into Eq. [refeq:fullCF-Ener](#), for small strain,

$$E_s = \frac{\alpha_m}{2} \sum_{\langle ij \rangle} (\mathbf{u}_{ij} \cdot \hat{\mathbf{r}}_{ij})^2. \quad (\text{B.4})$$

B.1.2 Bending

To calculate the bending energy in Eq. [3.23](#), I, again, write the full expression for the bending energy on the perfect lattice as

$$E_b = \frac{\kappa_m}{2} \sum_{\langle i\hat{j}k=\pi \rangle} (\theta_{ijk})^2. \quad (\text{B.5})$$

Here, angle θ_{ijk} is the angle between the two bond vectors \mathbf{R}_{ij} and \mathbf{R}_{ik} defined by

$$\sin(\theta_{ijk}) = \frac{|\mathbf{R}'_{ij} \times \mathbf{R}'_{ik}|}{|\mathbf{R}'_{ij}| |\mathbf{R}'_{ik}|} \quad (\text{B.6})$$

For small θ_{ijk} (strain), $\sin(\theta_{ijk}) \approx \theta_{ijk}$. Furthermore, using the definition for $\mathbf{R}'_{ij} = \mathbf{R}_{ij} + \mathbf{u}_{ij}$ from the previous section, the numerator in the expression for the energy becomes ($\mathbf{u}_{ij} \cdot \mathbf{u}_{ik} \rightarrow \mathcal{O}(\delta u^2) \ll 1$)

$$|\mathbf{u}_{ij} \times \mathbf{R}_{ik} - \mathbf{u}_{ik} \times \mathbf{R}_{ij}|. \quad (\text{B.7})$$

In addition, the denominator can be approximated as

$$|\mathbf{R}'_{ij}| \approx |\mathbf{R}_{ij}| \left(1 + \frac{\mathbf{u}_{ij} \cdot \mathbf{R}_{ij}}{|\mathbf{R}_{ij}|} \right) \quad (\text{B.8})$$

$$|\mathbf{R}'_{ik}| \approx |\mathbf{R}_{ik}| \left(1 + \frac{\mathbf{u}_{ik} \cdot \mathbf{R}_{ik}}{|\mathbf{R}_{ik}|} \right).$$

The combination of these two terms in the denominator will lead to a multiplicative factor proportional to $(1 - (\mathbf{u}_{ij} + \mathbf{u}_{ik}) \cdot \mathbf{r}_{ij})$. Neglecting all terms proportional to δu^2 and higher, I obtain

$$E_b = \frac{\kappa_m}{2} \sum_{\langle ij\hat{k}=\pi \rangle} ((\mathbf{u}_{ij} + \mathbf{u}_{ik}) \times \mathbf{r}_{ij})^2, \quad (\text{B.9})$$

where I have used the fact that all bonds are at rest length unity and are only considering collinear pairs of bonds by replacing all unit vectors with \mathbf{r}_{ij} .

B.2 Dynamical matrix calculation of a^*

The potential energy for a fully occupied lattice of central-force springs is given by

$$E_s = \frac{\alpha_m}{2} \sum_{\langle ij \rangle} (\mathbf{u}_{ij} \cdot \hat{\mathbf{r}}_{ij})^2. \quad (\text{B.10})$$

I can compute a^* by considering the fully occupied lattice and the force on site i , which is given by

$$\mathbf{F}_i = -\frac{\partial E}{\partial \mathbf{u}_i} = -\sum_j \mathbf{D}_{ij} \mathbf{u}_j. \quad (\text{B.11})$$

By Fourier analysis, I find a^* by considering the force f exerted on the bond ij as before (Chapter 3, page 63) and force balance gives

$$\mathbf{F}_j = f \hat{\mathbf{r}}_{12} (\delta_{1j} - \delta_{2j}). \quad (\text{B.12})$$

Here, $\delta_{ij=1,2}$ is the Kronecker delta. The Fourier transform of the dynamical equation (eq. B.11) for site i yields

$$\mathbf{u}_k = \mathbf{D}^{-1}(\mathbf{k}) \cdot \mathbf{F}_k. \quad (\text{B.13})$$

****Note:**

$$\mathbf{F}_k = \sum_i \mathbf{F}_i e^{i\mathbf{k} \cdot \hat{\mathbf{r}}_i}$$

$$\mathbf{D}(\mathbf{k}) = \sum_{i,j} \mathbf{D}_{ij} e^{i\mathbf{k} \cdot \hat{\mathbf{r}}_{ij}}$$

Where $\hat{\mathbf{r}}_{ij}$ is the lattice unit vector between sites i and j .

****End Note:**

I then use equation B.11 to find the response of the system when a force f is applied to the sites i and j , recalling that in the perfect case the effective spring constant between the sites i and j is $\alpha'_m = \alpha_m/a^*$. In other words,

$$\delta u = (u_i - u_j) = \frac{f}{\alpha_m/a^*}.$$

The inverse FT of Eq. B.13 is

$$\begin{aligned}\mathbf{u}_i &= \sum_{\mathbf{k}} \mathbf{u}_{\mathbf{k}} e^{-i\mathbf{k}\cdot\mathbf{r}_i} \\ &= - \sum_{\mathbf{k}} \mathbf{D}^{-1}(\mathbf{k}) \cdot \mathbf{F}_{\mathbf{k}} e^{-i\mathbf{k}\cdot\mathbf{r}_i}\end{aligned}\quad (\text{B.14})$$

Inserting the definition for $\mathbf{F}_{\mathbf{k}}$,

$$\mathbf{u}_i = - \sum_{\mathbf{k}} \mathbf{D}^{-1}(\mathbf{k}) \cdot \sum_j \mathbf{F}_j e^{i\mathbf{k}\cdot\mathbf{r}_j} e^{-i\mathbf{k}\cdot\mathbf{r}_i}. \quad (\text{B.15})$$

From Newton's third law, one obtains (for sites 1 and 2) from above

$$\mathbf{u}_i = -f \sum_{\mathbf{k}} \mathbf{D}^{-1}(\mathbf{k}) \cdot \hat{\mathbf{r}}_{12} \sum_j (\delta_{j1} - \delta_{j2}) e^{i\mathbf{k}\cdot\mathbf{r}_j} e^{-i\mathbf{k}\cdot\mathbf{r}_i}. \quad (\text{B.16})$$

If, for example, $i = 1$, only two terms survive the Kronecker deltas, i.e.

$$\mathbf{u}_1 = -\frac{f}{N} \sum_{\mathbf{k}} \mathbf{D}^{-1}(\mathbf{k}) \cdot \hat{\mathbf{r}}_{12} (1 - e^{-i\mathbf{k}\cdot\hat{\mathbf{r}}_{12}}), \quad (\text{B.17})$$

where N arises from the sum over j and is the number of sites in the lattice,

Now, δu is obtained from

$$\mathbf{u}_2 - \mathbf{u}_1 = \frac{f}{N} \sum_{\mathbf{k}} (2 - e^{-i\mathbf{k}\cdot\hat{\mathbf{r}}_{12}} - e^{i\mathbf{k}\cdot\hat{\mathbf{r}}_{12}}) \mathbf{D}^{-1}(\mathbf{k}) \cdot \hat{\mathbf{r}}_{12} \quad (\text{B.18})$$

such that a^* , which is deformation along $\hat{\mathbf{r}}_{12} \cdot (\mathbf{u}_2 - \mathbf{u}_1)$, is given by

$$a^* = \frac{1}{N} \sum_{\mathbf{k}} (2 - e^{-i\mathbf{k}\cdot\hat{\mathbf{r}}_{12}} - e^{i\mathbf{k}\cdot\hat{\mathbf{r}}_{12}}) \hat{\mathbf{r}}_{12} \cdot \mathbf{D}^{-1}(\mathbf{k}) \cdot \hat{\mathbf{r}}_{12}. \quad (\text{B.19})$$

Also, $\mathbf{D}^{-1}(\mathbf{k})$ is diagonal in this basis, $\hat{\mathbf{r}}_{ij} = \hat{\delta}$, and all lattice vectors are equivalent so that

$$a^* = \frac{2}{Nz} \sum_{\mathbf{k}, \hat{\delta}} \text{Tr} \{ [1 - e^{i\mathbf{k} \cdot \hat{\delta}}] (\hat{\delta} \hat{\delta} \cdot \mathbf{D}^{-1}(\mathbf{k})) \} = \frac{2}{Nz} \sum_{\mathbf{k}} \text{Tr} [\mathbf{D}(\mathbf{k}) \mathbf{D}^{-1}(\mathbf{k})]. \quad (\text{B.20})$$

The trace in d dimensions is $d * N$ which is just the number of degrees of freedom for system of N sites. Thus, a^* is related to the isostatic point for this system, or

$$a^* = \frac{2d}{z} = p_{iso}. \quad (\text{B.21})$$

For $d = 2$ and $z = 6$ (triangular lattice), $a^* = 2/3$. Therefore, from the constitutive equations, $p = p_{iso} = 2/3$ since α_m must vanish below and at the rigidity percolation threshold. The factor of a^* is really a geometric parameter that tells us how forces with propagate due to the topology and dimension of the system, hence z and d in the expression for a^* . Finally, when bending interactions between collinear bonds are added, one expect forces on the site j which joins adjacent bonds to have the form

$$\mathbf{F}_s^j = \alpha_m \sum (\mathbf{u}_{ij} + \mathbf{u}_{jk}) \cdot \hat{\mathbf{r}}_{jk} \hat{\mathbf{r}}_{jk} \quad (\text{B.22})$$

B.3 Dynamical matrix calculation for b^*

When a bending interaction is included on the lattice between adjacent collinear bonds there is a contribution to the effective lattice elastic constants. Of course, one assumes that deformations are small enough that the transverse and longitudinal motions of the lattice sites are decoupled. So, to begin I find the force on site j due to bending alone starting with Eq. B.9

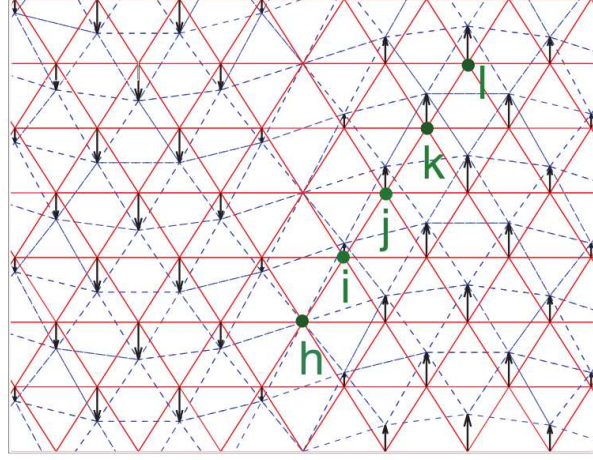


Figure B.1: Schematic figure of the filament network. The solid red lines represent the undeformed filament network, while the dashed blue lines show the deformation field having wavevector \mathbf{q} and displacement amplitude \mathbf{u} (shown in the upper left corner of the figure). The black arrows show the displacement field at each lattice point. This perfect lattice is disordered by making randomly placed cuts in the infinitely long filaments. These are not shown. [Courtesy of M. Das, unpublished]

$$\mathbf{F}_b^j = \kappa_m \sum_{\langle h i k l \rangle} \left[\begin{aligned} & [(\mathbf{u}_{ji} + \mathbf{u}_{jk}) - (\mathbf{u}_{ji} + \mathbf{u}_{jk}) \cdot \hat{\mathbf{r}}_{ji} \hat{\mathbf{r}}_{ji}] \\ & + \frac{1}{2} [(\mathbf{u}_{ih} + \mathbf{u}_{ij}) - (\mathbf{u}_{ih} + \mathbf{u}_{ij}) \cdot \hat{\mathbf{r}}_{ih} \hat{\mathbf{r}}_{ih}] \\ & + \frac{1}{2} [(\mathbf{u}_{kj} + \mathbf{u}_{kl}) - (\mathbf{u}_{kj} + \mathbf{u}_{kl}) \cdot \mathbf{r}_{kl} \mathbf{r}_{kl}] \end{aligned} \right], \quad (\text{B.23})$$

where I have used the vector identity $\vec{A} \times (\vec{B} \times \vec{C}) = (\vec{A} \cdot \vec{C})\vec{B} - (\vec{A} \cdot \vec{B})\vec{C}$. One must include all interactions that the site j participates in such that the triplets hij and jkl which must also be included into the total force on j .

Now, Fourier transforming the above dynamical equation, using

$$\mathbf{F}_\mathbf{k} = \sum_i \mathbf{F}_i e^{i\mathbf{k} \cdot \hat{\mathbf{r}}_i} \quad (\text{B.24})$$

$$\mathbf{u}_j = \sum_{\mathbf{k}} \mathbf{u}_\mathbf{k} e^{-i\mathbf{k} \cdot \hat{\mathbf{r}}_j}, \quad (\text{B.25})$$

and transforming all displacements to Fourier space, Eq. B.23 becomes,

$$\mathbf{u}_{ji}e^{i\mathbf{k}\cdot\hat{\mathbf{r}}_j} = \sum_{\mathbf{k}} \mathbf{u}_{\mathbf{k}}(1 - e^{i\mathbf{k}\cdot\hat{\mathbf{r}}_{ji}}) = -\mathbf{u}_{ij}e^{i\mathbf{k}\cdot\hat{\mathbf{r}}_j} \quad (\text{B.26})$$

$$\mathbf{u}_{jk}e^{i\mathbf{k}\cdot\hat{\mathbf{r}}_j} = \sum_{\mathbf{k}} \mathbf{u}_{\mathbf{k}}(1 - e^{i\mathbf{k}\cdot\hat{\mathbf{r}}_{jk}}) = -\mathbf{u}_{kj}e^{i\mathbf{k}\cdot\hat{\mathbf{r}}_j} \quad (\text{B.27})$$

$$\mathbf{u}_{ih}e^{i\mathbf{k}\cdot\hat{\mathbf{r}}_j} = \sum_{\mathbf{k}} \mathbf{u}_{\mathbf{k}}(e^{i\mathbf{k}\cdot\hat{\mathbf{r}}_{ji}} - e^{i\mathbf{k}\cdot\hat{\mathbf{r}}_{jh}}) \quad (\text{B.28})$$

$$\mathbf{u}_{kl}e^{i\mathbf{k}\cdot\hat{\mathbf{r}}_j} = \sum_{\mathbf{k}} \mathbf{u}_{\mathbf{k}}(e^{i\mathbf{k}\cdot\hat{\mathbf{r}}_{jk}} - e^{i\mathbf{k}\cdot\hat{\mathbf{r}}_{jl}}). \quad (\text{B.29})$$

Adding these terms together, I arrive at

$$\mathbf{F}_{\mathbf{k}} = \kappa_m \sum_{\mathbf{k}} \mathbf{u}_{\mathbf{k}} \sum_{\langle ij \rangle} \left[4(1 - \cos(\mathbf{k} \cdot \hat{\mathbf{r}}_{ji})) - ((1 - \cos(2\mathbf{k} \cdot \hat{\mathbf{r}}_{ji}))) \right] (\mathbf{I} - \hat{\mathbf{r}}_{ji}\hat{\mathbf{r}}_{ji}). \quad (\text{B.30})$$

Also, since all lattice vectors are of unit length, one can interchange the indices keeping track of the directionality of the unit vectors. Summing over all $\langle ji \rangle$ bonds, (see figure B.1).

$$ij = ji \quad (\text{B.31})$$

$$jk = -ji$$

$$jh = 2ji$$

$$jl = -2ji$$

the dynamical matrix for just the bending interaction is

$$\mathbf{D}_b(\mathbf{k}) = \kappa_m \sum_{\langle ij \rangle} \left[4(1 - \cos(\mathbf{k} \cdot \hat{\mathbf{r}}_{ji})) - (1 - \cos(2\mathbf{k} \cdot \hat{\mathbf{r}}_{ji})) \right] (\mathbf{I} - \hat{\mathbf{r}}_{ji}\hat{\mathbf{r}}_{ji}). \quad (\text{B.32})$$

The effective elastic constant κ_m/b^* from the dynamical matrix given above is found by assuming that the bending and stretching deformations are decoupled

and, hence, I write the total force on the site j as (see Eq. B.22)

$$\mathbf{F}^j = \mathbf{F}_s^j + \mathbf{F}_b^j. \quad (\text{B.33})$$

From this equation the displacement of the bond ji is found by inverting the dynamical equation the same way as was done in Sec. B.2, which can be written as

$$\mathbf{u}_{\parallel,\perp}(\mathbf{k}) = -\mathbf{D}^{-1}(\mathbf{k})\mathbf{F}_{s,b}(\mathbf{k}), \quad (\text{B.34})$$

where $\mathbf{D}(\mathbf{k}) = \mathbf{D}_s(\mathbf{k}) + \mathbf{D}_b(\mathbf{k})$ is the full dynamical matrix. To project out the transverse modes and extract κ_m/b^* , I inverse Fourier transform $\mathbf{u}_\perp(\mathbf{k})$ (bearing in mind these are bond modes, not site modes), which is equivalent to

$$\mathbf{u}_{ji} = \sum_{\mathbf{k}} \mathbf{D}_b(\mathbf{k})\mathbf{u}_\perp(\mathbf{k}) = \frac{2}{Nz} \sum_{\mathbf{k}} \text{Tr}[\mathbf{D}_b(\mathbf{k})\mathbf{D}^{-1}(\mathbf{k})]\mathbf{F}_b(\mathbf{k}). \quad (\text{B.35})$$

The sum is over the first Brillouin zone and b^* is

$$b^* = \frac{2}{Nz} \sum_{\mathbf{k}} \text{Tr}[\mathbf{D}_b(\mathbf{k})\mathbf{D}^{-1}(\mathbf{k})]. \quad (\text{B.36})$$

To perform the matrix product, which is implicitly summed over the unit cell, one needs the unit vectors which form the basis that the dynamical matrix is expressed in, or

$$\hat{\mathbf{r}}_{ji} \pm \hat{\mathbf{x}} \quad (\text{B.37})$$

$$\hat{\mathbf{r}}_{ji} \pm \cos\left(\frac{\pi}{3}\right)\hat{\mathbf{x}} \pm \sin\left(\frac{\pi}{3}\right)\hat{\mathbf{y}} \quad (\text{B.38})$$

Inserting these into Eq. B.32 I obtain

$$D_s = \alpha_m \begin{pmatrix} - (2 \cos(q_x) + \cos(\frac{q_x}{2}) \cos(\frac{1}{2}\sqrt{3}q_y) - 3) & \sqrt{3} \sin(\frac{q_x}{2}) \sin(\frac{1}{2}\sqrt{3}q_y) \\ \sqrt{3} \sin(\frac{q_x}{2}) \sin(\frac{1}{2}\sqrt{3}q_y) & -3 (\cos(\frac{q_x}{2}) \cos(\frac{1}{2}\sqrt{3}q_y) - 1) \end{pmatrix} \quad (\text{B.39})$$

$$D_b = \frac{\kappa_m}{4} \begin{pmatrix} 3(-4 \cos(\frac{q_x}{2}) \cos(\frac{1}{2}\sqrt{3}q_y) & \sqrt{3}(\sin(q_x) \sin(\sqrt{3}q_y)) \\ + \cos(q_x L) \cos(\sqrt{3}q_y) + 3 & -4 \sin(\frac{q_x}{2}) \sin(\frac{1}{2}\sqrt{3}q_y) \\ \sqrt{3}(\sin(q_x) \sin(\sqrt{3}q_y) \sin(\frac{1}{2}\sqrt{3}q_y)) & (2 \cos(2q_x) - 4 \cos(\frac{q_x}{2}) \cos(\frac{1}{2}\sqrt{3}q_y)) \\ -4 \sin(\frac{q_x}{2}) & + \cos(q_x) (\cos(\sqrt{3}q_y) - 8) + 9 \end{pmatrix}.$$

Finally, the relation for a^* and b^* is set by

$$a^* + b^* = \frac{2d}{z}. \quad (\text{B.40})$$

Appendix C

Semiflexible Chain

Force-extension

C.1 The weak bending limit

For stiff chains, where fluctuations are derived primarily from bending deformations, one implicitly assumes that the chain has no compliance along its contour. To calculate the contraction of its fully extended contour length due to the presence of thermal fluctuations one can relax this condition.

To begin, the full contour length can be found by integrating the magnitude of tangent vector field over the contour length of the chain, or

$$l = \int ds |\vec{t}(s)|. \tag{C.1}$$

This is the precise definition of inextensibility, which implies that $|\vec{t}(s)|^2 = 1$. One can relax this condition by approximating the magnitude of the tangent vector as

the projected length of the chain along some central axis [11], or

$$\int ds |\vec{t}(s)| \approx \left[\int ds \sqrt{1 + \left| \frac{dr}{ds} \right|^2} \right]. \quad (\text{C.2})$$

Within this approximation, the change in length of the chain is

$$\Delta l = \int dx \left(\sqrt{1 + \left| \frac{dr}{ds} \right|^2} - 1 \right) \simeq \frac{1}{2} \int dx \left| \frac{dr}{ds} \right|^2 = \frac{l}{4} \sum_q q^2 u_q^2. \quad (\text{C.3})$$

This is the term in which the force f from Eq. 3.17 couples to since the work done by a force to change the length of the chain by a distance Δl , is $E \sim f \Delta l$.

To obtain the force-extension relation of the chain, I investigate the response of the chain in the presence of the tension force and in the absence of. In this sense, one is looking at the response of the fluctuations in the chain due to an external force field and, hence, the response of the chain will be governed by the most dominant transverse mode, u_q . This mode in the weak bending limit will be on the order of the contour length of the chain l such that

$$\langle \Delta l \rangle_0 = \frac{l}{4} \sum_q q^2 \langle u_q^2 \rangle = \frac{k_B T l^2}{k \pi^2} \sum_n \frac{1}{n^2} = \frac{l^2}{6l_p}. \quad (\text{C.4})$$

Here, one assumes *pinned* boundary conditions so that the wave number $q = 1/\lambda$ with wavelength $\lambda = l/n\pi$ and the expression for $\langle u_q^2 \rangle$ is given by Eq. 3.19.

The mean value of u_q^2 can be found by the Gaussian integrals,

$$\langle u_q^2 \rangle = \frac{\int \mathcal{D}[u_q] u_q^2 e^{\frac{-l}{4k_B T} \sum_q (kq^4 + fq^2) u_q^2}}{\int \mathcal{D}[u_q] e^{\frac{-l}{4k_B T} \sum_q (kq^4 + fq^2) u_q^2}}. \quad (\text{C.5})$$

This can be expressed as

$$\langle u_q^2 \rangle = -\frac{d}{da(q)} \log \int d(u_q) e^{\frac{-l}{4k_B T} a(q) u_q^2}, \quad (\text{C.6})$$

where $a(q) = (kq^4 + fq^2)$. Finally,

$$\langle u_q^2 \rangle = \frac{4k_B T}{l(kq^4 + fq^2)} \quad (\text{C.7})$$

for a chain in three-dimensions. Therefore,

$$\delta l = \langle \Delta l \rangle_0 - \langle \Delta l \rangle_f = \frac{k_B T l^2}{k\pi^2} \sum_n \left(\frac{1}{n^2} - \frac{1}{n^2 + \phi} \right) = \frac{k_B T l^2}{k\pi^2} \sum_n \frac{\phi}{n^2(n^2 + f)}, \quad (\text{C.8})$$

where $\phi = fl^2/\kappa\pi^2$. It is interesting to note that $\kappa\pi^2/l^2$ is the classical Euler buckling force for an elastic beam [115, 116, 11]. Evaluating this sum in the large wavelength ($\lambda \sim l$) limit, one obtains Eq. 3.21.

Bibliography

- [1] D'Arcy Wentworth Thompson. *On growth and form*. Dover Pub. Inc., New York, 1942.
- [2] E.M. Purcell. Life at low reynolds number. *American Journal of Physics*, **45**:3–11, 1977.
- [3] Berk A Lodish H, Zipursky SL, and et al. *Molecular cell biology. 4th ed.* W. H. Freeman, New York, 2000.
- [4] C. S. Peskin, G. M. Odell, and G. F. Oster. Cellular motions and thermal fluctuations: The brownian ratchet. *Biophys. J.*, **65**:316–324, 1993.
- [5] A. Mogilner and G. Oster. Cell motility driven by actin polymerization. *Biophys. J.*, **71**:3030–3045, 1996.
- [6] R. D. Mullins, J. A. Heuser, and T. D. Pollard. The interaction of arp2/3 complex with actin: nucleation, high affinity pointed end capping, and formation of branching networks of filaments. *Proc. Natl. Acad. Sci. USA*, **95**:6181–6186, 1998.
- [7] Revathi Ananthakrishnan and Allen Ehrlicher. The forces behind cell movement. *Int. J. Biol. Sci.*, **3**:303–317, 2007.
- [8] Julet Lee and *et al.* Principles of locomotion for simple-shaped cells. *Nature*, **362**:167, 1993.

-
- [9] C. I. Lacayo and *et al.* Emergence of large-scale cell morphology and movement from local actin filament growth dynamics. *PLoS Biol.*, **5**:2035–2052, 2007.
- [10] Bruce Alberts, Alexander Johnson, Julian Lewis, Martin Raff, Keith Roberts, and Peter Walter. *Molecular biology of the cell, 4th ed.* Garland Science, New York, 2002.
- [11] Fred C. MacKintosh and *et al.* *Soft condensed matter physics in molecular and cell biology.* CRC Press., Boca Raton FL., 2006.
- [12] Arshad Desai and Timothy J. Mitchison. Microtubule polymerization dynamics. *Annu. Rev. Cell Dev. Biol.*, **13**:83–117, 1997.
- [13] Manuel L. Cano, Douglas A. Lauffenburger, and Sally H. Zigmond. Kinetic analysis of f-actin depolymerization in polymorphonuclear leukocyte lysates indicates that chemoattractant stimulation increases actin filament number without altering filament length distribution. *J. Cell Bio.*, **115**:677–687, 1991.
- [14] N. Mücke, L. Kreplak, R. Kirmse, T Wedig, H. Herrmann, U. Aebi, and J. Langowski. Assessing the flexibility of intermediate filaments by atomic force microscopy. *J. Mol. Bio.*, **335**:1241–1250, 2004.
- [15] T. M. Svitkina and G. G. Borisy. Arp2/3 complex and actin depolymerizing factor/cofilin in dendritic organization and treadmilling of actin filament array in lamellipodia. *J. Cell Biol.*, **145**:1009–1026, 1999.
- [16] Thomas E. Schaus *et al.* Self-organization of actin filament orientations in the dendritic-nucleation/array-treadmilling model. *PNAS*, **17**:7086, 2006.

-
- [17] E.H. Egelman, N. Francis, and D.J. DeRosier. F-actin is a helix with a random variable twist. *Nature*, **298**:131–135, 1982.
- [18] P. M. Chaikin and T. C. Lubensky. *Principles of condensed matter physics*. Cambridge Uni. Press, Cambridge, UK, 2007.
- [19] R. C. May and *et al.* The arp2/3 complex is essential for the actin-based motility of *listeria monocytogenes*. *Curr. Biol.*, **9**:759–762, 1999.
- [20] Blanchoin L, Amann KJ, Higgs HN, Marchand J-B, Kaiser DA, and Pollard TD. Direct observation of dendritic actin filament networks nucleated by arp2/3 complex and wasp/scar proteins. *Nature*, **404**:1007–1011, 2000.
- [21] Coumanran Egile, Isabelle Rouiller, Xiao-Ping XU, Niels Volkman, Rong Li, and Dorit Hanein. Mechanism of filament nucleation and branch stability revealed by the structure of the arp2/3 complex at actin branch junctions. *PloS*, **3**:1902–1909, 2005.
- [22] I. V. Maly and G. G. Borisy. Self-organization of a propulsive actin network as an evolutionary process. *Proc. Natl. Acad. Sci. USA*, **98**:483–518, 2001.
- [23] John A. Cooper and David Sept. New insights into mechanism and regulation of actin capping protein. *Int. Rev. of Cell and Mol. Bio.*, **267**:183–206, 2008.
- [24] Hine Robert. *Membrane. The facts on file dictionary of biology 3rd ed.* Checkmark, New York, New York, 1999.
- [25] Shao JY and Hochmuth RM. Micropipette suction for measuring piconewton forces of adhesion and tether formation from neutrophil membranes. *Biophys. J.*, **71**:2892, 1996.

-
- [26] H. P. Grimm, A. B. Verkhovskiy, A. Mogilner, and J.-J. Meister. Analysis of actin dynamics at the leading edge of crawling cells: implications for the shape of keratocyte lamellipodia. *Eur. Biophys. J.*, **32**:563–577, 2003.
- [27] Marko Kaksonen, Christopher P. Toret, and David G. Drubin. Harnessing actin dynamics for clathrin-mediated endocytosis. *Nature Rev.: Mol. Cell Biol.*, **7**:404–414, 2006.
- [28] M. Prass, K. Jacobson, A. Mogilner, and M. Radmacher. Direct measurement of the lamellipodial protrusive force in a migrating cell. *J. Cell Biol.*, **174**:767–772, 2006.
- [29] A.E. Carlsson, M.A. Wear, and J.A. Cooper. End versus side branching by arp2/3 complex. *Biophysical Journal*, **86**:1074–1081, 2004.
- [30] Richard E. Michod. On fitness and adaptedness and their role in evolutionary explanation. *Jour. of the History of Bio.*, **19**:289, 1986.
- [31] J.F. Crow and M. Kimura. *An introduction to population genetics theory*. Harper & Row, New York, New York, 1970.
- [32] R. A. Fisher. *The genetical theory of natural selection*. Oxford Univ. Press, Oxford, U.K., 1999.
- [33] K. Keren and *et al.* Mechanism of shape determination in motile cells. *Nature*, **453**:475–480, 2008.
- [34] Lee J, Ishihara A, and Jacobson K. The fish epidermal keratocyte as a model system for the study of cell locomotion. *Symp Soc Exp Biol*, **47**:73, 1993.
- [35] E. Urban and *et al.* Electron tomography reveals unbranched networks of actin filaments in lamellipodia. *Nat. Cell. Biol.*, **12**:429–435, 2010.

-
- [36] Ovijit Chaudhuri, Sapun H. Parekh, and Daniel A. Fletcher. Reversible stress softening of actin networks. *Nature*, **445**:295–298, 2007.
- [37] D. Bray. *Cell movements: From molecules to motility*. Garland, New York, NY, 2001.
- [38] S. M. Rafelski and J. A. Theriot. Crawling toward a unified model of cell mobility: spatial and temporal regulation of actin dynamics. *Annu. Rev. Biochem.*, **73**:209–239, 2004.
- [39] A. Mogilner. Mathematics of cell motility: have we got its number? *J. Math. Biol.*, **58**:105–134, 2009.
- [40] T. D Pollard, L. Blanchoin, and R. D. Mullins. Molecular mechanisms controlling actin filament dynamics in nonmuscle cells. *Ann. Rev. Biophys. Biomol. Struct.*, **29**:545–576, 2000.
- [41] T. P Loisel and *et al.* Reconstitution of actin-based motility of listeria and shigella using pure proteins. *Nature*, **401**:613–616, 1999.
- [42] M.-F. Carlier and *et al.* Actin-based motility as a self-organized system: mechanism and reconstitution *in vitro*. *C. R. Biologies*, **326**:161–170, 2003.
- [43] A. Gopinathan, K.-C. Lee, J. M. Schwarz, and A. J. Liu. Branching, capping, and severing in dynamic actin structures. *Phys. Rev. Lett.*, **99**:058103–058103–4, 2007.
- [44] J. Weichsel and U. Schwarz. Two competing orientation patterns explain experimentally observed anomalies in growing actin networks. *Proc. Natl. Acad. Sci. USA*, **107**:6304–6309, 2010.

-
- [45] P. B. Moore, H. E. Huxley, and D. J. DeRosier. Three-dimensional reconstruction of f-actin, thin filaments and decorated filaments. *J. of Mol. Biol.*, **50**:279–288, 1969.
- [46] D. T. Woodrum, S. A. Rich, and T. D. Pollard. Evidence for biased bidirectional polymerization of actin filaments using heavy meromyosin prepared by an improved method. *J. Cell. Biol.*, **67**:231–237, 1975.
- [47] K. C. Holmes and *et al.* Atomic model for the actin filament. *Nature*, **347**:44–49, 1990.
- [48] I. Ichetovkin, W. Grant, and J. Condeelis. Cofilin produces newly polymerized actin filaments that are preferred for dendritic nucleation by the arp2/3 complex. *Curr. Biol.*, **12**:79–84, 2002.
- [49] C. Yang, M. Hoelzle, A. Disanza, G. Scita, and T. Svitkina. Coordination of membrane and actin cytoskeleton dynamics during filopodia protrusion. *PLoS ONE*, **4**:e5678, 2009.
- [50] A. E. Carlsson. The effect of branching on the critical concentration and average filament length. *Biophys. J.*, **89**:130–140, 2005.
- [51] T. Odijk. Microfibrillar buckling within fibers under compression. *J. of Chem. Phys.*, **108**:6923–6928, 1998.
- [52] W. J. Bock and G. von Wahlert. Adaptation and the form-function complex. *Evolution: Int. J. of Organic Evol.*, **19**:269–299, 1965.
- [53] B. Rubinstein and A. Mogilner. The physics of filopodia protrusion. *Biophys. J.*, **89**:782–795, 2005.

-
- [54] S. A. Koestler and *et al.* Differentially oriented populations of actin filaments generated in lamellipodia collaborate in pushing and pausing at the cell front. *Nat. Cell Biol.*, **10**:306–313, 2008.
- [55] D. Raucher and M. P. Sheetz. Cell spreading and lamellipodial extension rate is regulated by membrane tension. *J. Cell. Biol.*, **148**:127–136, 2000.
- [56] S. H. Parekh, O. Chaudhuri, J. A. Theriot, and D. A. Fletcher. Loading history determines the velocity of actin-network growth. *Nat. Cell Biol.*, **7**:1219–1223, 2005.
- [57] A. E. Carlsson. Structure of autocatalytically branched actin solutions. *Phys. Rev. Lett.*, **92**:238102–1–238102–4, 2004.
- [58] H. Kang, A. E. Carlsson, and J. X. Tang. Kinetic overshoot in actin network assembly induced jointly by branching and capping proteins. *Phys. Rev. E*, **80**:041913–1–041913–6, 2009.
- [59] I. E. Hardik, X. Liu, and R. Ekambaram. Elastic stability of plates with varying rigidities. *Computers and Structures*, **38**:161–168, 1991.
- [60] W. M. Briehner, M. Coughlin, and T. J. Mitchinson. Fascin-mediated propulsion of *listeria monocytogenes* independent of frequent nucleation by the arp2/3 complex. *J. Cell Biol.*, **165**:233–242, 2004.
- [61] D. Vignjevic *et al.* Formation of filapodia-like bundles in vitro from a dendritic network. *J. Cell Biol.*, **160**:951–962, 2003.
- [62] K.-C. Lee, A. Gopinathan, and J. M. Schwarz. Modeling for formation of *in vitro* filopodia. *arXiv:0909.2594*, 2009.
- [63] Kreis T and Vale R. *Guidebook to the cytoskeletal and motor proteins*. Oxford University Press, Oxford, 1999.

-
- [64] Courson DS and Rock RS. Actin cross-link assembly and disassembly mechanics for α -actinin and fascin. *J. Biol. Chem.*, **285**:26350–26357, 2010.
- [65] Nakamura F, Osborn TM, Hartemink CA, Hartwig JH, and Stossel TP. Structural basis of filamin a functions. *J. Cell Biol.*, **179**:1011–1025, 2007.
- [66] Stossel TP, Condeelis J, Cooley L, Hartwig JH, Noegel A, Schleicher M, and Shapiro SS. Filamins as integrators of cell mechanics and signaling. *Nat. Rev. Mol. Cell Biol.*, **2**:138–45, 2001.
- [67] Maxwell J C. On the calculation of the equilibrium and stiffness of frames. *Philos. Mag.*, **27**:294–299, 1864.
- [68] C. Moukarzel. Comparison of rigidity and connectivity percolation in two dimensions. *Phys. Rev. E*, **59**:26142622, 1999.
- [69] M. Sahimi. *Progress in percolation theory and its applications, in: Annual Reviews of Computational Physics II.* World Scientific., 1995.
- [70] P.G. De Gennes. On the relation between percolation theory and the elasticity of gels. *Jour. de phys lett.*, **34**:1976, L-1.
- [71] M. Born and K. Huang. *Dynamical theory of crystal lattices.* Oxford Univ. Press, New York, New York, 1954.
- [72] M.F. Thorpe and P.M Duxbury. *Rigidity theory and applications.* Kluwer Academic/Plenum Pub., New York, New York, 1999.
- [73] M. F. Thorpe M. V. Chubynsky. Self-organization and rigidity in network glasses. *Curr. Opin. Sol. St. Mat. Sci.*, **5**:525–532, 2001.
- [74] P. M. Duxbury et al. Floppy modes and the free energy: Rigidity and connectivity percolation on bethe lattices. *Phys. Rev. E*, **59**:2084–2092, 1999.

-
- [75] Martin Ostoja-Starzewski. Lattice models in micromechanics. *Appl. Mech. Rev.*, **55**:35–60, 2002.
- [76] R. K. Pathria. *Statistical mechanics 2nd ed.* Elsevier Butterworth-Heinemann, Burlington, MA, 2004.
- [77] Feng S, Thorpe MF, and Garboczi E. Effective-medium theory of percolation on central-force elastic networks. *Phys. Rev. B*, **31**:276–280, 1985.
- [78] Schwartz LM, Feng S, Thorpe MF, and Sen PN. Behavior of depleted elastic networks-comparison of effective-medium and numerical calculations. *Phys. Rev. B*, **32**:4607–4617, 1985.
- [79] Feng S and Sen PN. Percolation on elastic networks- new exponent and threshold. *Phys. Rev. Lett.*, **52**:216–219, 1984.
- [80] Arbabi S Sahimi M. Mechanics of disordered solids. ii. percolation on elastic networks with bond-bending forces. *Phys. Rev. B*, **47**:703–712, 1993.
- [81] Das M, MacKintosh FC, and Levine AJ. Effective medium theory of semiflexible filamentous networks. *Phys. Rev. Lett.*, **99**:038101, 2007.
- [82] C. Broedersz, X. Mao, F.C. MacKintosh, and T.C. Lubensky. Critical and isostaticity in fiber networks. *arXiv*, **1011.6535**:6 pages, 2010.
- [83] F.C. Mackintosh, J. Käs, and P.A. Janmey. Elasticity of semiflexible polymers. *Phys. Rev. Lett.*, **75**:4425–4428, 1995.
- [84] Gardel ML, Nakamura F, Hartwig JH, Stossel TP, and Weitz DA. Prestressed f-actin networks cross-linked by hinged filamins replicate mechanical properties of cells. *Proc. Natl. Acad. Sci.*, **103**:1762–1767, 2006.
- [85] MacKintosh FC Head DA, Levine AJ. Deformation of cross-linked semiflexible polymer networks. *Phys. Rev. Lett.*, **91**:108102, 2003.

-
- [86] Levine AJ Head DA, MacKintosh FC. Distinct regimes of elastic response and deformation modes of cross-linked cytoskeletal and semiflexible polymer networks. *Phys. Rev. E*, **68**:061907, 2003.
- [87] F.C. MacKintosh D.A. Head and A.J. Levine. Nonuniversality of elastic exponents in random bond-bending networks. *Phys. Rev. E*, **68**:025101(R), 2003.
- [88] Timonen J Latva-Kokko M. Rigidity of random networks of stiff fibers in the low-density limit. *Phys. Rev. E*, **64**:066117, 2001.
- [89] Latva-Kokko M, Mäkinen J, and Timonen J. Rigidity transition in two-dimensional random fiber networks. *Phys. Rev. E*, **63**:046113, 2001.
- [90] Shin JH Gardel ML, MacKintosh FC, Mahadevan L, Matsudaira PA, and Weitz DA. Scaling of f-actin network rheology to probe single filament elasticity and dynamics. *Phys. Rev. Lett.*, **93**:188102, 2004.
- [91] Gardel ML, Shin JH, MacKintosh FC, Mahadevan L, Matsudaira PA, and Weitz DA. Elastic behavior of cross-linked and bundled actin networks. *Science*, **304**:1301–1305, 2004.
- [92] et al Cornelis Storm. Nonlinear elasticity in biological gels. *Nature*, **435**:191–194, 2005.
- [93] Nobuhiko Saito et al. The statistical mechanics of stiff chains. *J. Phys. Soc. Japan*, **22**:1966, 219–226.
- [94] M.L. Gradel, M.T. Valentine, J.C. Crocker, A.R. Bausch, and D.A. Weitz. Microrheology of entangled f-actin solutions. *Phys. Rev. Lett.*, **91**:158302, 2003.

-
- [95] Frey E Wilhelm J. Elasticity of stiff polymer networks. *Phys. Rev. Lett.*, **91**:108103, 2003.
- [96] Rivero F, Furukawa R, Fechheimer M, and Noegel AA. Three actin cross-linking proteins, the 34 kda actin-bundling protein, alpha-actinin and gelation factor (abp-120) have both unique and redundant roles in the growth and development of *dictyostelium*. *J. Cell Sci.*, **112**:2737–2751, 1999.
- [97] Tseng Y, Kole TP, Lee JSH, Fedorov E, Almo SC, Schafer BW, and Wirtz D. How actin cross-linking and bundling proteins cooperate to generate an enhanced mechanical response. *Biochem. Biophys. Res. Comm.*, **334**:183–192, 2005.
- [98] Tilney LG, Connelly KA, Vranich MK, Shaw MK, and Guild GM. Why are two different cross-linkers necessary for actin bundle formation in vivo and what does each cross-link contribute. *J. Cell Biol.*, **143**:121–133, 1998.
- [99] Schmoller KM, Lieleg O, and Bausch AR. Cross-linking molecules modify composite actin networks independently. *Phys. Rev. Lett.*, **101**:118102–1–118102–4, 2008.
- [100] DiDonna B A and Levine A J. Filamin cross-linked semiflexible networks: Fragility under strain. *Phys. Rev. Lett.*, **97**:068104, 2006.
- [101] Pollard TD, Blanchoin L, and Mullins RD. Molecular mechanisms of controlling actin filament dynamics in nonmuscle cells. *Ann. Rev. Biophys. Biomol. Str.*, **29**:545–576, 2000.
- [102] Cai Y Thorpe M F. Mechanical and vibrational properties of network structures. *J. Non. Cryst. Solids*, **114**:19–24, 1989.

-
- [103] Frey E Heussinger C. Floppy modes and nonaffine deformations in random fiber networks. *Phys. Rev. Lett.*, **97**:105501, 2006.
- [104] Esue O and Tseng Yand Wirtz D. α -actinin and filamin cooperatively enhance the stiffness of actin filament networks. *PLOS One*, **4**:e4411, 2009.
- [105] Huisman EM, Heussinger C, Storm C, and Barkema GT. Semiflexible filamentous composites. *Phys. Rev. Lett.*, **105**:118101, 2010.
- [106] Das M and MacKintosh FC. Poisson's ratio and microrheology of composite elastic materials with rigid rods. *Phys. Rev. Lett.*, **105**:138102, 2010.
- [107] Press WH, Teukolsky SA, Vetterling WT, and Flannery BP. *Numerical recipes in C: The art of scientific computing*. Cambridge University Press, New York, 1992.
- [108] Alexander S. Amorphous solids: Their structure, lattice dynamics and elasticity. *Phys. Rep.- Rev. Sec. Phys. Lett.*, **296**:65–236, 1998.
- [109] Kantor Y and Webman I. Elastic properties of random percolating systems. *Phys. Rev. Lett.*, **52**:1891–1894, 1984.
- [110] Hughes G D, Lambert C J, and Burton D. Critical dynamics of a dilute central force network with partial bond bending forces. *J. Phys: Condens. Matter*, **2**:3399–3403, 1990.
- [111] Wyart M, Liang H, Kabla A, and Mahadevan L. Elasticity of floppy and stiff random networks. *Phys. Rev. Lett.*, **101**:215501, 2008.
- [112] Revenu C, Athman R, Robine S, and Louvard D. The co-workers of actin filaments: From cell structures to signals. *Nat. Rev. Cell Biol.*, **5**:1–12, 2004.

-
- [113] Wagner B, Tharmann R, Haase I, Fischer M, and Bausch A R. Cytoskeletal polymer networks: The molecular structure of cross-linkers determines macroscopic properties. *Proc. Natl. Acad. Sci.*, **103**:13974–13978, 2006.
- [114] Stein AM, Vader DA, Weitz DA, and Sander LM. The micromechanics of three-dimensional collagen-i gels. *Complexity*, **16**:22–28, 2010.
- [115] S. Timoshenko. *Theory of elastic stability*. McGraw Hill Book Company, New York, 1936.
- [116] L.D. Landau and E.M. Lifshitz. *Theory of elasticity 3rd ed.* Elsevier, Oxford, UK., 2007.

VITA

NAME OF AUTHOR: David Aaron Quint

PLACE OF BIRTH: Whittier, California

DATE OF BIRTH: August 17, 1978

DEGREES AWARDED:

B.Sc., Physics, UC Santa Cruz, California (2004)

PROFESSIONAL EXPERIENCE:

Syracuse University, Department of Physics, Graduate Student Instructor/Assistant & Graduate Student Researcher (2005-2011)

HONORS AND AWARDS:

STEM Fellow - Awarded DOE National STEM fellowship full graduate stipend (2006-2007)